AD-A278 281

JMENTATION PAGE

Form Approved
OMB No. 0704-0188

2. REPORT DATE

3. REPORT TYPE AND DATES COVERED
FINAL 01 Feb 92 TO 31 Jan 94

4. TITLE AND SUBTITLE
Repetitively Pulsed Backward-Wave Oscillator Investigations

5. FUNDING NUMBERS
2301 ES

(2)

6. AUTHOR(S)
Dr Schamiloglu

7. PERFORMING ORGANIZATION NAME(S) AND ADDRESS(ES)
Department of Electrical & Computer Engineering
Univ of New Mexico
Albuquerque, NM 87131

8. PERFORMING ORGANIZATION REPORT NUMBER
AEOSR-TR- 94 0232

9. SPONSORING/MONITORING AGENCY NAME(S) AND ADDRESS(ES)
AFOSR/NE
110 Duncan Avenue Suite B115
Bolling AFB Washington DC 20332-0001
Dr. Robert Barker

10. SPONSORING/MONITORING AGENCY REPORT NUMBER
F49620-92-J-0157

11. SUPPLEMENTARY NOTES

12a. DISTRIBUTION/AVAILABILITY STATEMENT
APPROVED FOR PUBLIC RELEASE: DISTRIBUTION IS UNLIMITED

12b. DISTRIBUTION CODE

DTIC
ELECTE
APR 2 0 1994
S F D

13. ABSTRACT *(Maximum 200 words)*

SEE EXECUTIVES SUMMARY FOR ABSTRACT

"Original contains color plates: All DTIC reproductions will be in black and white"

DTIC QUA[illegible] 3

14. SUBJECT TERMS

15. NUMBER OF PAGES

16. PRICE CODE

17. SECURITY CLASSIFICATION OF REPORT	**18. SECURITY CLASSIFICATION OF THIS PAGE**	**19. SECURITY CLASSIFICATION OF ABSTRACT**	**20. LIMITATION OF ABSTRACT**
UNCLASSIFIED	UNCLASSIFIED	UNCLASSIFIED	UNLIMITED

AFOSR-TR- 94 0232

Final Technical Report Submitted to AFOSR:
Repetitively Pulsed Backward-Wave Oscillator Investigations
(Grant AFOSR #F49620-92-J-0157 Amend P00001)

31 March 1994

Edl Schamiloglu, Assistant Professor, Principal Investigator
John Gahl, & Donald Shiffler, Assistant Professors, CO-PIs
Pulsed Power & Plasma Science Laboratory
and
Charles Fleddermann, Associate Professor, Co-PI
Center for High Technology Materials

Department of Electrical and Computer Engineering
University of New Mexico
Albuquerque, NM 87131

410551 94-1189

94 4 19 01

Table of Contents

I. Executive Summary

The Pulsed Power & Plasma Science Laboratory at the University of New Mexico (UNM) has completed its initial phase of research on repetitively pulsed high power backward-wave oscillators (BWOs). The aggressive program that we had established seeked to address three basic goals:

1. Understand the physics of high efficiency vacuum BWOs using the Sinus-6 repetitively pulsed electron beam accelerator
2. Study vacuum and initiate plasma-filled long pulse BWO operation using the modified PI-110A accelerator
3. Study the prospects of incorporating ferroelectric ceramic cathodes in high power electron beam-driven microwave sources to improve their operation in the long pulse regime.

We believe that we have enjoyed a great deal of success in achieving most of our goals, and this led us to propose the new three-year effort that we are presently being funded under ("High Efficiency Vacuum and Plasma-Filled Backward-Wave Oscillators: a Critical Evaluation").

A hallmark of our program is the continued synergistic relationship between our group and the following groups:

(i) Sandia National Laboratories (Dr. Lemke)
(ii) Air Force Phillips Laboratory (Drs. Hendricks and Spencer)
(iii) High Current Electronics Institute–Tomsk, Russia (Drs. Korovin, Rostov, Polevin, Roitman and Pegel)
(iv) Institute of Electrophysics–Ekaterinburg, Russia (Academician Mesyats)
(v) Institute of Applied Physics–Nizhny Novgorod, Russia (Dr. Denisov)

Dr. Lemke supports our experimental and theoretical work with TWOQUICK particle-in-cell simulations. He also collaborates on the theoretical aspects of vacuum BWOs. Drs. Hendricks and Spencer have assisted with our experimental work, especially in performing frequency measurements using heterodyning techniques. Drs. Korovin, Rostov and Polevin were especially helpful during the initial stages of teaching us about the Sinus-6 and elucidating the design of the two-stage slow wave structure. Drs. Roitman and Pegel have allowed us to reach the "state-of-the-art" in terms of both the experimentally obtained output characteristics, and the theoretical understanding of efficient vacuum BWOs. (Drs. Roitman and Pegel are "visiting scientists" in our laboratory since October 1993, funded through three separate grants, two from the National Research Council and one from the William and Mary Greve Foundation). Academician Mesyats was a distinguished visiting professor in our laboratory during June–July 1993. He was helpful in describing experiments he had performed in the late 1960's on ferroelectric dielectric cathodes. He also delivered a short course entitled "Advances in Pulsed Electron Acceleration and Applications" which was attended by our students, as well as by scientists from the Air Force Phillips Laboratory, Sandia National Laboratories, and Los Alamos National Laboratory. Finally, Dr. Denisov was invaluable in introducing us to serpentine mode convertors.

The milestones achieved under the auspices of this program are:

Milestones Achieved

- Elucidation of the roles of the "volume" and "surface" modes in high power BWO devices—the first such description of this physics in the literature outside of the former Soviet Union.
- Output power levels exceeding 500 MW in 10 ns bursts routinely obtained using the Sinus-6.
- Good understanding of the relationship between experimental results and TWOQUICK simulations, leading to a refinement of coefficients used in TWOQUICK for the damping of high frequency components.
- Long pulse microwaves generated using modified PI-110A accelerator and equivalent Sinus-6 electron gun and tube geometries.
- Ceramic and metallic thin film coatings identified using quasi-DC experiments. These are the candidate coatings to incorporate in high power microwave tube components.
- Electron emission from bulk ferroelectric samples have been observed and characterized. The presence of extremely energetic electrons have been inferred. The importance of "resetting" the ferroelectric has become apparent during the

course of these studies. There appears to be some viability of the ferroelectric emission process.

Plasma-filled BWO experiments have been postponed to the new programmatic period because of modifications that were incorporated in the long pulse experimental hardware. The modifications result in the Sinus-6 and PI-110A accelerates operating using similar beam, magnetic field, and slow wave structure parameters.

Outline of this Final Technical Report

This final report is organized as follow. Section II highlights the Sinus-6 experimental and theoretical results. Progress on the long pulse BWO experiment and related technologies is described in Sec. III. Progress on the ferroelectric cathode development is presented in Sec. IV. Plans for future work are presented in Sec. V. References for this document are contained in Sec VI. Finally, Appendix A contains three papers that are to appear in the *Proceedings of the 9th IEEE International Pulsed Power Conference*, and Appendix B contains two manuscripts that have been submitted for publication. The first manuscript "Suppression of Vacuum Breakdown Using Thin Film Coatings" summarizes the results of the ceramic and metallic coatings research, and the second manuscript "Efficiency Enhancement of High Power Vacuum BWOs using Nonuniform Slow Wave Structures" presents a detailed description of the experimental and theoretical results of the investigations using the Sinus-6 accelerator.

II. Sinus-6 High Power BWO Experiments and Theory

A. BWO physics

The Sinus-6 accelerator has been operational for 18 months. A total of approximately 15,000 shots have been logged on this machine. The ability to acquire this much data allows us to perform careful experiments with good statistics to elucidate the interaction of relativistic beam electrons with electromagnetic modes in these high power devices. Since the parameter space used to describe the operation of BWOs is so broad, it is essential to have good statistics in order to verify the importance of various factors on the observed output of the device. This ability to aquire a large data base also makes feasible comparisons with particle-in-cell simulations.

The overall conclusions derived from the 18 months of research using the Sinus-6 accelerator are summarized in two publications, one provided in Appendix A ("Effects of Using a Nonuniform-Amplitude Slow Wave Structure in a Repetitively-Pulsed, High Power Relativistic Backward-Wave Oscillator" by Moreland *et al.*), and one provided in Appendix B ("Efficiency Enhancement of High Power Vacuum BWOs using Nonuniform Slow Wave Structures" by Moreland *et al.*). I will summarize here the understanding we have gained during the course of our studies.

The most important piece of physics that was elucidated by the experiments and particle-in-cell simulations is the general electric field structure within a BWO. Insight into the field structure is obtained from both a plot of electron particle density, and a contour plot of E_z, both shown in Fig. 1. The charge density bunches portrayed in the top portion of Fig. 1 are formed as a result of the interaction of the slow space charge wave with a backward traveling surface wave. The wave amplitude in this case is largest near the inner surface of the BWO slow wave structure. The separation between the bunches represents the spatial wavelength of the mode, which is approximaely 1.5 ripple periods.

Additional insight into the general field structure is obtained by the bottom plot in Fig. 1. This contour plot reveals that E_z is largest on axis. This implies the existence of a standard TM waveguide mode in addition to the surface wave, whose characteristics are determined entirely by the waveguide radius. We refer to this

FIG. 1. TWOQUICK simulation of a uniform BWO with typical beam parameters used in the experiments. The figure on top presents a plot of electron current density, while the figure on the bottom presents plots of contours of E_z within the same simulation region. (NOTE: Figure appears on the next page.)

[illegible]

[illegible]

mode as a "volume wave." Inspection of the figure indicates that the volume mode has a wavelength of 3.0 ripple periods (consider, for example, the distance between two separate red-colored regions in the figure), or twice the wavelength of the surface mode.

Movies of the contours of E_z (generated as an output from TWOQUICK) reveal that the volume wave has both backward and forward traveling components, which combine to form a standing wave in approximately the first half of the tube. The various ripple sections used at the ends of the BWO are necessary to match the fields of the finite length device. Thus, the backward traveling surface mode, which interacts with the electron beam, must convert part of its energy into a backward traveling volume mode to satisfy boundary conditions at the cutoff neck in the upstream section. It is at this position that the volume mode is reflected toward the outlet, and ultimately radiated. This fact enables these tubes to operate at such high power levels without breakdown problems since the fields are distributed across the entire cross section of the waveguide.

Another important piece of BWO physics that we learned was that the two-stage nonuniform amplitude slow wave structure (described in the two papers referred to earlier) can be considered as being comprised of a non-oscillating prebunching section, followed by an oscillating section. The prebunching of the electron beam which enters the predominantly uniform downstream section results in increased efficiency for our beam, slow wave structure, and magnetic field parameters.

In concluding this section it should be noted that, whereas researchers in the former Soviet Union have described BWOs invoking fundamental and higher harmonics of the electromagnetic modes in a slow wave structure (most notably, consider Refs. 1 and 2), our presentation is the first description of this by researchers in the United States. Our description evolved independently and was a direct result of our interaction with Dr. Lemke of Sandia National Laboratories (funded independently by the Air Force Phillips Laboratory).

B. Experiments with high power output of BWO

Several simple experiments were performed with the output of the Sinus-6 BWO operating at power levels exceeding 500 MW in order to confirm output radiation mode patterns, and to check output radiation frequency. In this section we present four photographs taken using a 35 mm camera with an open shutter and a darkened room. We will discuss these photographs, presented as Fig. 2 and Fig. 3.

Figure 2 presents photographs of the light emission from a 36 × 37 planar array of neon discharge lamps embedded in styrofoam. The inter-bulb spacing is 2.54 cm and the plane is oriented normal to the incident microwaves, at a distance of 1.5 m from the conical horn antenna. (This distance is barely into the far-field of the antenna for 9.6 GHz radiation.) Note the hole in the center of the pattern on top, consistent with TM_{01} radiation. The pattern on the bottom has no hole in the center, and is representative of a Gaussian-like pattern. Note that the intensity is greater in the pattern on the bottom, as can be inferred by the intensity of the color emitted by the discharge bulbs. This is because peak power densities for the TM_{01} radiation pattern are on the order of 80 kW/cm^2 and the peak power densities for the TE_{11} radiation pattern are on the order of 450 kW/cm^2. The TE_{11} pattern was obtained by using our serpertine mode convertor (98% conversion efficiency), designed by the Institute of Applied Physics, Nizhny Novgorod, Russia.[3]

Figure 3 (top) presents an open shutter photograph of TE_{11} radiation exiting the vacuum window at the end of the conical horn antenna (right) and incident onto a cylindrical reflector (left) located about 1.5 m away. The resulting air breakdown reveals a standing wave pattern. The distance between striations is 1.6 cm, or half a wavelength. Figure 3 (bottom) presents an open shutter photograph of TM_{01} radiation exiting the vacuum window at the end of the conical horn antenna. The circular light is produced by an air breakdown about 3 cm downstream from the vacuum window. This light is consistent with a TM_{01} mode pattern. The light on axis is probably due to scattered radiation.[4]

FIG. 2. Open shutter photograph of neon bulb array, subjected to TM_{01} radiation (top) and TE_{11} radiation (bottom). (NOTE: Figure appears on the next page.)

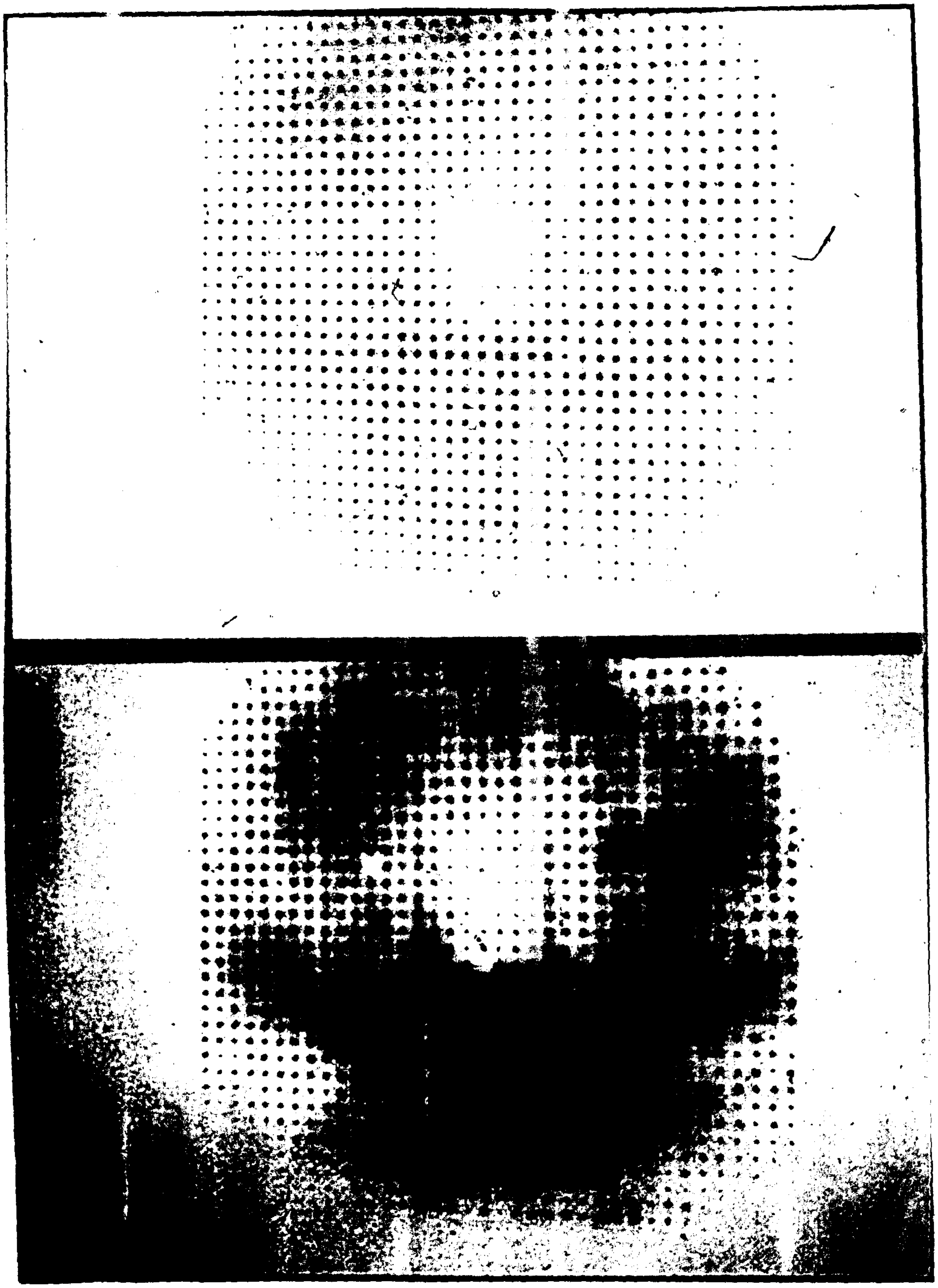

FIG. 3. Top: Open shutter photograph of TE_{11} radiation exiting the vacuum window at the end of the conical horn antenna (right) and incident onto a cylindrical reflector (left). Bottom: Open shutter photograph of TM_{01} radiation exiting the vacuum window at the end of the conical horn antenna. (NOTE: Figure appears on the next page.)

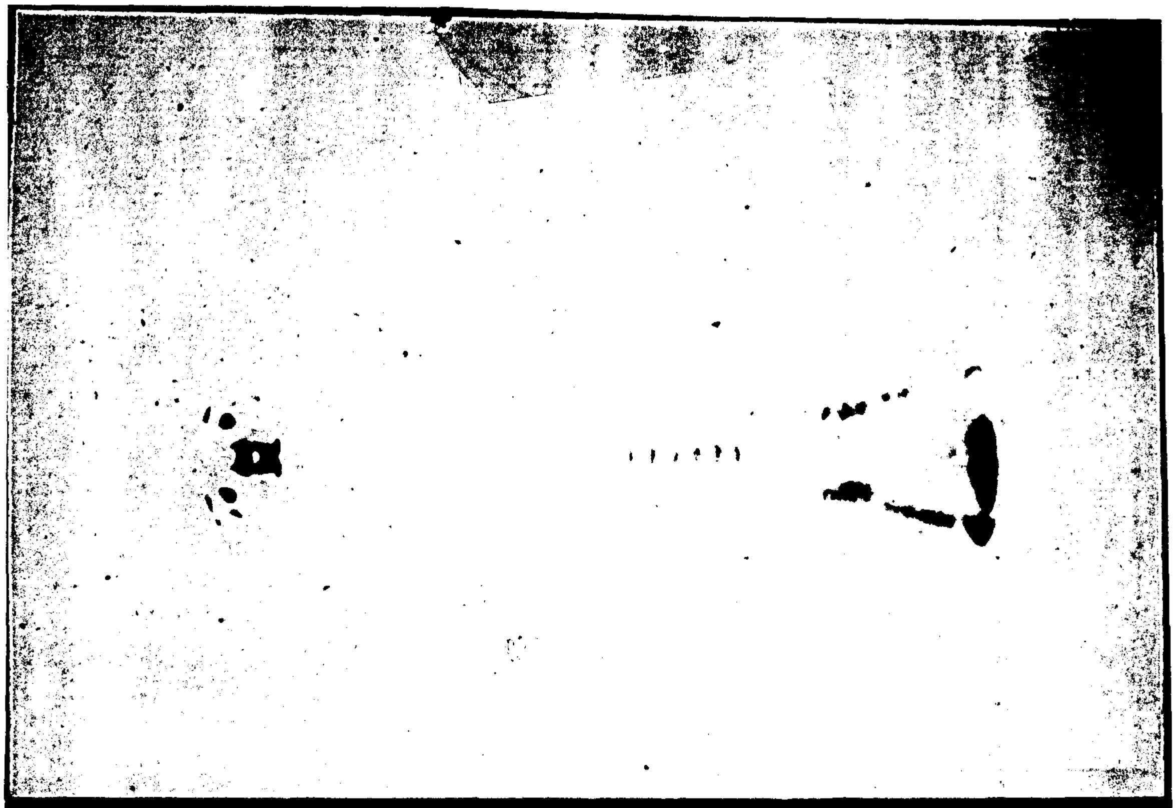

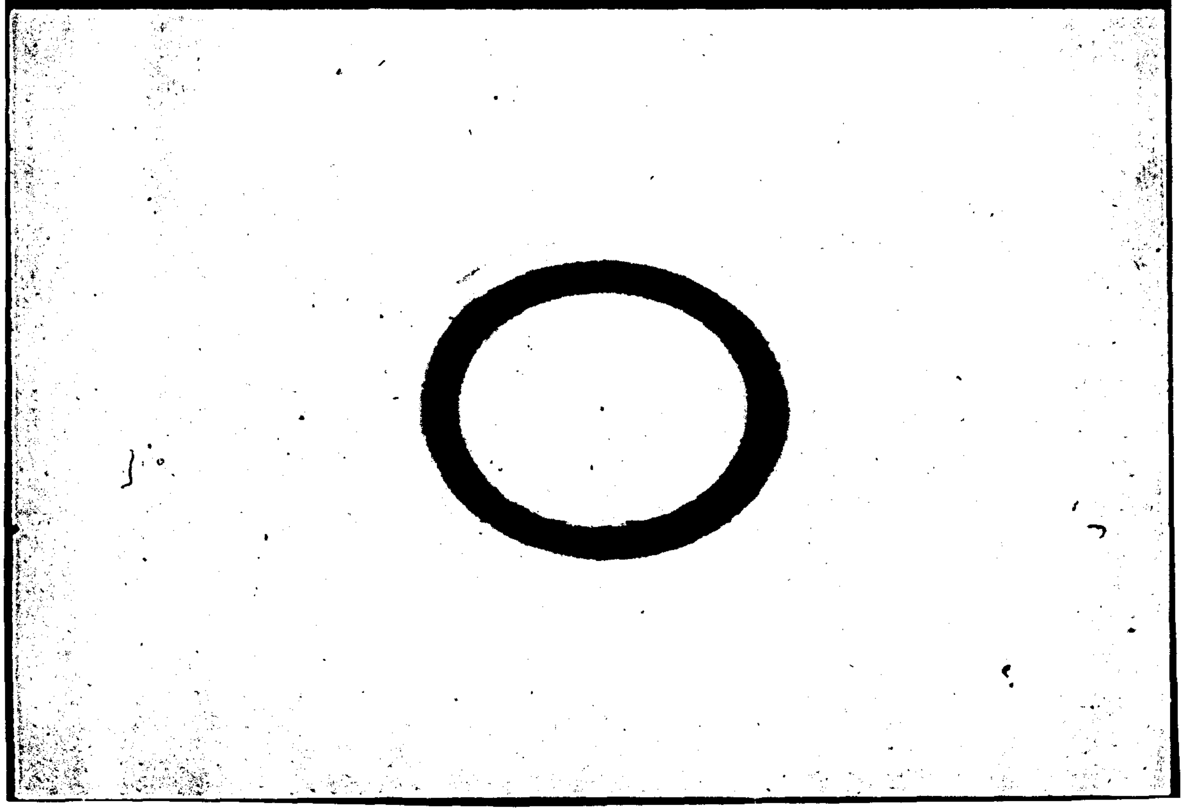

[illegible]

III. Long Pulse Vacuum BWO Experiments

During the past year significant progress has been made on the UNM Long Pulse BWO Experiment. By the end of the year all major components had been designed and constructed and were in place on the experiment. In addition, one or two new diagnostics were added, and presently work is being directed toward developing additional diagnostics.

A number of different experiments have been conducted with the apparatus during the past year with very promising results. Several experiments were performed at the beginning of June 1993 with only a make-shift horn antenna and a slow wave structure having a uniform ripple amplitude. Peak microwave powers of approximately 10 MW were observed in a TM_{01} mode with microwave pulse durations exceeding 100 ns. Later, after a proper horn antenna and beam dump were designed, constructed, and installed, slightly higher peak powers, somewhere between 30 and 45 MW, were measured, although at somewhat shorter pulse durations (40-50 ns FWHM). A slow wave structure having a nonuniform ripple amplitude, identical to that used in the Sinus-6 experiments, was also tested. In these experiments peak powers of up to about 140 MW were achieved, at approximately the same pulse durations.

A. Status of the PI-110A long pulse hardware

The accelerator used in the UNM Long Pulse BWO Experiment is a modified Physics International Pulserad 110A. An 11-stage Marx bank with an energy storage capacity of 2.75 kJ is used as the main energy store and initial pulse forming device in the accelerator. The Blumlein which previously followed the Marx bank has been replaced with an LC filter network. When erected, the Marx bank and the LC network together form a 2-stage pulse forming network (PFN).[5] An equivalent circuit for this is shown in Fig. 4. The pulse duration and impedance of the accelerator in this configuration are approximately 500 ns and 40 Ω, respectively. A balanced resistive voltage divider (not shown in the figure) has been placed between the Marx bank and the LC network to monitor the Marx voltage. The electron gun immediately follows the LC filter network, and its configuration is nearly identical to the

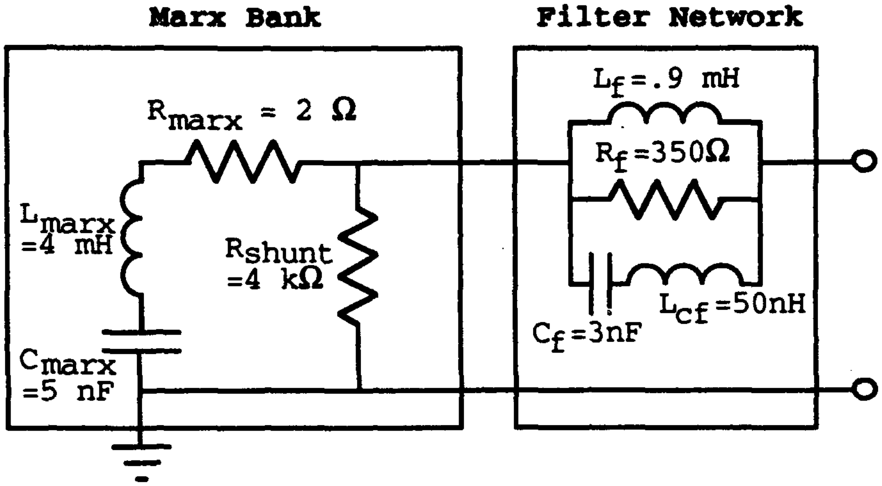

FIG. 4. Equivalent circuit of modified PI-110A.

one on the Sinus-6. The cathode holder is stainless steel and is curved to follow the magnetic field lines. At the end of the holder is a 2 cm-diameter carbon knife-edge tip from which an annular electron beam is emitted. Either 6 or 7 field coils can be placed around the slow wave structure to produce a guiding field for the electron beam. The field strength on axis is typically 30 kG. After traveling through the slow wave structure, the electron beam follows the magnetic field lines to the beam dump, which consists of a section of stainless steel screen surrounded by a larger, concentric section of copper pipe that is lined with carbon on its inner surface. The microwaves that are produced in the slow wave structure travel past the screen into another section of circular waveguide, and then to a conical horn where they are radiated into an *anechoic* measurement area.

Two Rogowski coils are used to monitor the beam current, one around the cathode holder and the other to be located just upstream of the beam dump. The latter monitor has not been installed, yet, but is currently being constructed along with a new coil to be placed around the cathode holder. Both of the new coils will be of the slow wave variety, discussed in Ref. 6. In addition, a capacitive voltage divider has recently been installed just behind the first Rogowski coil to enable measurement of the cathode voltage during experiments. To measure the microwave radiation, two different kinds of detectors have been used. One is a simple $\dot{B}$ probe which directly measures the magnetic field intensity of the microwave radiation. The other detector is similar to the one presently being used on the Sinus-6 experiments. It consists of a small piece of a semiconductor material placed inside a short section of waveguide (Fig. 5). Before the accelerator is fired, a negative voltage pulse having an amplitude of approximately 50 V and a duration of 100-120 μs is sent to the detector. When microwaves enter the waveguide and impinge upon the semiconductor, the impedance of the semiconductor changes, causing a ripple in the amplitude of the reflected voltage pulse. From the amplitude of the ripple the power density of the incident microwave radiation can be determined.

B. Discussion of long pulse vacuum BWO results

Vacuum BWO experiments have been conducted using slow wave structures with both uniform and nonuniform ripple amplitudes. At the beginning of June 1993 a

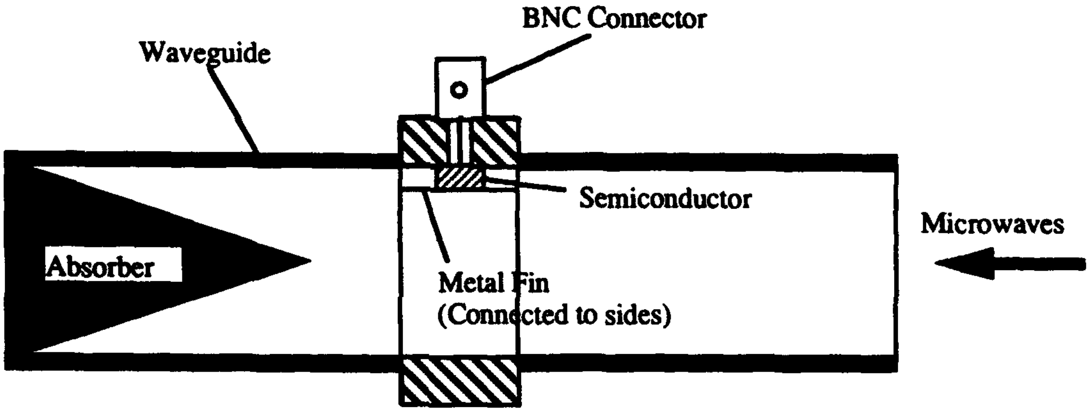

FIG. 5. Cross-sectional view of microwave detector based on semiconductor's response to fast electrons.

few experiments were performed before final assembly of the experimental apparatus was complete. Since the only component that was lacking was a horn antenna, a simple horn was constructed from copper sheet metal and attached to the waveguide following the slow wave structure. In these early experiments, in which the uniform slow wave structure was used, microwave pulses with FWHM durations exceeding 100 ns were observed. Typical signals from the first Rogowski coil and the microwave detector ($\dot{B}$ probe) are shown in Fig. 6. The radiated power was estimated to be about 10 MW. By positioning the $\dot{B}$ probe at various angles with respect to the center axis of the horn, a crude map of the radiation was obtained (Fig. 7). From this figure it is apparent that the radiation is emitted in the TM_{01} mode. Measurements were not made to determine the frequency of the radiation. However, several simulations of the slow wave structure were performed using the MAGIC 2.5-D particle-in-cell code, and the results indicate a frequency of approximately 10 GHz.

Additional experiments were performed with the uniform slow wave structure after a proper horn and beam dump had been installed. The power measurements, made with the second microwave detector, showed somewhat higher radiation levels, 30-45 MW, but with a somewhat shorter pulse duration, 40-50 ns FWHM. Experiments are now being conducted with a slow wave structure having a nonuniform amplitude, identical to the slow wave structure used in the initial Sinus-6 experiments. The power levels that have been measured are significantly higher, 130-140 MW, with pulse durations comparable to those observed in the more recent uniform slow wave structure experiments. A plot of the Rogowski coil and microwave detector signals from a typical experiment is given in Fig. 8. (The large positive overshoot in the detector signal is not real but an artifact of the filter used to block out the -50 V carrier pulse.) The microwave frequency has not been measured in these experiments thus far. However, it is expected to be similar to the 9.6 GHz measured in the Sinus-6 experiments.

Two problems have been encountered in these most recent experiments. One is that there are significant signs of rf breakdown in the slow wave structure following these experiments. The second is that, for the particular anode-cathode (A-K) gap spacing in these experiments, the current pulse ends abruptly (Fig. 8) and, therefore, halts the production of microwaves. For smaller A-K gap spacings (and therefore

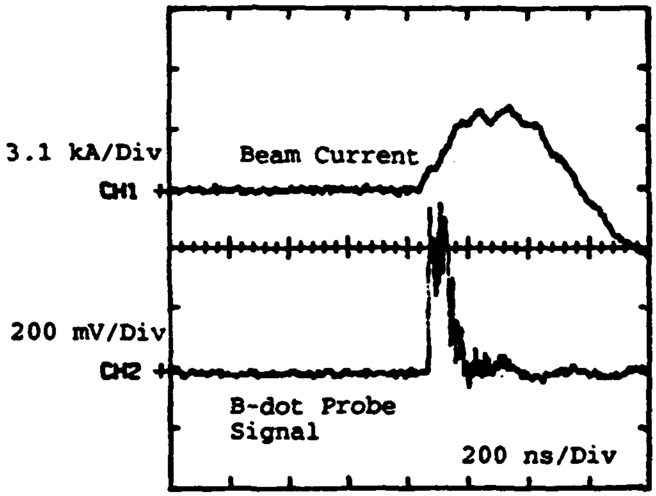

FIG. 6. Typical signals from the Rogowski coil (top) and the $\dot{B}$ probe (bottom).

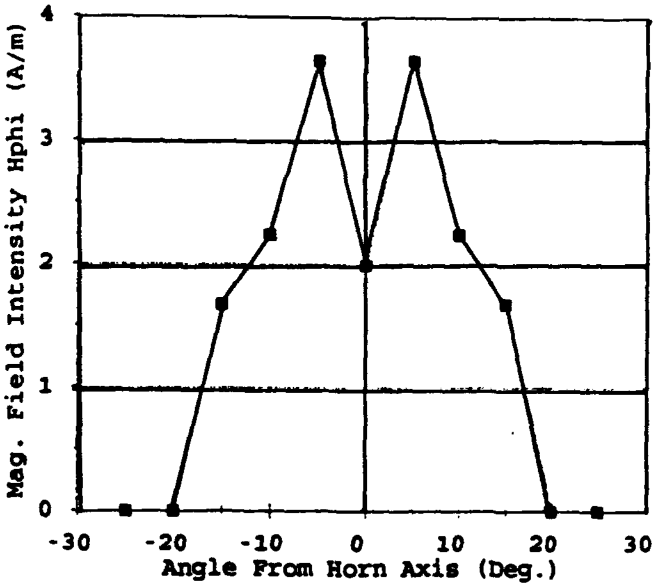

FIG. 7. Radiated magnetic fields measured by $\dot{B}$ probe 1.7 m downstream from the conical horn antenna. (Data for positive angles was mirrored to negative angles to better illustrate the radiation pattern.)

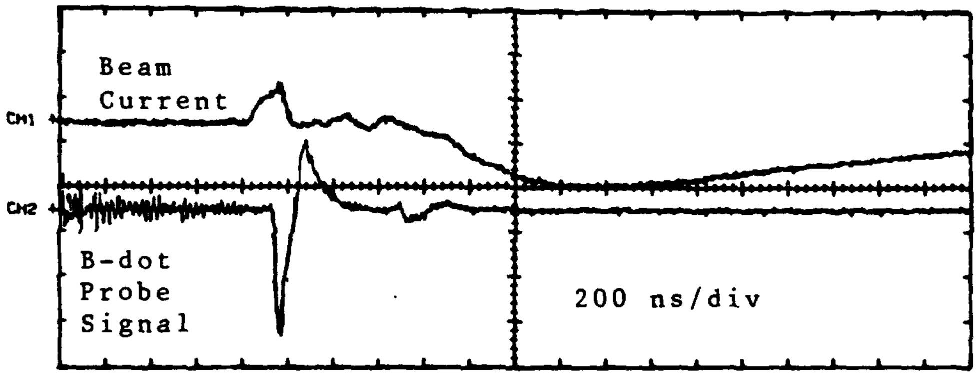

FIG. 8. Rogowski coil and microwave detector waveforms typical of most recent results.

a diode impedance which is more closely matched to the accelerator impedance) the current pulse has the expected duration (approximately 500 ns), but also a much higher amplitude, and the radiated microwave power is much less. Plans are underway to place several shunt resistors just before the diode and the vacuum-oil interface to allow the accelerator to operate more closely matched to the load conditions at the larger A-K gap spacing (diode impedance), as was done in Ref. 7.

IV. Ferroelectric Cathode Development

Ferroelectric cathodes are potentially a new source of electrons for high power, electron beam-driven microwave devices. These cathodes have the potential to extend the pulse duration of high power BWOs beyond the 100 ns regime. Typically high power BWO experiments utilize explosive emission cathodes. These cathodes form plasmas which can expand into the anode-cathode gap and hence cause a change in the diode impedance. Furthermore, plasmas and neutrals inherent to the explosive emission process can adversely affect the BWO interaction over time scales longer than 10's of nanseconds. Ferroelectric ceramics have the potential for providing sufficient current to operate a BWO without the above problems.[8]

Ferroelectrics are materials possessing a spontaneous electric dipole moment when the temperature is below the Curie temperature and above the Curie-Weiss temperature. Since these materials have a spontaneous dipole moment, ferroelectrics may be characterized by a bulk surface charge density which depends upon the magnitude and direction of the polarization of the sample. These materials are promising as advanced cathode materials because it is possible to liberate electron charge from the sample. The emission mechanism consists of the following sequence of events. The material is placed in a state very close to a phase transition. A large electric field is then applied across the cathode. If the electric field is of the proper polarity, a phase transition occurs, causing the cathode to become paraelectric and forcing the spontaneous electric dipole moment to zero. When the phase transition occurs, a large amount of surface charge remains momentarily unscreened on the surface of the cathode. This charge may be liberated as electrons.[8] For example,[9] the ferroelectric lead lanthanum zirconate titanate (PLZT) has a surface charge of 55 mC/cm^2, corresponding to about 10^{14} electrons/cm^2. Furthermore, since the amount of unscreened charge is initially quite large, the emission energy of electrons from the surface can lie in the kilovolt range. In this section, we report on the goals of the ferroelectric research and the progress which has been achieved at the end of the grant period. First, we review the geometry used in the experiments. Next, we review our work with unpoled ferroelectric samples. We have shown unambiguously that the emission process depends upon the state of the material and that the emission does not require an initially prepoled sample. Furthermore, with our advances in the understanding of the ferroelectric emission process, we envision the possibility of using the ferroelectric cathode as a charge-gated source.[10] Such a source would emit a constant amount of charge and would be capable of high peak currents. Following the work on electron emission from the ferroelectrics, we discuss several materials issues related to the use of thin films for the ferroelectric cathode.

A. Experimental configuration

The ferroelectric experiment consists of a ferroelectric sample placed in the triode configuration shown in Fig. 9. A circular grid 0.27 cm in diameter with 20% transmission forms the emitting surface on the top of the PLZT wafer. The thickness of the wafer is 0.33 mm and the grid and plate are separated by 2.7 cm. The cathode contact on the back of the wafer is grounded. The drive circuitry is also shown in Fig. 9. A bias voltage, used to produce a preset dipole moment in the sample, is applied to the grid, and the pulsed coercive field is applied through a coupling capacitor. A DC voltage of up to 20 kV is applied between the plate and the cathode contact. Current viewing resistors (CVRs) provide measurements of the grid current and plate current, while a current toroid and Rogowski coil have been used to measure current in the grid-cathode gap. Voltage measurements are obtained using resistive dividers.

We used PLZT 9/65/35 as the ferroelectric material for these experiments. The material was not prepoled; *i.e.* there was no permanent electric dipole moment or polarization in the sample. The surface was prepared to a quality suitable for electro-optics applications. Figure 10 shows a sample hysteresis curve taken at 60 Hz excitation frequency. The material exhibits a "soft" ferroelectric behavior. The remanent polarization is 1.5 mC/m^2 while the coercive electric field is 4 kV/cm. At saturation, the polarization is about 1.5 mC/m^2, corresponding to an electric field of 12 kV/cm. (Pulsed measurements using 300 ns risetime pulses show no change in these values.)

B. Experimental results

The novel aspect of these experiments is the application of the bias voltage to produce a known and variable polarization within the material. This configuration allows

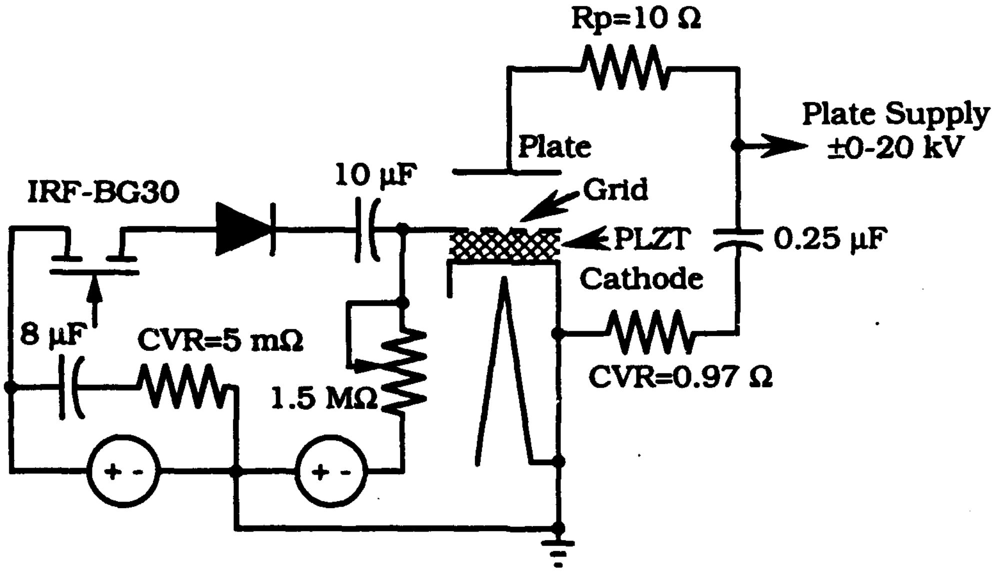

FIG. 9. Experimental configuration for ferroelectric cathode investigations.

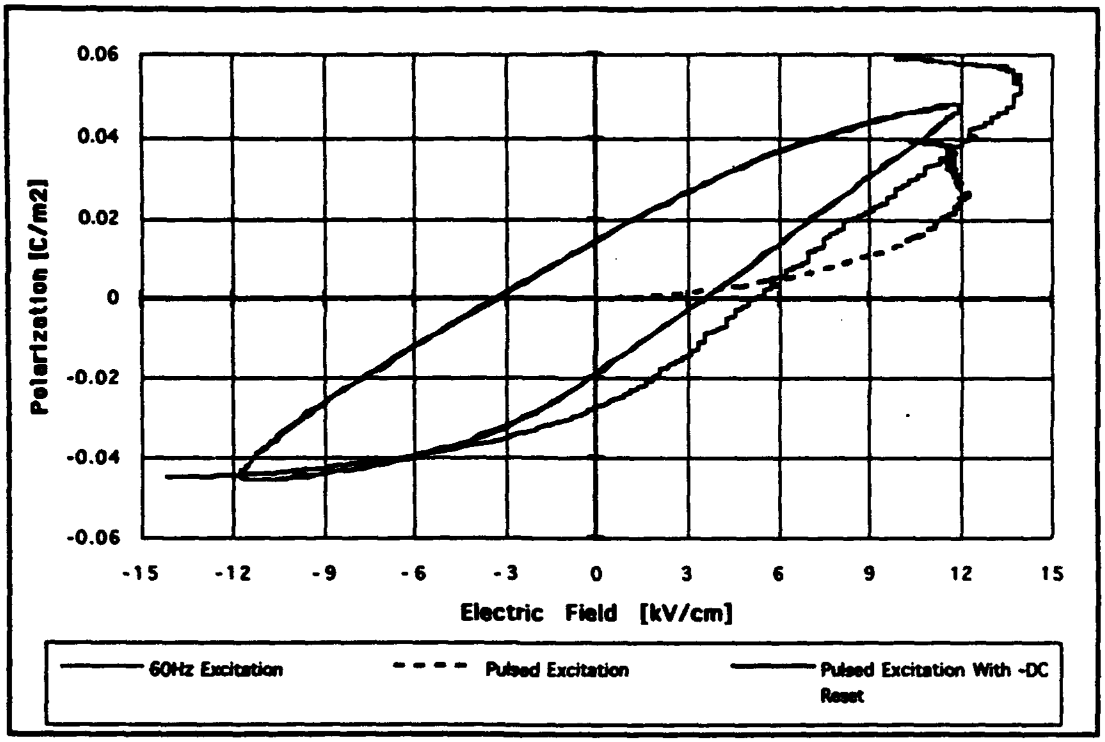

FIG. 10. Experimentally obtained hysteresis ($P - E$) curve.

one to change the initial position of the applied voltage on the hysteresis curve. We can thus, for the first time, control the state of the cathode in a known and easily quantified fashion. Experiments were performed both with no bias voltage (no initial polarization) and with a bias present. When no bias voltage was applied, current emission was erratic, although when emission did occur it was about 100 mA. By applying a bias voltage, current at the 100 mA level was seen on every shot. Furthermore, by changing the bias level, we were able to control the amount of emitted charge, and hence the current.

Figure 11 shows the grid voltage and current, and Fig. 12 shows the plate current during a typical shot with a bias voltage present. Note the change in slope of the grid voltage as the ferroelectric saturates, as well as the sharp drop in the grid voltage as the current emission begins. A delay of about 800 ns between the leading edge of the grid voltage and the leading edge of the plate (vacuum) current is present in all shots and is consistent with previous results.[9,10] From these traces we can see that the leading edge of the emission current pulse begins just before the ferroelectric is saturated and the emission ends as the material comes out of saturation. Hence, we see electron emission during a nonlinear portion of the hysteresis curve in which the relative dielectric constant is close to unity.

The charge emitted from the PLZT as a function of the applied electric field at the grid is plotted in Fig. 13. Ten measurements were taken at peak electric fields ranging from 6-14 kV/cm and the results are plotted with a best fit line. The emitted charge is measured by integrating the current to the plate. The graph indicates that more charge is emitted as the field at the grid increases, and that there is a threshold field of about 8 kV/cm below which no charge is emitted. It is important to note that, for each case, the reverse field is equal in magnitude to the forward field. In other words, the PLZT is excited from $-E_{sat}$ to $+E_{sat}$ during the grid pulse. The initial bound surface charge, as a result, increases as the applied field is increased. The graph in Fig. 13 suggests a strong link between the bound surface charge (which is equal to the initial polarization) and the emitted charge. As the field applied to the grid increases, the spread in the measured emitted charge increases. This effect correlates with variations in the width of the emitted current pulse. Although the current pulse begins consistently as the ferroelectric saturates, the emission interrupts

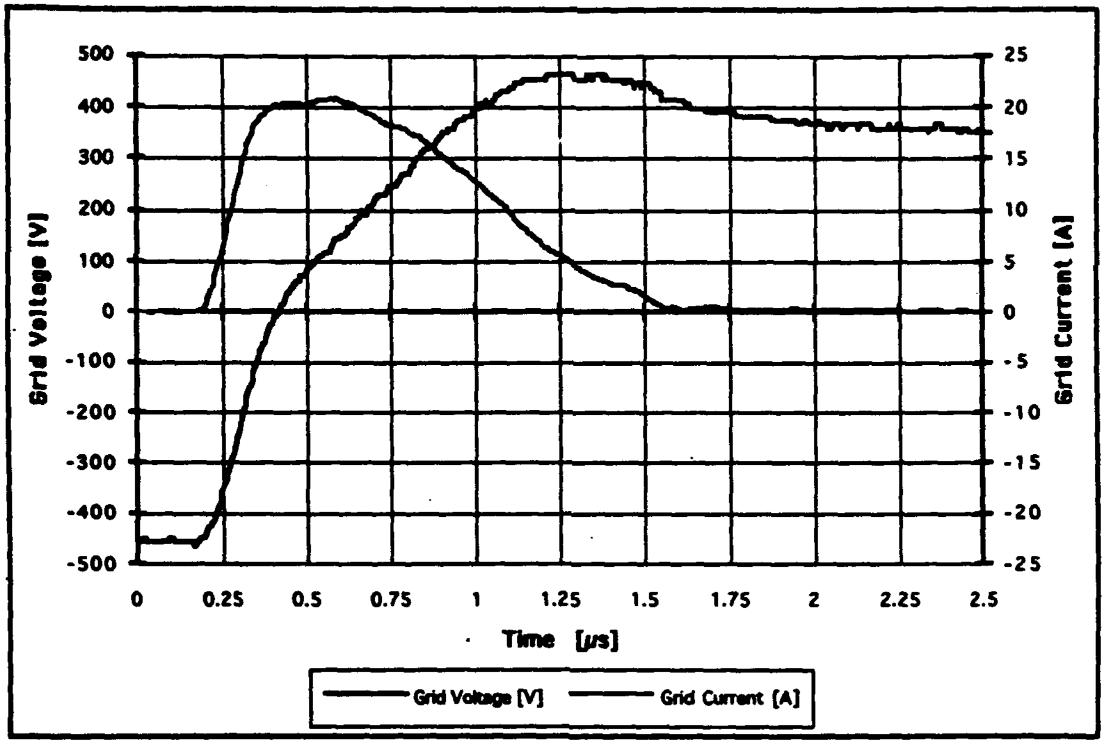

FIG. 11. Grid voltage and current.

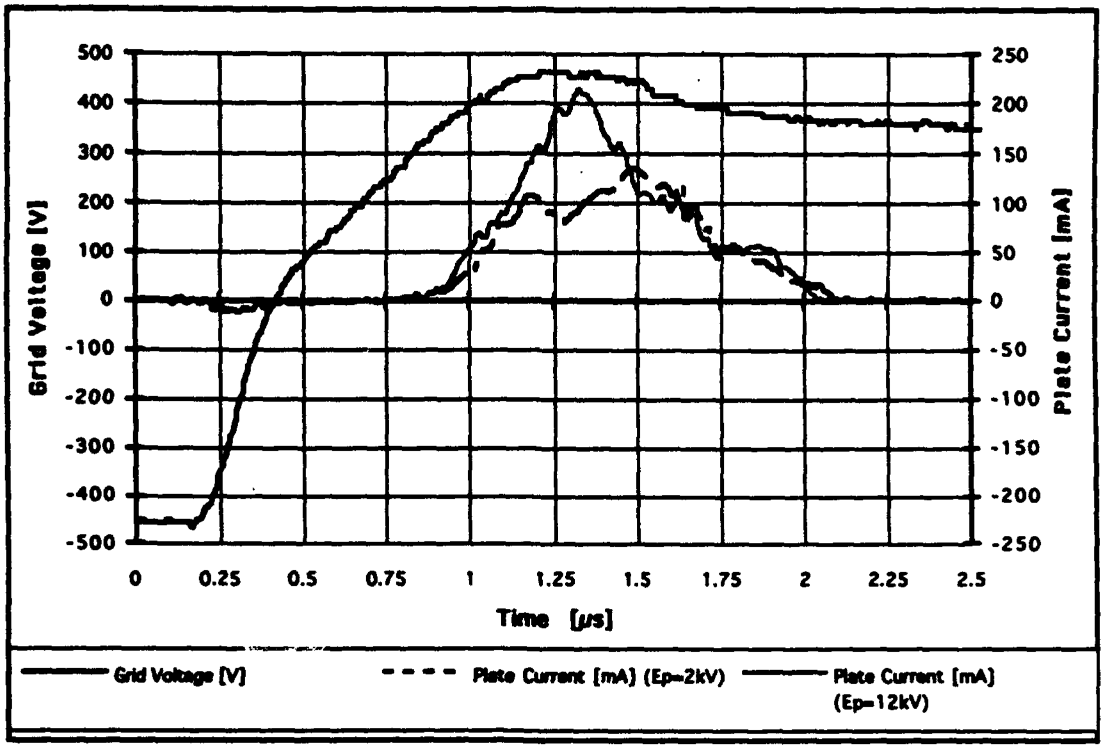

FIG. 12. Grid voltage and plate current.

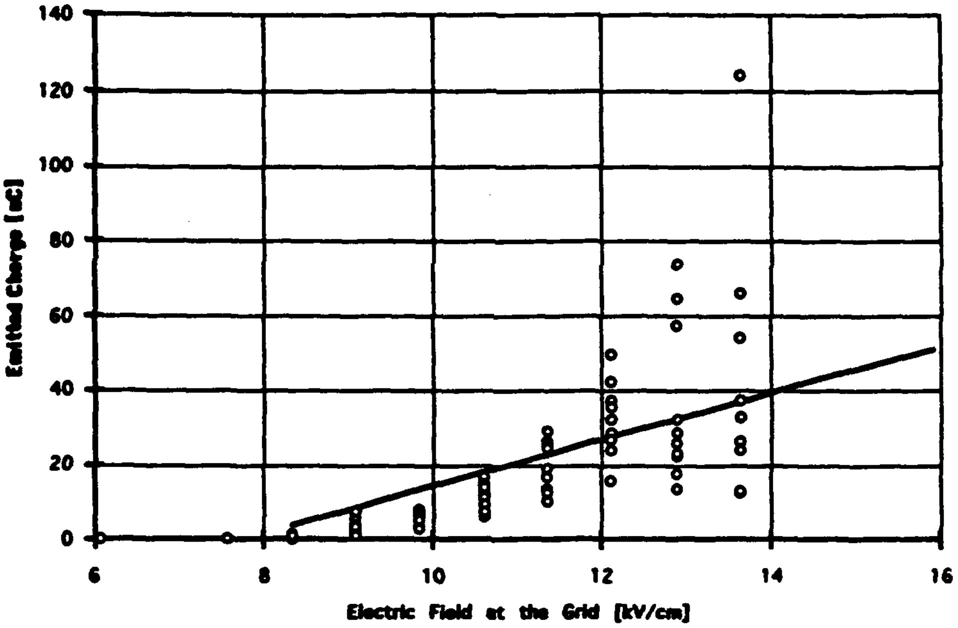

FIG. 13. Emitted charge as a function of the magnitude of the applied electric field.

irregularly as the material comes out of saturation.

These results have demonstrated several unique characteristics of ferroelectric cathodes. First, since emission depends on the bias voltage, we can see that the initial state of the PLZT clearly affects the emission process. To demonstrate this observation, a pulsed hysteresis ($P - E$) curve for the no bias case is included in Fig. 10. Although the sample has no initial polarization, the slope of the curve at the end of the pulse shows that the material is switching from remanence back to saturation. Under these conditions, emission from the PLZT was sporadic. The pulsed $P - E$ curve with a negative DC bias more closely matches the bottom half of the 60 Hz $P - E$ curve. With this excitation, emission is more regular. Secondly, emission does not depend on prepoling. Using a bias voltage to achieve the necessary bulk polarization is sufficient. Furthermore, by changing the bias we can change the emitted charge. Finally, emission occurs only when the ferroelectric becomes saturated. Note that the introduction of the bias potential is an important addition to ferroelectric cathodes, since one can now effectively gate the charge as well as change the state of the cathode material.

C. Bulk sample preparation

Before mounting the PLZT substrates into the vacuum chamber, a grid was applied to the surface using standard photolithographic techniques. A thin (0.5 mm) layer of gold was evaporated onto the surface using an electron beam evaporator. A layer of photoresist was spun onto the gold layer and exposed through a mask using a UV mask aligner. The mask consists of a series of dots, designed to yield a grid in the gold consisting of a gold surface perforated by a series of circular holes which expose the PLZT surface. After exposure, the photoresist is developed, and the excess gold is etched away using standard wet chemical etching methods.

D. Thin film preparation

Studies of thin film deposition of PLZT were initiated for eventual use as ferroelectric cathodes. The technology for deposition of thin films of this material is well developed for non-volatile memory applications. However, deposition of films for our application presents some unique challenges. Among the commonly used compositions for electronic applications is PLZT (28/1/100). However, the optimal composition for our application will be PLZT (9/65/35). These two compositions have different thermal expansion coefficients so the technology already developed for microelectronic applications will not necessarily work for our application.

Our thin films are deposited using ion beam sputtering with a Kaufman ion gun. Since the as-deposited films are in the pyrochlore phase (which is not ferroelectric), and are oxygen deficient, annealing in an oxygen ambient is essential. Sufficient annealing fully oxygenates the material and transforms the crystal structure to the ferroelectric perovskite phase. Annealing takes place in flowing oxygen at 650° C for two hours.

A number of substrate/buffer combinations have been studied for depositing high-quality 9/65/35 films. Initial work used stainless steel substrates and stainless steel coated with a thin platinum layer. After annealing, the PLZT films did not adhere well to the substrate. Bare silicon substrates were also studied. After annealing, these yielded continuous films, but with very poor surface morphology—some buckling of the films was evident, although these will probably be acceptable for use as a cathode. We are currently in the process of evaluating the use of silicon dioxide/platinum buffer layers for producing better quality films.

V. Plans for Future Work

Experiments with the Sinus-6 will continue to study the physics of efficient high power microwave generation in vacuum BWOs. Recent advances in the theoretical understanding of these devices are expected to yield uniform BWOs with microwave generation efficiencies approaching 50%. These results will then be compared with plasma-filled tubes to critically evaluate the merits of a plasma-fill in these tubes in the short pulse and repetitively-pulsed operating regime.

The Sinus-6 experimental and theoretical results will continue to feed into the PI-110A long pulse experiments. Once the shunt resistors have been placed in the modified PI-110A accelerator, as discussed above, and the new Rogowski coils have been constructed, experiments will begin to characterize the general behavior of the apparatus. The characterization will include precise measurements of the frequency of the microwave radiation, and the generation of a new map of the radiation profile in the far-field. In addition, the problem of breakdown in the slow wave structure will be addressed. It is anticipated that we will introduce thin film ceramic and metallic coatings within the inner wall of the slow wave structures to see if there is improvement in the vacuum breakdown strength under the influence of microwaves. (Please refer to the manuscript "Suppression of Vacuum Breakdown Using Thin Film Coatings" presented in Appendix B for a discussion of the breakdown strength of coatings.)

Work on the ferroelectric cathodes will continue because we believe that an alternative to traditional explosive emission cathodes will be one of the key advances that will yield successful long pulse vacuum and plasma-filled BWO operation. Now that we have demonstrated electron emission from a ferroelectric cathode, albeit at severely reduced electric field parameters, we plan to proceed in several areas. First, we plan to characterize the emitted electron beam in detail. These measurements will consist of determining the energy spread and emittance of the electron beam. Next, we wish to enhance the electron emission currents. To perform this study, we intend to sample different ferroelectric materials, as well as explore various grid geometries capable of enhancing the emitted current. Another important test is to attempt to achieve electron emission from thin films. Thin films, in principle, allow the production of an almost arbitrary electron beam shape which can be used to enhance the performance of any electron beam-driven microwave device. Theoretical studies will be initiated to contrast with an earlier theory[11] and to clarify the difference between the ferroelectric emission process and explosive emission observed earlier in ferroelectric dielectric cathodes.[12] Finally, we will begin the design and testing of a ferroelectric cathode to be tested on a relativistic BWO accelerator.

VI. References

1. N. F. Kovalev and V. I. Petrukhina, Electr. Techn. SVCH **7**, 101-105 (1977) (in Russian).
2. S. D. Korovin, S. D. Polevin, A. M. Roitman, and V. V. Rostov, to appear in Tech. Phys. Lett. (1994).
3. D. V. Vinogradov and G. G. Denisov, Radiofizika **33**, 726 (1990).
4. V. L. Bratman, G. G. Denisov, N. S. Ginzburg, A. V. Smorgonsky, S. D. Korovin, S. D. Polevin, V. V. Rostov, and M. I. Yalandin, Int. J. Electronics **59**, 247 (1985).
5. D. B. Cummings, *IEEE Conference Record of the Twelfth Modulator Symposium* (IEEE Cat. No. 76CH1045-4ED), pp. 142-146 (1976).
6. K. L. Wong and T. R. Chen, IEEE Trans. Plasma Sci.**18**, 219 (1990).
7. J. A. Swegle, R. A. Anderson, J. F. Comancho, B. R. Poole, M. A. Rhodes, E. T. Rosenbury, and D. L. Shaeffer, IEEE Trans. Plasma Sci. **21**, pp. 714-724 (1993).
8. H. Gundel, J. Handerek, and H. Riege, J. Appl. Phys. **69**, 2 (1991).
9. J. D. Ivers, L. Schachter, J. A. Nation, G. S. Kerslick, and R. Advani, J. Appl. Phys. **73**, 6 (1993).
10. H. Gundel, Integrated Ferroelectrics **2**, 207 (1992).
11. L. Schachter, J. D. Ivers, J. A. Nation, and G. S. Kerslick, J. Appl. Phys. **73**, 12 (1993).
12. S. P. Bugaev and G. A. Mesyats, Zh. Tekh. Fiz. **37**, 1855 (1967) (in Russian).

Appendix A. Conference Papers Accepted for Publication

To Appear in the Proceedings of the 9th IEEE International Pulsed Power Conference

EFFECTS OF USING A NONUNIFORM-AMPLITUDE SLOW WAVE STRUCTURE IN A REPETITIVELY-PULSED, HIGH POWER RELATIVISTIC BACKWARD WAVE OSCILLATOR.+ *

L. D. Moreland, E. Schamiloglu, R. Lemke,§ J. Gahl, D. Shiffler
University of New Mexico
Department of Electrical and Computer Engineering
Albuquerque, New Mexico 87131

Abstract

The University of New Mexico Pulsed Power and Plasma Science Laboratory is conducting a systematic investigation of nonuniform-amplitude backward wave oscillators (BWOs) using the SINUS-6, a high power relativistic repetitively-pulsed electron beam accelerator The Sinus-6 produces a 12 ns microwave pulse with a peak power of 600 MW at 9.6 GHz. Efficiencies of microwave generation using both uniform and nonuniform-amplitude BWOs are measured and compared with TWOQUICK (MAGIC) computer simulations. Each BWO structure is tested hundreds of times over a wide range of input parameters. The plentiful data allow for careful comparisons with theoretical models. Initial results confirm that prebunching the electron beam in a nonoscillating shallow ripple section results in increased microwave generation efficiency. Finally, experimental results from a high power serpentine mode converter based on a design of the Institute of Applied Physics, Nizhny Novgorod, Russia are also presented. The converter changes the dominant TM_{01} mode *output of the BWO to a* TE_{11} *mode with very high conversion* efficiency.

Introduction

There have been many experimental and theoretical studies of high power backward wave oscillators (BWOs) [1]. The majority of the work within the United States has used uniform amplitude and period slow wave structures. The efficiencies for converting input beam power into RF radiation using these devices have been reported to be as large as 15%. Work from the former Soviet Union on nonuniform BWOs has shown experimental measurements of RF efficiencies exceeding 40% and theoretical predictions indicate efficiencies may reach 75% [2,3].

This paper describes a systematic program at the University of New Mexico to investigate RF efficiencies of uniform and nonuniform BWOs using the *Sinus-6* repetitively-pulsed electron beam accelerator. The advantage of this accelerator is that it easily yields hundreds of BWO test shots in a single day, which allows for careful comparison of experimental results with theoretical calculations.

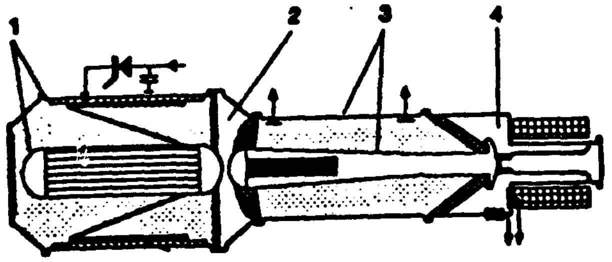

Fig. 1 Cut-away view of Sinus-6.

Sinus-6

The Sinus-6 (pronounced CEE-NUSS) is a high current, repetitively pulsed electron beam accelerator. Figure 1 is a cut-away diagram of the Sinus-6 with the following components: 1) Tesla transformer and pulse forming line which steps up the voltage from 300 V to 700 kV; 2) nitrogen-filled spark gap switch which is pressurized up to 18 atmospheres; by adjusting the nitrogen pressure, the spark gap voltage can be varied from 400 kV to 700 kV; 3) oil-filled adiabatic line which matches the 22 Ω input to a 100 Ω output; and 4) magnetically insulated coaxial vacuum diode with a cold explosive-emission graphite cathode. A magnetic field of 2.6 Tesla used to confine the electron beam is generated by a pulsed solenoid system. The pulsed system provides a magnetic pulse duration of 3 ms and requires 8 s to recharge. The Sinus-6 can rep rate its electron beam at 200 Hz but is currently operating at a single shot every 10 seconds, limited by the magnetic field system.

The electron beam pulse has a full width, half maximum (FWHM) temporal duration of 12 ns. Figure 2 shows voltage and current traces. By adjusting the pressure in the spark gap, cathode voltages from 400 to 650 kV were tested along with beam currents ranging from 3 to 5 kA.

For each different BWO structure, hundreds of test shots were made over the range of input parameters given above. The Sinus-6 provides a "work horse" to test many BWO structures over a wide range of input parameters. Within its first year of operation at the University of New Mexico, the Sinus-6 has accumulated over 10,000 single shots.

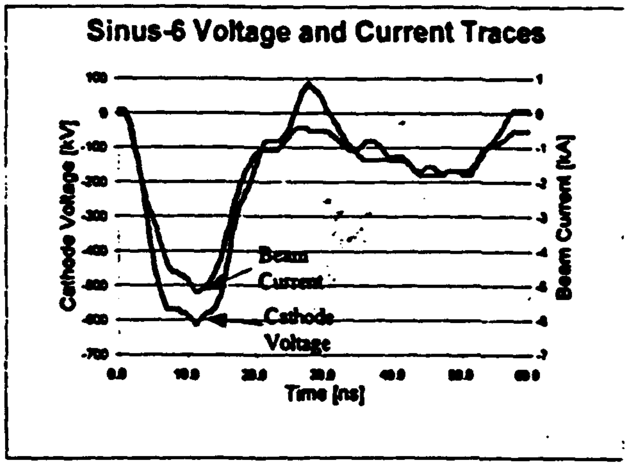

Fig. 2 Sinus-6 Voltage and Current Traces.

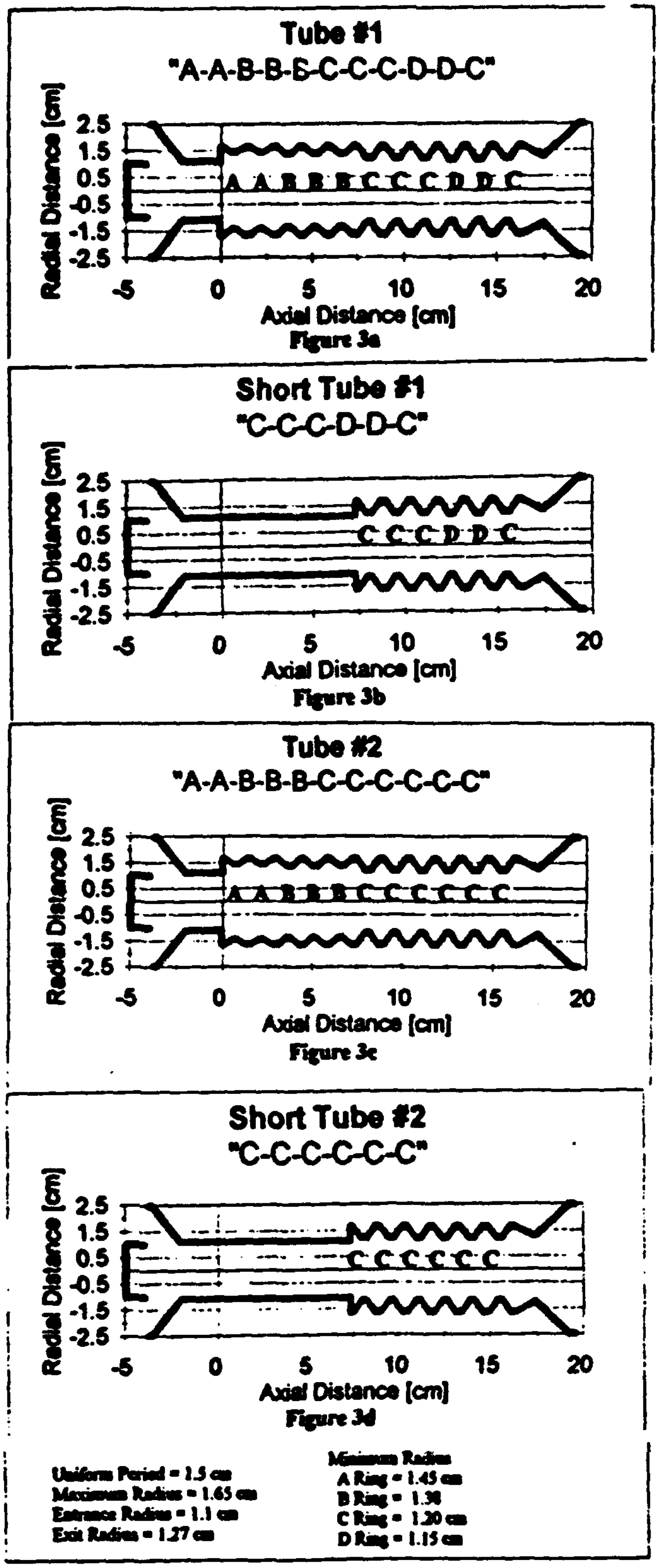

Fig. 3 Nonuniform-amplitude slow wave structures.

Nonuniform BWOs

Analysis has shown that nonuniform BWOs can be designed to operate more efficiently than uniform BWOs [2,3]. A nonuniform BWO can be constructed by varying the amplitude of the ripple in the slow wave structure, or by varying the period of the ripple. Varying the amplitude of the ripple changes the coupling resistance between the slow surface and the TM_{01} modes. Varying the period of the ripples changes the phase velocity of the slow surface wave. Our initial studies used a nonuniform-amplitude BWO structure provided by the High Current Electronics Institute, Tomsk, Russia. Figure 3a shows this structure. Variations of this structure were tested. The BWO structure is constructed from individual rings for each ripple period. In this manner, the structure can be quickly changed to any combination of ripple amplitudes. Each ring has a width of 1.5 cm (corresponding to a ripple period of 1.5 cm) and a maximum radius of 1.65 cm. Four different types of rings were used with ripple amplitudes of 1.0 mm, 1.35 mm, 2.25 mm and 2.5 mm. The original structure studied (referred to as Tube #1 and shown in Fig.3a) has two sections, a first section with shallow ripples followed by a second section with deeper ripples. A variation of this tube is Short Tube #1 where the shallow first section is eliminated, as shown in Fig. 3b. A second variation of our original tube is shown in Figs. 3c and 3d where the amplitude of the six ripple periods of the second section are the same. These tubes are referred to as Tube #2 and Short Tube #2.

Experimental Results

Variations in Slow Wave Structure Amplitude

We now present experimental data in which the BWO sections were tested separately. The RF efficiency was obtained by dividing the maximum total RF power divided by the total peak input beam power (cathode voltage multiplied by beam current). When the shallow section was tested alone, no RF radiation was detected with beam currents up to 4.5 kA. When the second stage of deeper ripples was tested alone (Short Tube #1), the RF efficiency was plotted as a function of input beam power in Fig. 4 and has a maximum RF efficiency of about 5%. The full BWO (Tube #1) results are plotted in Fig. 5 and indicate a maximum efficiency of 25 to 30%. The results for Tube #2 and Short Tube #2 are shown in Figs. 6 and 7. When the RF efficiencies for Tube #1 and Tube #2 are compared with beam current, as shown in Figs. 8 and 9, the maximum RF efficiency occurs at approximately twice the start current.

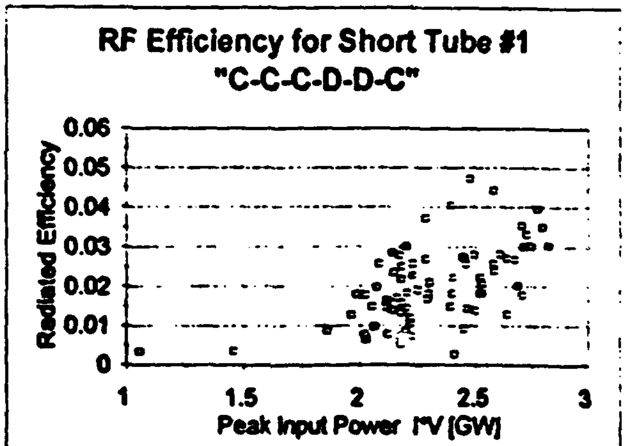

Fig. 4 RF efficiency for short tube #1.

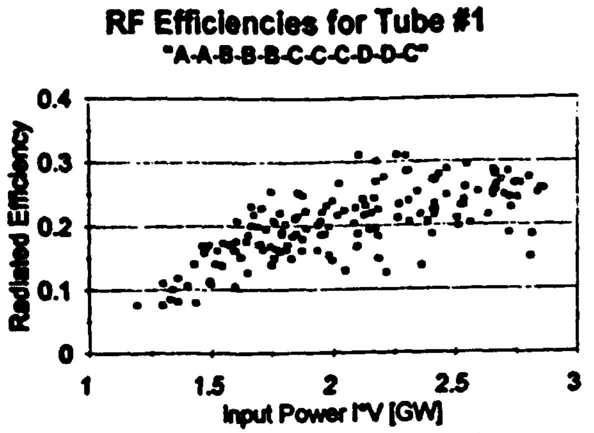

Fig. 5 RF efficiency for tube #1.

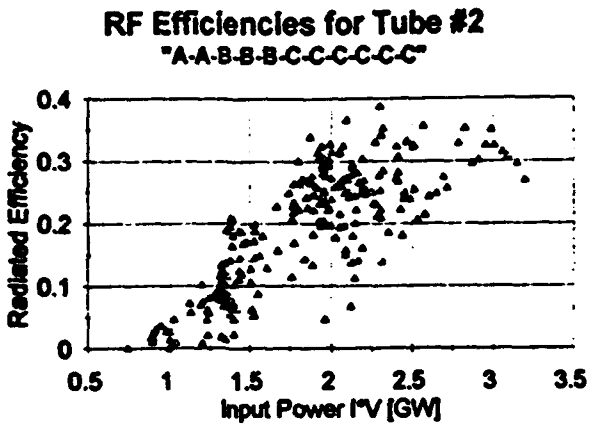

Fig. 6 RF efficiency for tube #2.

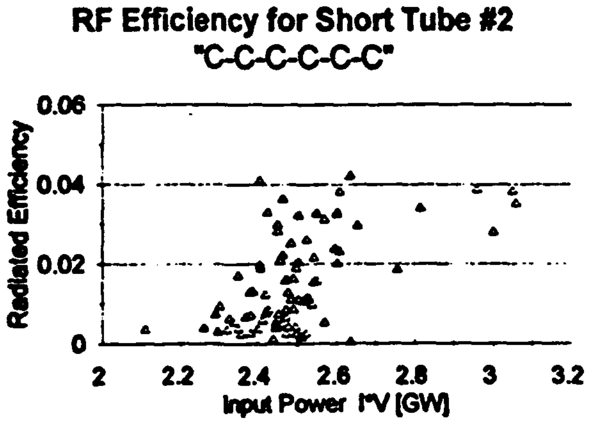

Fig. 7 RF efficiency for short tube #2.

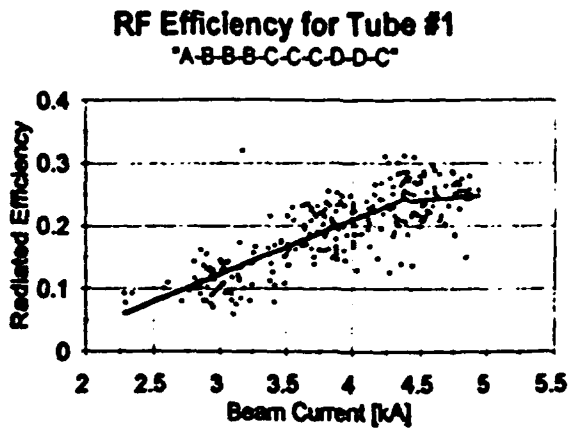

Fig. 8 RF efficiency for tube #1.

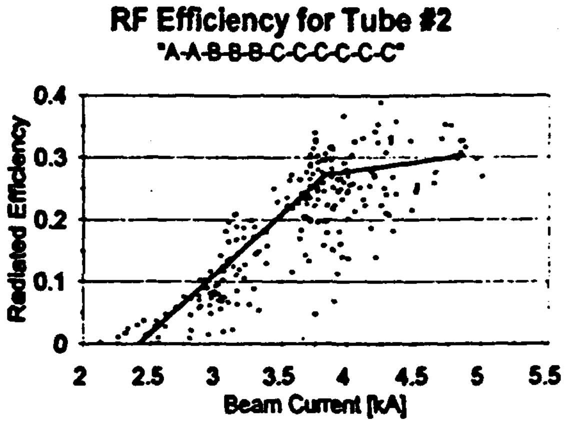

Fig. 9 RF efficiency for tube #2.

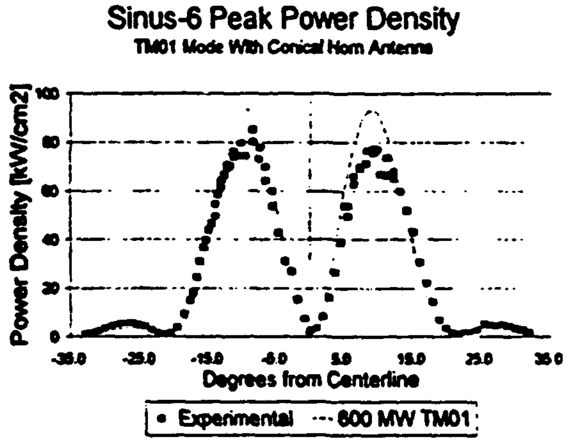

Fig. 10 TM_{01} radiation pattern.

Mode Conversion

The TM_{01} mode is the dominant mode in the slow wave structure. A conical horn antenna with a diameter of 15 cm was used to radiate the RF energy. Power density measurements were made in the horizontal plane at a distance of 1.7 m from the horn aperture. Using the nonuniform-amplitude BWO (Tube #1), the radiation pattern from the TM_{01} mode is shown in Fig. 10. The measurements in Fig. 10 are compared with the calculated radiation pattern from a 600 MW TM_{01} source [4]. Next a mode converter based on a design of the Institute of Applied Physics, Nizhny Novgorod, Russia was used to convert the TM_{01} mode to a TE_{11} mode [5]. The measured radiation pattern using the mode converter is shown in Fig. 11 and compared with a Gaussian radiation pattern of 600 MW total power and a half power beam width of 12 degrees. The mode conversion efficiency was nearly 100% within the limits of experimental error. The Gaussian-like radiation pattern is useful for applications, such as high power radars [6].

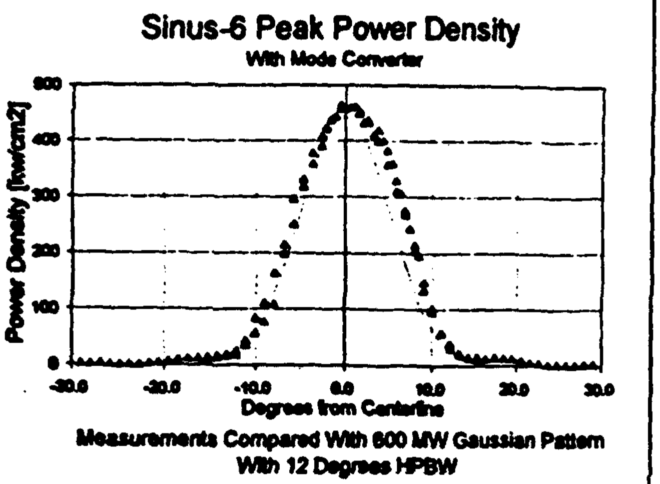

Fig. 11 Radiation pattern from mode converter.

MAGIC Comparisons

Sandia National Laboratories' version of MAGIC, TWOQUICK, was used to perform computer simulations to compare with experimental results. The computer simulations allow "snapshots" to be taken of the BWO operation. By calculating and plotting the charge density of the electron beam throughout the tube, the slow surface wave on the beam can be observed, as shown in Fig. 12. These results indicated that the surface wave has a wavelength equal to approximately 1.5 ripple periods. By plotting the intensity of the longitudinal electric field within the tube, the volume mode of the tube can be observed. The wavelength of the volume mode is approximately equal to 3 ripple periods. The tube is overmoded and the extraction of power through the volume mode minimizes microwave breakdown problems.

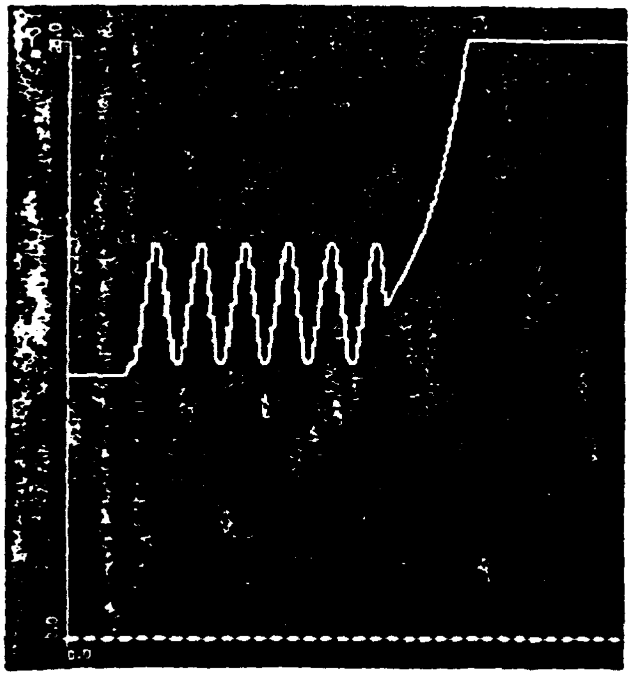

Fig. 12 Electron beam density from TWOQUICK (MAGIC) simulation.

Simulations provided good agreement with experimental measurements of the operating frequency of the BWOs. Simulations confirm that the first stage of shallow ripples in the original two-section structure does not oscillate. Simulations also indicate that efficient BWO operation occurs when the beam current is approximately twice the starting current for the oscillating section, consistent with experimental measurements. Simulations could not predict actual operating efficiencies in all cases due to resonance effects associated with artificially low power losses in the ideal model. However, the scaling appears to be in agreement provided that the tubes are not oscillating in the vicinity of a cavity resonance in the simulations.

Conclusions

The nonuniform-amplitude BWOs tested resulted in peak RF efficiencies of 25 to 35%. The maximum values for RF efficiencies occurred at approximately twice the start current, consistent with computer simulations. When the two sections were tested individually, the first shallow ripple section did not radiate measurable RF power and the second deeper ripple section showed RF efficiencies of less than 5%. The increased efficiency of the two section BWOs can be attributed to the prebunching of the electron beam by the nonoscillating first section.

TWOQUICK MAGIC simulations provided insight into the interaction of the surface mode and volume mode inside the slow wave structure. Simulation results were sensitive to the cavity Q's of the set-up. Agreement with experimental measurements were good when the simulations were not near resonance.

A high power serpentine mode converter resulted in power densities as large as 450 kW/cm^2 being measured 1.7 m from the radiating antenna. The TM$_{01}$ to TE$_{11}$ conversion efficiency was nearly 100%, consistent with theoretical predictions [5]

+ In collaboration with the High Current Electronics Institute, Tomsk, Russia.
* Research supported by AFOSR Grant # F49620-92-J-0157DEF
§ Sandia National Laboratories, Albuquerque, NM

References

[1] See, for example, J. Benford and J. Swegle, High-Power Microwaves. Boston: Artech House, 1992 and references therein.

[2] N. F. Kovalev, V. I. Petrukhina, and A. V. Smorgnoski, Radiotekh Elektron. 20, 1547 (1975).

[3] S. D. Korovin, S. D. Polevin, A. M. Roitman, and V. V. Rostov, "Relativistic backward wave tube with variable phase velocity," Sov. Tech. Phys. Lett. 18(4) (1992).

[4] R. A. Koslover, Computer code "TM0n" (SEAC, Albuquerque NW) (1988).

[5] D. V. Vinogradov and G. G. Denisov, "The conversion of waves in a bent waveguide with a variable curvature," Radiofizika, 33, 726 (1990).

[6] G. A. Mesyats, paper presented at the 1992 IEEE Microwave Theory and Techniques Society Symposium, Albuquerque, NM, June 2, 1992.

To Appear in Proceedings of the 9th IEEE International Pulsed Power Conference

LONG-PULSE HIGH POWER MICROWAVE EXPERIMENTS

C. Grabowski, J. Gahl, E. Schamiloglu, and D. Shiffler
Department of Electrical and Computer Engineering
University of New Mexico
Albuquerque, NM 87131

Abstract--Experiments to develop a long-pulse, high power microwave source are currently being conducted at the University of New Mexico (UNM). By removing the Blumlein in a PI Pulserad 110A and replacing it with a parallel L-C network, the Pulserad has been converted into a type A PFN.[1] The new pulse length, output voltage, and impedance of the device are approximately 450 ns, 500 kV, and 40 Ω, respectively. This modified Pulserad is used to drive an electron beam diode which is identical to the diode in the UNM SINUS-6 accelerator.[2] The relativistic electron beam produced by the diode is injected into a slow-wave structure to generate X-band microwaves at a frequency similar to that of the UNM SINUS-6. In addition, the output voltage and current are also similar for the two accelerators; however, the UNM SINUS-6 is a short-pulse, rep-rated accelerator while the UNM Pulserad is a long-pulse, single-shot machine. The primary objective of these experiments is to determine whether the backward wave oscillator (BWO) presently on the SINUS-6 machine can operate at long pulse durations. Initial experiments involve vacuum BWO operation, which will be followed by plasma-filled BWO operation. The system design will be presented along with electron beam diagnostic and microwave generation results.**

I. Introduction

In the past several years interest in high power microwaves has grown considerably. Devices have been developed which have peak powers on the order of terawatts. Increasing the average powers of these devices, though, has proved to be more difficult. In the case of long-pulse backward wave oscillators (BWO's) microwave generation simply ceases after a period of time even though the electron beam continues to travel through the slow wave structure.

At the University of New Mexico a long-pulse accelerator has been developed to drive a BWO for the purpose of investigating this phenomenon further. The electron gun of the BWO is nearly identical to that of the UNM SINUS-6, a short-pulse, rep-rated accelerator also at the university. Experiments are being conducted which involve both vacuum and plasma-filled BWO operation, and a portion of this study will be focused on understanding the behavior of the plasma and the interactions between the electron beam and the plasma in plasma-filled BWO operation.

This paper will discuss the work that has been completed thus far. In section II a description of the accelerator and the BWO will be presented, followed by a discussion of some of the preliminary results in section III. Section IV will present the conclusions drawn from this work and list the plans for future work. Acknowledgments are made in section V.

II. Experimental Design

The accelerator for the experiment has been constructed using a Physics International Pulserad 110A. Inside the Pulserad 110A is an 11-stage Marx bank, which has a capacitance of 0.05 μF and a maximum charging voltage of 100 kV for each stage. This translates to a maximum energy storage capacity of 2.75 kJ. The blumlein following the Marx bank was removed and replaced with a parallel L-C network. Both the Marx bank (when erected) and the L-C network together form a type-A PFN which has a pulse width and impedance of approximately 450 ns and 40 Ω, respectively. An equivalent circuit is shown in Fig. 1. A balanced resistive voltage divider, which is not shown in Fig. 1, has been placed between the Marx bank and the filter network to monitor the Marx voltage. PSPICE calculations show that with a matched load a peak voltage of 775 kV can be obtained from the Marx bank after it has been erected, resulting in a cathode voltage and load current of 570 kV and 14.3 kA, respectively (Fig. 2).

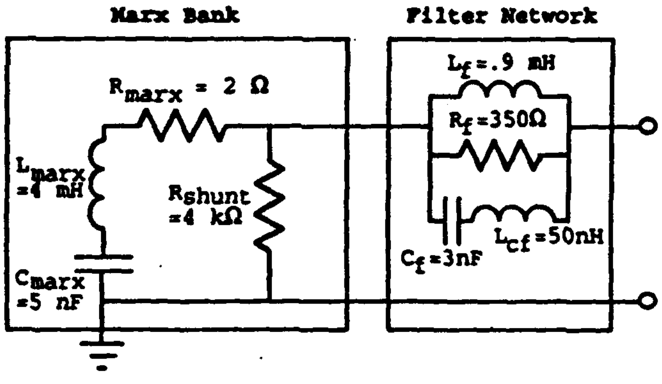

Fig. 1 Equivalent circuit of Pulserad 110A.

As was mentioned previously, the electron gun used with the Pulserad 110A is nearly identical to that on the UNM SINUS-6. The major difference between the two is that the slow wave structure in the gun on the Pulserad 110A is slightly different. Figure 3 shows a diagram of the gun. The cathode is stainless steel and has a 1.95 cm diameter knife-edge tip to emit an annular beam into the slow wave structure. As can be seen from the drawing the cathode is inserted some distance into the magnetic field so that electrons are emitted on uniform field lines. The maximum field that can be produced on axis by the field coils is approximately 3 T. Two Rogowski coils are shown in the diagram which are used to measure the beam current, one around the

---

***Research supported by AFOSR grant #F49620-92-J-0157DEF.*

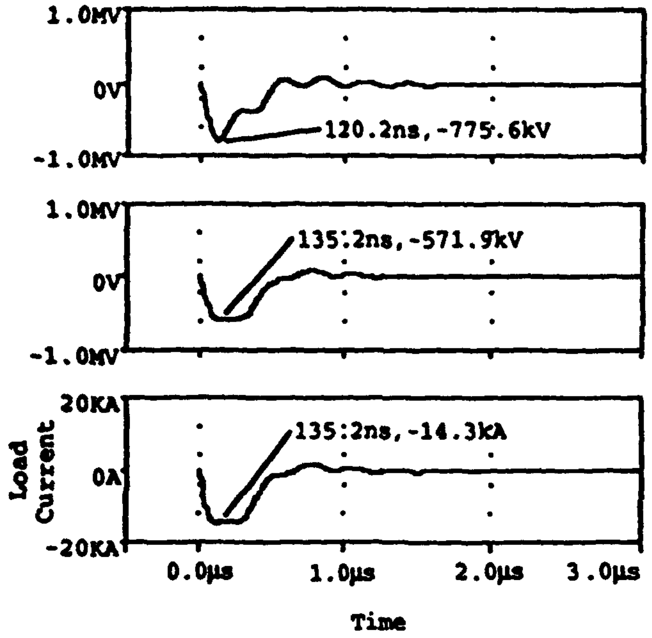

Fig. 2 Voltage and current waveforms calculated by PSPICE for the Pulserad 110A fully charged and terminated into a 40 Ω load.

cathode, which is currently installed, and one at the end of the slow wave structure, which will be installed in the near future. The coil used is a standard non-integrating Rogowski coil, requiring an RC integrator at the input of the oscilloscope to process the signal. Finally, following the slow wave structure is a conical horn which radiates the microwave power.

III. Discussion of Preliminary Results

Cathode Voltage and Beam Current

During experiments in which the Marx bank was charged to full voltage the signal waveform from the voltage divider indicated a peak voltage from 520 to 620 kV, which is slightly less than the PSPICE prediction of 775 kV for the 40 Ω load. Assuming that the ratio of the cathode voltage to the Marx voltage remained the same as that which PSPICE predicted, the cathode voltage was then in the range of 380 to 450 kV.

A beam current of 3.8 to 4.2 kA was consistently observed with the Rogowski coil. Pulse widths (measured at the base of the current pulse) varied from 530 to 560 ns. These values are in very good agreement with the pulse widths predicted by PSPICE in Fig. 2.

Mode Pattern

Two diagnostic methods were used to determine the mode pattern of the microwave radiation. The first and simplest method was to place a sheet of foam with a matrix of small neon bulbs embedded in it in the far-field region in front of the output horn. The room was darkened and an open-shutter camera was then used to take photographs of the light board as the Pulserad was fired. Figure 4 shows one of the photographs that were taken. In this particular case the Pulserad 110A was fired 7 times before closing the camera shutter. A small dark region can clearly be seen in the center of the light board surrounded by a rather broad lighted region which is in turn surrounded by another dark region. This pattern is characteristic of the TM_{01} radiation mode.

A second diagnostic used to evaluate the mode pattern was a B-dot probe. The probe was mounted on a wooden stand and positioned on

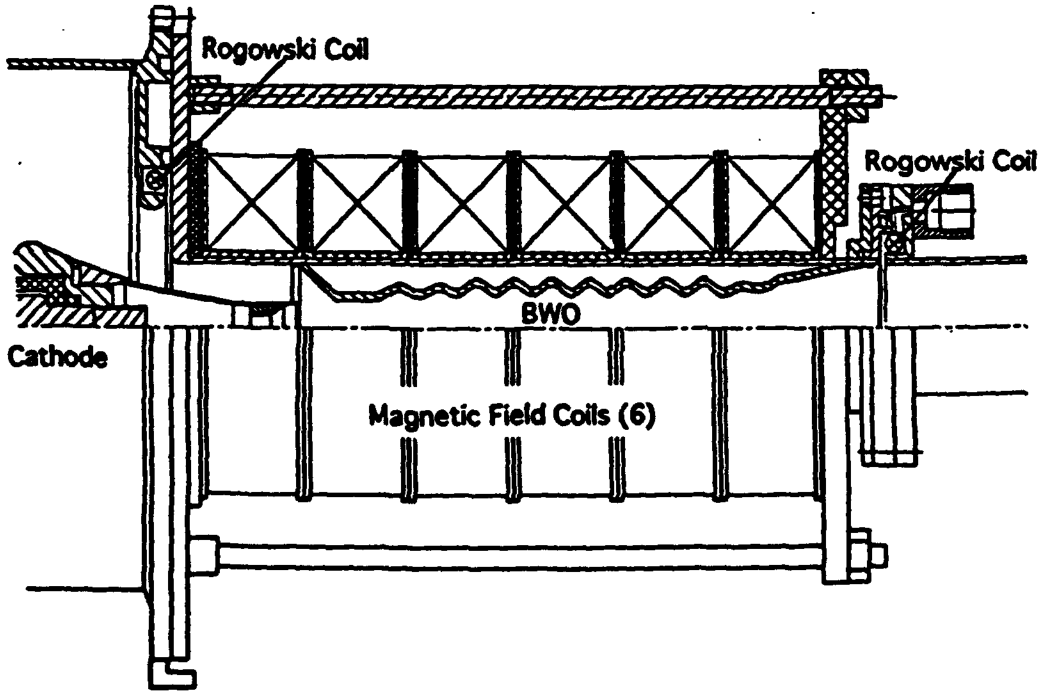

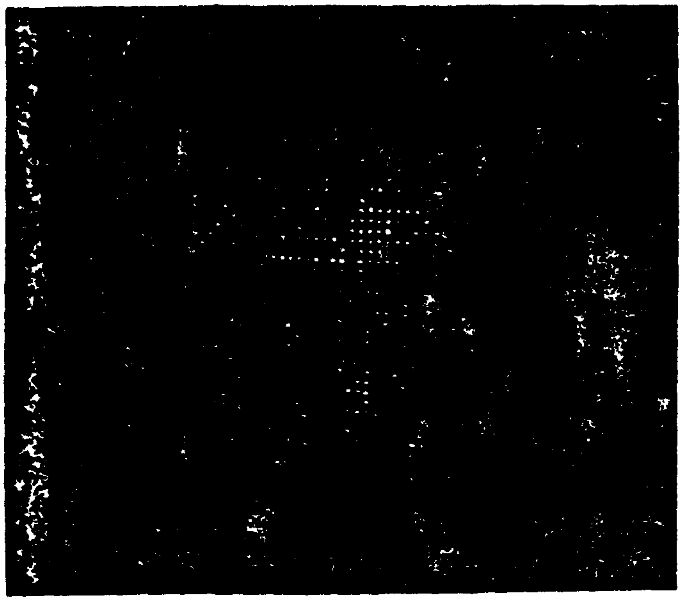

Fig. 4 Photograph of light board showing pattern for TM_{01} mode illuminated.

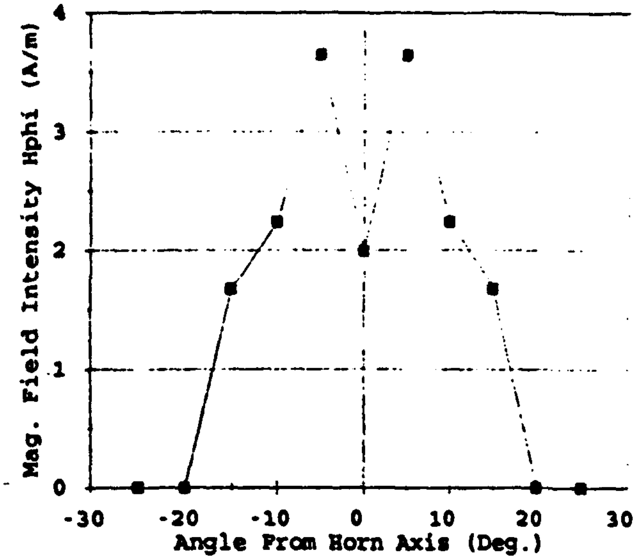

Fig. 6 Radiated magnetic fields measured by B-dot probe at 1.7 m from horn aperture. Data for positive angles was mirrored to negative angles to better illustrate radiation pattern.

the axis of the microwave horn at the same distance at which the light board was set. Measurements were taken and then the probe was moved to the left or right in increments of 5 degrees away from the horn axis. One of the recorded signal waveforms from the B-dot probe is shown in Fig. 5 along with the current waveform for the same shot. The early cessation in the production of microwaves, which was mentioned earlier as a characteristic of BWO's, is clearly seen here; the current pulse has a duration of 540 ns, while the duration of the microwave pulse is only 130 ns, over 4 times shorter.

Because of the large amplitude of the microwave signal from this shot and other similar shots, several layers of attenuating material were placed in front of the output horn, since the crystal detector used with the probe behaves very non-linearly for large input signals. As shown in the plot of probe data in Fig. 6, the signals from the B-dot probe were generally in agreement with the photograph in Fig. 4 and indicate the presence of the TM_{01} mode. The perturbation in the recorded data in comparison to the ideal TM_{01} pattern may have been caused by scattering of the microwaves as they passed through the attenuating material or the decreased radiation intensity bringing the probe signal closer to the noise floor.

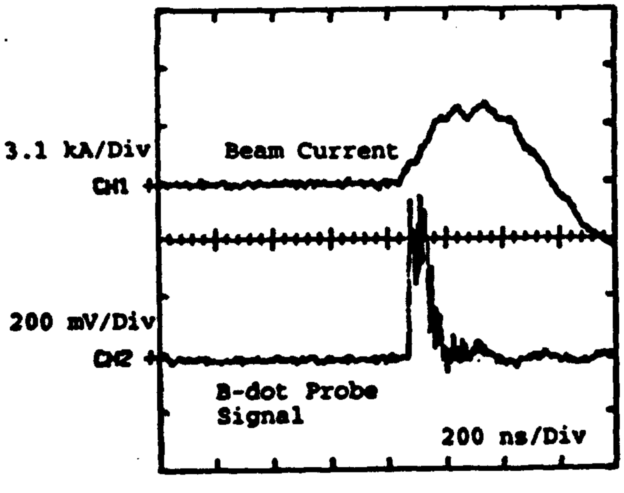

Fig. 5 Typical signal waveforms from the Rogowski coil and B-dot probe.

Microwave Power and Frequency

Although the radiated power could not be calculated exactly from the experimental data, it was estimated to be less than 10 MW. Another estimate of the power was obtained using MAGIC, a 2 1/2 D particle-in-cell simulation code.[3] Figure 7 shows a plot from MAGIC of the power over a 10 ns time period calculated for the case with a cathode voltage of 350 kV and a beam current of 4 kA. The power rises to almost 80 MW after about 1.5 ns but then rapidly drops. Over a duration of 130 ns the average power would seem to be on the order of 10 MW, which agrees well with the estimate from the experimental data. By setting the oscilloscope on a faster time scale when recording the B-dot probe signals (say, 5 ns/div instead of the 200 ns/div used for most of the present measurements) the high initial powers could be confirmed.

For this cathode voltage and beam current MAGIC calculates a value of approximately 7 GHz for the dominant microwave component. However, other MAGIC runs for other cathode voltages and beam currents show the dominant frequency component to be 10 GHz. Using a Mathmatica routine written by Tom Spencer at Phillips Lab for calculating the cold dispersion relation of a slow wave structure [4], a frequency of 10.8 GHz was predicted for the microwave radiation.

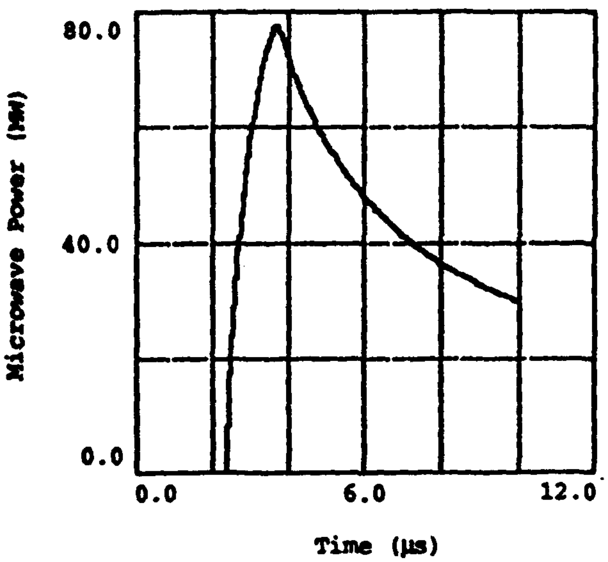

Fig. 7 Time history of radiated microwave power calculated by MAGIC for a beam current of 4 kA and a cathode voltage of 350 kV.

IV. Conclusions

Initial experiments show the radiated microwave power to be rather low; however, MAGIC predicts this low power level for the parameter space in which these experiments have been conducted. It should also be pointed out that the UNM SINUS-6 achieves considerably higher powers (~ 600 MW) [2] due to the fact that a more advanced slow wave structure has been installed in it. Once the theory behind the operation of this slow wave structure is better understood a structure of this design will then be placed on the Pulserad 110A. However, the immediate next steps in this investigation will involve varying the parameter space in MAGIC in order to determine a more favorable operating regime in which higher powers can be produced. Diagnostics will also be improved to better determine the radiated power and mode pattern. Work on plasma-filled BWO experiments will then begin, and the necessary diagnostics for these experiments will be developed and incorporated into the Pulserad 110A.

V. Acknowledgments

The authors wish to thank M. Anderson, J. Bradley, T. Cavasos, J. Crawford, L. Moreland, and R. Terry for their technical advice and assistance in assembling the experimental apparatus. The authors also with to acknowledge the work of N. Keator with much of the early MAGIC simulations.

References

[1] D. B. Cummings, "Conversion of a Marx Generator to a Type-A Pulse Forming Network," IEEE Conference Record of the Twelfth Modulator Symposium, IEEE Cat. No. 76CH1045-4ED, 1976, pp. 142-6.

[2] L. Moreland, et al., this conference.

[3] B. Goplen, R. E. Clark, J. McDonald, and W. M. Bollen, Users' Manual for MAGIC/Version-Oct. 1991, MRC/WDC-R-246, (Mission Research Corp., Washington, D.C., 1991).

[4] T. Spencer (private communication, 1992).

To Appear in Proceedings of the 9th IEEE International Pulsed Power Conference

INITIAL STUDIES OF FERROELECTRIC CATHODES

T. Cavazos, D. Shiffler, B. Wroblewski, C. Fleddermann,
J. Gahl, and E. Schamiloglu
Electrical and Computer Engineering Department
University of New Mexico
Albuquerque, NM 87131

Abstract--A basic limitation of all electron beam driven radiation producing devices is the need for more input power. For high power microwave devices and free electron lasers, this requirement may be stated as the need for greater electron beam current with higher brightness beams. Our research investigates ferroelectrics as a source of electrons for high current cathodes. Ferroelectric cathodes operate by inducing a phase transition in a sample of ferroelectric material, leaving copious amounts of electron space charge on the surface which can be easily liberated.[1] We have built a prototype electron gun in a triode configuration. The gun is energized using a transmission line pulser. The grid of the triode induces the phase transition. A second voltage is applied across the anode-cathode gap to accelerate the electrons. In this paper, we present results of polarization measurements under AC signals, as well as results of operating the triode as an electron gun. Finally, a design is presented for a beam transport system using standard accelerator technology to determine the beam emittance and brightness. Since ferroelectric cathodes can in principle operate at relatively low temperatures, the limiting emittance set by the cathode temperature should be very low.*

1-Introduction

Electron emission for vacuum electronics has been limited to thermionic sources (i.e. oxide coated or barium dispenser cathodes), explosive field emission cathodes (carbon felt materials) and exotic photocathodes. A novel cathode material has been introduced consisting of ferroelectric materials. By inducing a phase transition in a pre-poled ferroelectric, abundant electron emission can be observed. Emitted charge densities of up to 1 μC/cm2 [2] as well as current densities up to 70 A/cm2 have been documented.[3] These results demonstrate diode currents exceeding the space charge limit for typical vacuum diodes.

A research program is in progress at the University of New Mexico (UNM) to investigate ferroelectric cathodes as a novel emitter for high power microwave (HPM) sources. Such sources require high brightness, low emittance electron beams. Ferroelectric cathodes offer two key advantages over state-of-the-art thermionic emitters: (1) higher current densities and (2) lower operating temperatures. Since the ferroelectric is not operated as an explosive emitter, it is not susceptible to gap closure due to plasma formation. The material has demonstrated repetitive operation and can be used in any environment (rough to hard vacuum, and plasma filled devices).[4]

A key aspect of this research program is to investigate thin film ferroelectric cathodes. These films are fabricated in the UNM Center for High Technology Materials (CHTM). The materials can vary in thickness from 0.1 μm to 10 μm and can be produced in a variety of compounds and mixtures. Thin films have several advantages over bulk material: the ferroelectric can be switched at lower voltages since the material is thinner, the films may be grown or sputtered onto a wide variety of cathode geometries, and lastly, it may be possible to reduce the resultant electron beam divergence after emission.[5]

This paper summarizes the effort to date beginning with a brief discussion of the theory of ferroelectric emission in sec. 2. Section 3 describes the method of measuring the polarization (P-E) characteristics of the material. A discussion of the fabrication of the thin films is given in sec. 4 and a description of the triode experiments is given in sec. 5. The design and simulation of a low emittance gun is presented in sec. 6 followed by concluding remarks.

2-Theory of Ferroelectronics

Ferroelectric materials are polar dielectrics that undergo a change of spontaneous polarization under the influence of an applied electric field. Like ferromagnetic materials, ferroelectrics have domains, exhibit hysteresis loops, and show Curie-Weiss behavior near the phase transition temperatures.[6] The displacement in a polar material is expressed as:

$$\mathbf{D} = \varepsilon_o \mathbf{E} + \mathbf{P}, \tag{1}$$

where the polarization may be expanded as:

$$\mathbf{P} = \varepsilon_o \chi_e \mathbf{E} + \mathbf{P}_s + \mathbf{P}_d \,. \tag{2}$$

The first term is the polarizability of the material, the second term $\mathbf{P}_s$ describes the polarization due to the spontaneous alignment of the domains, and the last term is the polarization due to defects in the material [4]. For a given remanent polarization in the material, there will be a bound surface charge density which is expressed as:

$$q_{sb} = |\mathbf{P}|_{surface} \quad [\mathrm{C/m^2}] \,. \tag{3}$$

Under normal conditions, the bound surface charge is screened by free charges. If the material undergoes a rapid change in polarization, then a large uncompensated charge will be generated at the surface. The electric field is high enough (100-10,000 kV/cm) to extract carriers bound in the surface of the material. If conditions are arranged such that these carriers are negative, then the electrons will be accelerated into the diode gap.

This research is funded by AFOSR Grant #F49620-92-0157DEF.

The various methods of inducing a rapid change in the polarization include [4]:

(1) heating or cooling across a phase transition boundary from or to the ferroelectric (FE) state,
(2) transitions between the FE phase and the antiferroelectric (AFE) or paraelectric (PE) phases by applying pulsed stress,
(3) transitions between the AFE or PE phases and the FE phase by applying a pulsed electric field,
(4) partial reversal of P_s inside the ferroelectric phase by applying high voltage pulses, and
(5) illumination by laser light (photo assisted domain switching).

It is most advantageous to apply method (4) for [illegible]tition rate applications. This techniqu[illegible] initially selected for this research progr[illegible] A second option is to heat the material close to the phase transition, then apply a pulsed electric field to switch the material into the PE or AFE phase. With this combination of methods (1) and (3) no cooling of the material between pulses is necessary so that it is consistent with rep-rate operation. A further enhancement of emission can possibly be obtained by adding laser light illumination.

3-Polarization Curves

The hysteresis of a ferroelectric material is determined by plotting the polarization of the material as a function of the applied electric field. One method of performing this method is the Sawyer-Tower loop circuit (Fig. 1).[6] Capacitor C_t must be linear and should have a capacity much higher than the material under test. The vertical and horizontal voltages are written as:

$$V_x = Ed \text{ and}$$

$$V_y = \frac{1}{C_t}\int_0^t i(t)\,dt, \qquad (4)$$

where d is the thickness of the material. Assuming that the loop current is a uniform displacement current, the vertical voltage may be rewritten as:

$$V_y = \frac{1}{C_t}\int_0^t \frac{dD}{dt} A\,dt = \frac{D\,A}{C_t}, \qquad (5)$$

where A is the conduction area. Substituting Eq. (1) for the displacement gives

$$V_y = \frac{A}{C_t}(\varepsilon_0 E + P). \qquad (6)$$

Finally, substituting V_x/d for E and solving for P gives

$$P = V_y \frac{C_t}{A} - V_x \frac{\varepsilon_0}{d}. \qquad (7)$$

As long as C_t is large, the second term in Eq. (7) can be ignored and the vertical and horizontal voltages can be related to the polarization and electric field using

$$P = V_y \frac{C_t}{A} \text{ and } E = \frac{V_x}{d}. \qquad (8)$$

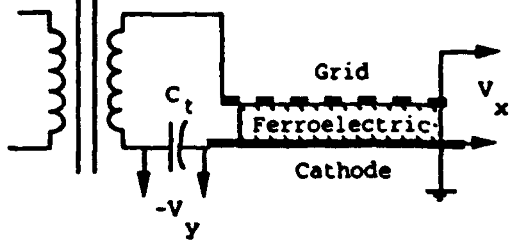

Fig. 1. Sawyer-Tower circuit for displaying P-E hysteresis curves.

The hysteresis curves are obtained with the materials mounted in the triode experiment. This step is to insure that there is good electrical contact with the material being tested. From the hysteresis curves, the remanent polarization P_r is determined from the vertical intercept, and the coercive field E_c is determined from the horizontal intercept. Hysteresis curves will be collected at temperatures up to the Curie temperature. Tests on a 0.25 mm PLZT wafer yielded the P-E curve shown in Fig. 2. This result most likely indicates a minor hysteresis loop. Attempts to increase the coercive field and drive the material into hard saturation resulted in electrical breakdown.

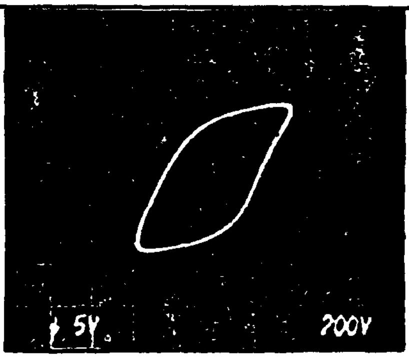

Fig. 2. P-E curve on a gridded PLZT wafer at room temperature. The vertical axis is approximately 1.5 μC/cm2 and the horizontal axis is 7.9 kV/cm.

4-Manufacturing Thin Films

The ferroelectric films are produced with an ion beam sputtering method (Fig. 3). The beam source is a Kaufman Ion Gun which provides independent control of beam energy and current. The ion gun is capable of

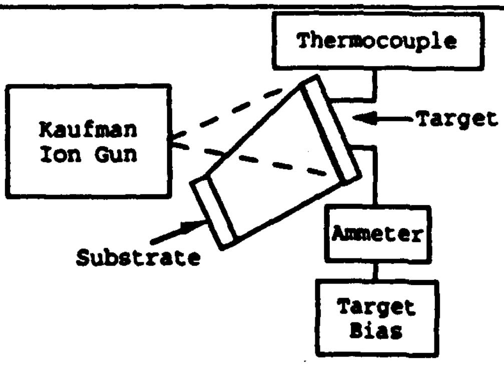

Fig. 3. Deposition system for ferroelectric thin films.

sputtering with an inert ion (Ar) beam or a reactive ion (O_2) beam. The sputtering target is a single composite (28/0/100) PLZT. The films are deposited onto a flat stainless steel substrate which has been coated with platinum. After deposition, the films are annealed in an oxygen furnace for half an hour at 650°C.

The CHTM laboratory also deposits gold electrodes onto the ferroelectric samples. The metallization is deposited using electron beam evaporation. The grid is patterned with standard photolithography/wet etch techniques. The electrode pattern is circular with 200 µm apertures and a 200 µm separation.

5-Triode Experiments

The purpose of the triode experiments is to determine the emission current density and charge limit of several different ferroelectric compounds. These results will determine the emittance of the cathode. A key aspect of this part of the research is to compare the performance of the thin film ferroelectric materials to the bulk materials. A parallel plane triode tube (Fig. 4) has been constructed for this task. The triode is a demountable vacuum tube assembled with 7 cm stainless steel flanges. An ion pump is used to evacuate the tube to 10^{-9} Torr. The grid flange is isolated from the cathode with a ceramic adapter and the anode is separated with a 25 cm glass tube. A tungsten filament heater is suspended inside a 1.9 cm stainless steel tube which is connected to cathode potential. The material under test is attached to a cap on top of the heater tube. Grid connections are made from the top of the sample to four stainless steel posts which are connected to the grid flange.

The experiment is operated as a grid modulated hard tube pulser. The anode potential can be varied from 10-30 kV and the grid is energized with a transmission line pulser. The ferroelectric material is pre-poled with the polarization vector pointing into the triode. Pre-poling is accomplished by heating the material above the Curie temperature and cooling down through the transition with a DC field across the material.

Electrical contacts to the bulk samples have been problematic. Connections are sensitive to mechanical stress due to the brittle nature of 0.25 mm ceramic wafers. The gold metallization adhered poorly to the ceramic. The grid pulled away from the sample when wires were bonded to the metallization. A conductive epoxy was used to glue foil contacts to the grid. However, the adhesive was too fragile for the mechanical stresses during the triode assembly. Planned improvements include roughening the surface of the ceramic to increase the surface tension with the gold metallization, and annealing the metallization at 200 °C after deposition. The mechanical mounting of the wafers has been redesigned to minimize the stress on the ceramic.

Initial tests on thin films were inconclusive. The grid contacts were shorted to the cathode in several cases. This problem could be caused by: 1) the film becoming scratched during assembly or 2) breakdown of the film due to static discharge during handling.

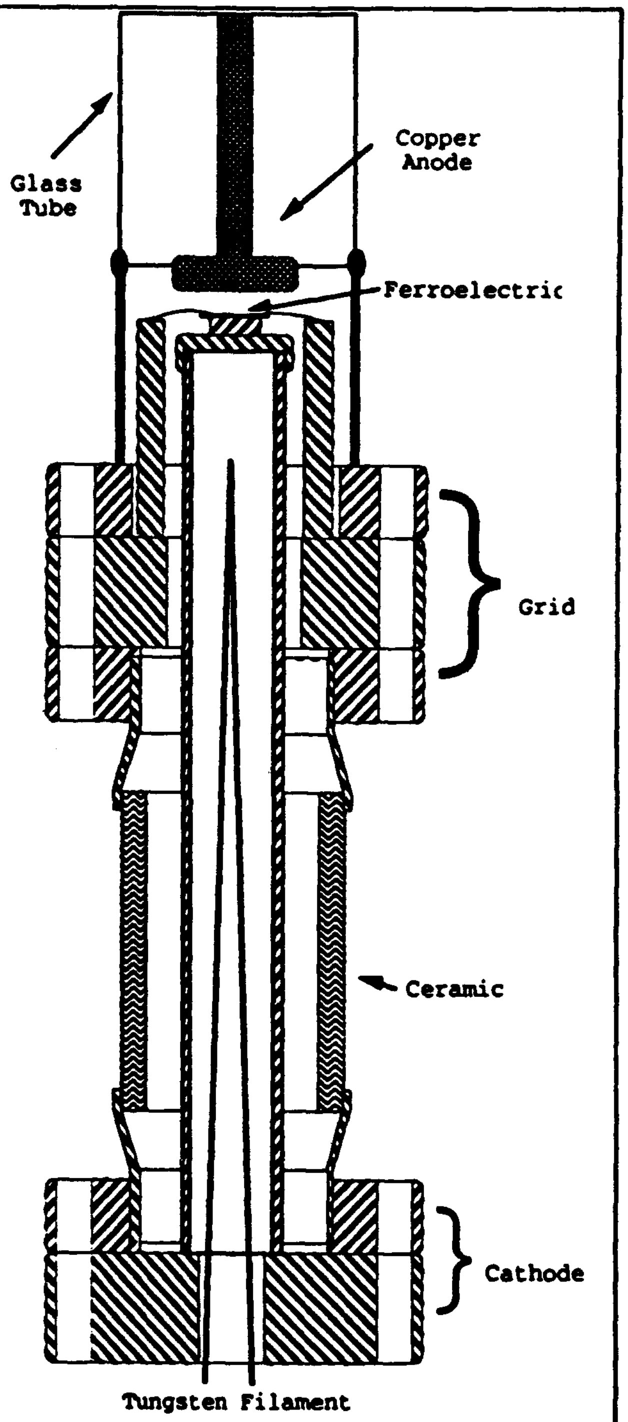

Fig. 4. Cut-away view of the ferroelectric triode. Vacuum flanges are 7 cm in diameter.

6-Ferroelectric Gun Design

The electron gun design is based on a Pierce gun configuration for low emittance operation. The design was analyzed using EGUN and the gun parameters for a 10 kV anode voltage are given in Table 1. A schematic of the ferroelectric gun is given in Fig. 5. The grid will be connected to the focusing electrode which must be held at ground potential. The ferroelectric will be energized with a negative cathode pulse.

Table 1. Electrical Parameters of the Ferroelectric Pierce Gun

Current Density	35 A/cm2
Current	25.2 A
Perveance	25.2 μPerv
Emittance	9.81 πmm-mrad

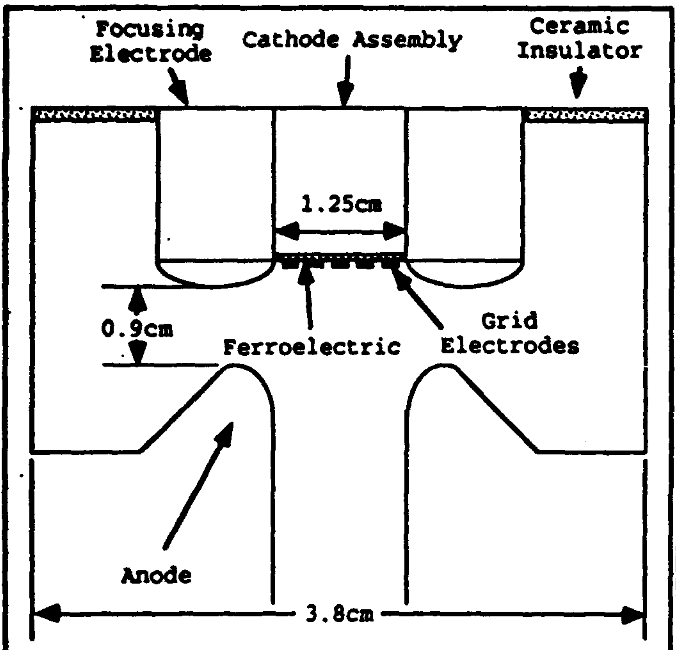

Fig. 5. Schematic of the ferroelectric Pierce gun.

The beam line will include diagnostics to determine beam emittance and energy spread for the ferroelectric cathode. The magnetic transport system consists of a quadrupole triplet and a spectrometer magnet. Phosphorus screens will be used to determine the beam spot, and hence emittance. The spectrometer magnet with a profilometer will determine the center energy and energy spread of the beam. A schematic of the beam line is given in Fig 6. The quadrupoles have a 4.06 cm effective length, 13 cm aperture, and field strength at the pole piece of 720G for a current of 1 A.

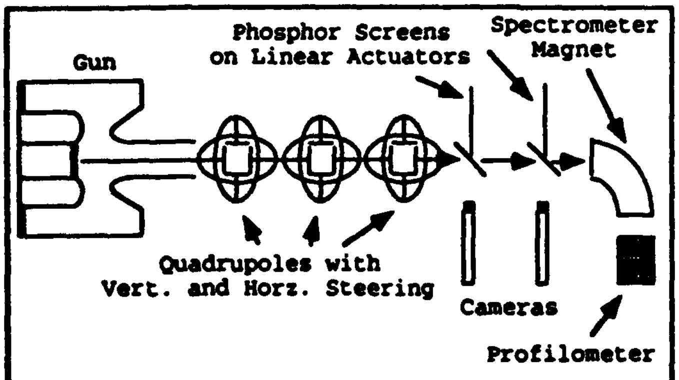

Fig. 6. Beam diagnostics for the ferroelectric gun.

7-Summary

A vacuum triode experiment has been assembled to study the emission from thin film and bulk ferroelectric materials. Significant problems have been encountered with mounting and connecting the bulk material to the triode. Redesign of the triode will include a stress-free holder for the ceramic and adhesion of the metallization to the samples will be improved. Fabrication of thin films has been performed, but the electrical characterization of this material is inconclusive at this time. The design of a low emittance Pierce gun using the ferroelectric cathode is complete as well as a design for a diagnostic system to determine beam quality. This work is expected to lead to improved performance of long pulse backward wave oscillators.

Acknowledgments

The authors wish to extend their gratitude to R. L. Terry and M. S. Anderson for help with the machining, assembly and maintenance of the experiment and to Bill Wilbanks for help in CHTM. The PLZT samples were supplied by Bruce Tuttle of Sandia National Laboratories and Jay Saxton of Motorola (Ceramic Products Division).

References

[1] H. Gundel, J. Handerek and H. Reige, "Time-dependent electron emission from ferroelectrics by external pulsed electric fields," *J. Appl. Phys.* **69**, (2), pp. 975-982, (1991).

[2] H. Gundel, H. Reige and E. J. N. Wilson, "Copious Electron Emission From PLZT Ceramics with a High Zirconium Concentration", *Ferroelectrics*, **100**, pp. 1-16 (1989).

[3] J. D. Ivers, L. Schachter, J. A. Nation, G. S. Kerslick and R. Advani, "Electron-beam diodes using ferroelectric cathodes," *J. Appl. Phys.* **73**, (6), pp.2667-2671, (1993).

[4] H. Gundel, "Electron Emission by Nanosecond Switching in PLZT," Integrated Ferroelectrics, **3**, pp. 207-220 (1992).

[5] H. Gundel (private communication, 1993)

[6] J. C. Burfoot and G. W. Taylor, *Polar Dielectrics and Their Applications*, Los Angles: University of California Press, 1979.

Appendix B. Journal Manuscripts Submitted and Accepted for Publication

Suppression of Vacuum Breakdown Using Thin Film Coatings

C. S. Mayberry, B. Wroblewski, E. Schamiloglu, and C. B. Fleddermann

Department of Electrical and Computer Engineering
University of New Mexico
Albuquerque, New Mexico 87131

ABSTRACT

Thin film metal and metal oxide coatings ion sputter-deposited onto the cathode electrode of a parallel-plate high voltage gap were found to suppress electron emission in high vacuum. Electric fields as high as 60 kV/mm have been sustained across a 1 mm gap for pulse durations of 10 μs. Lesser electric fields were sustained for pulse durations exceeding 10 ms. The behavior of 500 nm thick coatings was independent of the type of coating used, whereas the breakdown voltage for thinner coatings depended upon the material and the deposition conditions. The breakdown properties of various coatings, as well as a discussion of the suppression of electron emission is presented.

Submitted to J. Appl. Phys.
(5/93)

PACS: 84.70, 77.55, 52.75.P

I. Introduction

The ability to sustain large electric fields across metal electrodes in vacuum is an important consideration in pulsed power applications.[1] Previous researchers have attempted to improve the breakdown characteristics of metal electrodes by coating them with various dielectrics, including epoxy, oil, and polymers.[1-6] Although these coatings led to improved performance, little work was done to understand the mechanisms that increase the threshold voltages for initiating breakdown.

This paper describes the results of an experimental investigation to increase the threshold breakdown voltages and sustained pulse durations across planar stainless steel electrodes in high vacuum ($P_{base} < 4 \times 10^{-8}$ Torr). A solid anode electrode and thin-film coated 80% transparent mesh cathode were used. (Films were deposited on the cathode screen using ion-beam sputter deposition.) The choice of electrode material, as well as the actual configuration, were selected as part of a study of a planar liquid metal ion source.[7] In addition, the choice of coating materials was motivated by initial studies of coatings for use in high power microwave sources.[8]

This paper is organized as follows: Section II presents a discussion of relevant vacuum breakdown theories. Section III describes the experimental apparatus and presents measurements of the breakdown characteristics of various coatings. The conclusions from this work are presented in Sec. IV.

II. Breakdown Theories

As the voltage across parallel-plate electrodes in vacuum is increased, small currents are emitted from local sites on the electrodes. These small currents, called prebreakdown currents, generally arise from one or two micron tall protrusions on the surface of the cathode. At the tips of the protrusions, the electric field becomes enhanced to the point where field emission can occur, typically at about an electric field $E \approx 3 \times 10^3$ kV/mm. These currents are typically in the picoAmpere range and obey an equation found from a quantum mechanical treatment of a clean metal-vacuum boundary and is shown here in its most useful form:[2]

$$\log \frac{I}{V^2} = \log \left[\frac{1.54 \times 10^{-6} A_e \beta^2 10^{4.52\phi^{-1/2}}}{\phi d^2} \right] - \frac{2.84 \times 10^9 d \phi^{1.5}}{\beta V}, \qquad (1)$$

where ϕ is the work function of the material, A_e is the effective emitting area, d is the anode-cathode (A-K) gap distance, V is the applied voltage, and β is the field enhancement factor. This equation, known as the Fowler-Nordheim equation, yields β and A_e from the slope and intercept of a graph of $\log\frac{1}{V^2}$ versus $\frac{1}{V}$. As the applied voltage on a microprotrusion increases, the current will increase for a given set of parameters until it is space-charge-limited. At that point the I-V characteristic departs from the Fowler-Nordheim equation and assumes a Child-Langmuir dependence with $I \propto \frac{V^{3/2}}{d^2}$. The microprotrusion cannot sustain very large current densities and eventually, through Joule heating, vaporizes, forming a microplasma which is considered the seed of an eventual breakdown.[2] This type of breakdown applies to short gaps where d<0.5 mm.

The dependence of Eq. (1) on the gap spacing d is not as straightforward as it appears. The macroscopic electric field needed to maintain a prebreakdown current has been shown to decrease with increasing d. This is termed the "Total Voltage Effect" and is attributed to two theories.[2] One theory suggests that higher voltages result in higher sputtering rates of adsorbed oxygen, which in turn give higher emission current (an oxygen free surface has a lower work function). Another theory suggests that there is increased current resulting from a rise in surface temperature on the cathode following its bombardment by increasingly energetic positive ions. Either of these theories can lead to breakdown by filling the gap with sufficient material so that an avalanche can occur. These mechanisms are thought to occur mainly for large gaps where d>2 mm. The key to suppressing breakdown is to minimize the seed material that is introduced into the A-K gap, and this is ultimately done by suppressing electron emission from the cathode when the anode is pulsed positively.

III. Experimental Apparatus and Measurements

The experiment, shown in Fig. 1, consists of an A-K gap in a stainless steel vacuum chamber at a base pressure of 4×10^{-8} Torr. A cryogenic pump was used to achieve the base pressure. The anode is made of polished stainless steel, 2.54 cm square. The broad area cathode is an 80% transparent stainless steel mesh. The cathode is adjustable over the anode to a minimum gap spacing of 1.00 ± 0.12 mm. A voltage pulse is applied to the anode from a 0.733 μF capacitor through a spark gap switch. The pulse risetime is less than 1 μs. The voltage pulse was terminated with a crowbar spark gap switch across the capacitor. The typical A-K gap used was 1 mm and voltages from 20 - 65 kV were applied. Additional information on the hardware can be found in Ref. 9.

The breakdown theories described in Sec. II were the guiding principles upon which we operated the experiment. The breakdown theories suggest that anything that can be done to blunt microprotrusions and to remove loose particles adhering to electrode surfaces should improve the breakdown characteristics of the gap. Towards that end we first polished the anode with a high speed polishing wheel and jewelers rouge. (Of course this could not be applied to the delicate cathode mesh.) Both of the electrodes were subjected to washing with isopropyl alcohol, methanol, and finally with acetone. After the electrodes were installed, the gap was sprayed with 40# synthetic air to remove any dust that may have settled on the surfaces. The intent of these procedures was to remove as many microparticles from the electrodes as possible, and to minimize the formation of monolayers of oxygen and water. The chamber was pumped down to a final pressure of 4×10^{-8} Torr before any voltages were applied. These procedures alone resulted in breakdown occurring at 30 kV/mm within 50-100 μs.

There are a number of *in situ* conditioning processes that can be applied to reduce the emitted current from microstructures.[2,6] The gap can be subjected to successively higher DC voltages, allowing the prebreakdown currents to decay over a span of approximately 30 minutes. Another employs glow discharge cleaning and takes advantage of the sputtering action of low-energy ions to knock off layers of contaminants. This was performed on our experiment with no noticeable improvements, as our vacuum was very good to begin with and this method is generally useful for removing contaminants which keep the chamber pressures high.

Another conditioning method was used on our experiment to recover lost performance after a breakdown. Figure 2 (a) shows a typical wire from the cathode mesh magnified 2750 times using an environmental scanning electron microscope (ESEM). The wire has channels running along its axis due to its manufacturing processes. (Note the microparticles which were not removed by cleaning.) Figure 2 (b) shows a mesh after a breakdown event which possesses many fine structures where field enhancement can occur. By reducing the applied voltage, increasing the pulse duration, and repeatedly pulsing the gap until breakdown no longer occurs, we were able to regain some of the performance of the gap prior to breakdown. This procedure is thought to blunt the microprotrusions created by the breakdown event, thus lowering their β values so that emission levels would be reduced.

The maximum electric field and pulse duration achieved without breakdown using the above procedures was 30 kV/mm for 100 μs. A great advance over these results was made by sputter-depositing thin film coatings onto the cathode mesh. Figure 3 shows a comparison of the breakdown voltages for different coatings, all grown to a thickness of 500 nm. Films were deposited using ion-beam sputtering with a 2.5 cm diameter Kaufman gun. Typically, the ion gun was run with a beam voltage of 750 V and a beam current of 30 mA. Metal films were deposited using an argon ion beam, and oxides were deposited using Ar/O_2 mixtures. Sputter targets were either metals or stoichiometric oxides, depending on the film to be deposited. The coatings in Fig. 3 are compared with a bare stainless mesh on the left. It is clear from the figure that coating the cathode increases the threshold breakdown voltage for all materials except TiN, and that TiO_2 and SnO_2 performed the best. All experiments described here were performed using TiO_2 coatings.

One hypothesis that can be used to explain the increase in the breakdown electric field with the thin film coatings is that these coatings buried, to some extent, the microprotrusions left by the manufacturing process. The screens, as shown in Figs. 4 (a) and (b) viewed on a micron scale using an ESEM, reveal a smoother surface for the coated screen. The results obtained were repeatable and suggest that a sputter-deposited surface of approximately 500 nm thickness is smoother than the bare surface. This is also revealed in Fig. 5 which shows the breakdown electric field for several sputter-deposited metal films, including a sputter-deposited stainless steel film, compared to bare stainless steel. All of these coatings achieved a peak electric field of about 50 kV/mm. We have found that there are a large variety of coatings which, when grown to at least 500 nm, yield a large increase in the breakdown electric field by creating a smoother surface with a smaller average β, thus reducing electron emission from the cathode.

Thinner films (200 nm) showed a variation of breakdown electric field with a change in the deposition condition. Specifically, we varied the oxygen content of the sputter gas mixture used during film growth, with all other ion beam parameters held constant. Breakdown field as a function of oxygen content of the beam is shown in Fig. 6 for TiO_2 films. (Rutherford backscattering measurements on these films confirmed that all were stoichiometric TiO_2.) This plot indicates that the breakdown electric field varies markedly with oxygen content while a plot for a TiO_2 film at a thickness of 500 nm, shown in Fig. 7, is independent of the deposition conditions. It is widely known that the index of refraction, grain size, and packing density of oxide films vary with the oxygen partial pressure during deposition, and that the index of refraction is indicative of changes in the latter two properties.[10,11] We have verified the relationship of the index of refraction as a function of oxygen content of the background gas as shown in Fig.8, and this agrees with the experimental findings in Ref. 10. Therefore, it is apparent that the breakdown electric field for thin films (200 nm) is more sensitive to the film properties, while for 500 nm thick films, merely burying surface microprotrusions becomes the dominant mechanism in achieving the larger breakdown electric fields.

The breakdown behavior of Ti/TiO_2 layered structures deposited on the cathode screen was also investigated. Two of this type of film were studied: one was a 100 nm thick pure titanium layer deposited on the screen, followed by a 100 nm thick TiO_2 layer (grown using 50% oxygen in the ion beam) for a total layer thickness of of 200 nm; the other was a similar structure with 300 nm of Ti with 200 nm of TiO_2 for a total thickness of 500 nm. For the 300/200 film, the breakdown field was 52 kV/mm, which is comparable to the fields measured for 500 nm Ti and TiO_2 films. In this case the presence of the dielectric is insignificant as is expected for the thicker films, and the breakdown field increase is due to the burying of imperfections. However, the 100/100 film had a breakdown field of 44 kV/mm. This is significantly higher than the breakdown field for a 200 nm thick pure Ti film (the 0% oxygen value in Fig. 6), showing that for thin films where the effect of covering up cathode imperfections is not as significant, the presence of even a thin dielectric layer can cause measurable improvement in the breakdown behavior of the cathode.

IV. Conclusions

The results of this study indicate that thin film coatings of metals or metal oxides can yield a factor of two increase in the breakdown characteristics of parallel-plate stainless steel electrodes in high vacuum. The study found that the breakdown electric field for 200 nm thick coatings was dependent on the grain size or packing density of the film, whereas the breakdown field for 500 nm thick coatings was independent of the material properties. To achieve the highest breakdown field, the oxygen content of the background gas should be 50% or higher for 200 nm thick films, or 500 nm thick films should be applied. It is important to note that these coatings are not robust. While some level of performance can be regained after a breakdown event, generally the coated cathode screen will have to be replaced if the application cannot tolerate a large variation in breakdown electric field.

Acknowledgements

The authors would like to thank Dr. V. I. Rakhovsky for useful discussions on the total voltage effect, and R. L. Terry for providing technical assistance with the experimental hardware. In addition, they would like to thank S. Droes for performing the Rutherford backscattering measurements. This research was supported by Sandia National Laboratories contract No. 69-5698, and partially supported by AFOSR grant F49620-92-J-0157P00001.

References

1. See, for example, articles in *Proceedings of the 15th International Symposium on Discharges and Electrical Insulation in Vacuum*, edited by D. Konig (IEEE, 92CH3191-2, Berlin, 1992).

2. R. V. Latham, *High Voltage Vacuum Insulation, The Physical Basis* (Academic Press, NY, 1981).

3. J. C. Anderson, J. Vac. Sci. Technol. **9**, 1 (1972).

4. E. W. Gray, J. Appl Phys. **58**, 132 (1985).

5. G. B. Frazier, Proceedings of the 2nd International Pulsed Power Conference (IEEE, New York, 1979), p. 127.

6. R. J. Noer, Appl. Phys. A **28**, 1 (1982).

7. C. S. Mayberry, E. Schamiloglu, and G. W. Donohoe, submitted to J. Appl. Phys.

8. D. Shiffler, T. Cavazos, L. Moreland, C. Fleddermann, J. Gahl, and E. Schamiloglu, Bull. Am. Phys. Soc. 37, 1540 (1992).

9. C. S. Mayberry, M. S. Thesis, University of New Mexico (1993).

10. H. K. Pulker, G. Paesold, and E. Ritter, and E. Ritter, Appl. Opt. **15**, 2986 (1976).

11. S. Schiller, G. Beister, W. Sieber, G. Schirmer, and E. Hacker, Thin Solid Films **83**, 239 (1981).

Fig. 1. Schematic of the experimental set-up (not drawn to scale).

Fig. 2. Comparison of stainless steel meshes coated with stainless steel before (a), and after (b) a breakdown event.

Fig. 3. Maximum breakdown electric fields for several types coatings sputter-deposited with a beam composed of 50% argon and 50% oxygen.

Fig. 4. Comparison of a bare stainless steel mesh (a) to one coated with 500 nm of sputter-deposited stainless steel (b).

Fig. 5 Maximum breakdown electric fields for several types of metal coatings sputter deposited with a beam composed of 100% argon.

Fig. 6. Plot of breakdown electric field as a function of the oxygen content of the background gas for a film thickness of 500 nm.

Fig. 7. Plot of breakdown electric field as a function of the oxygen content of the background gas for a film thickness of 200 nm.

Fig. 8. Plot of the index of refraction as a function of the oxygen content of background gas for TiO_2 films.

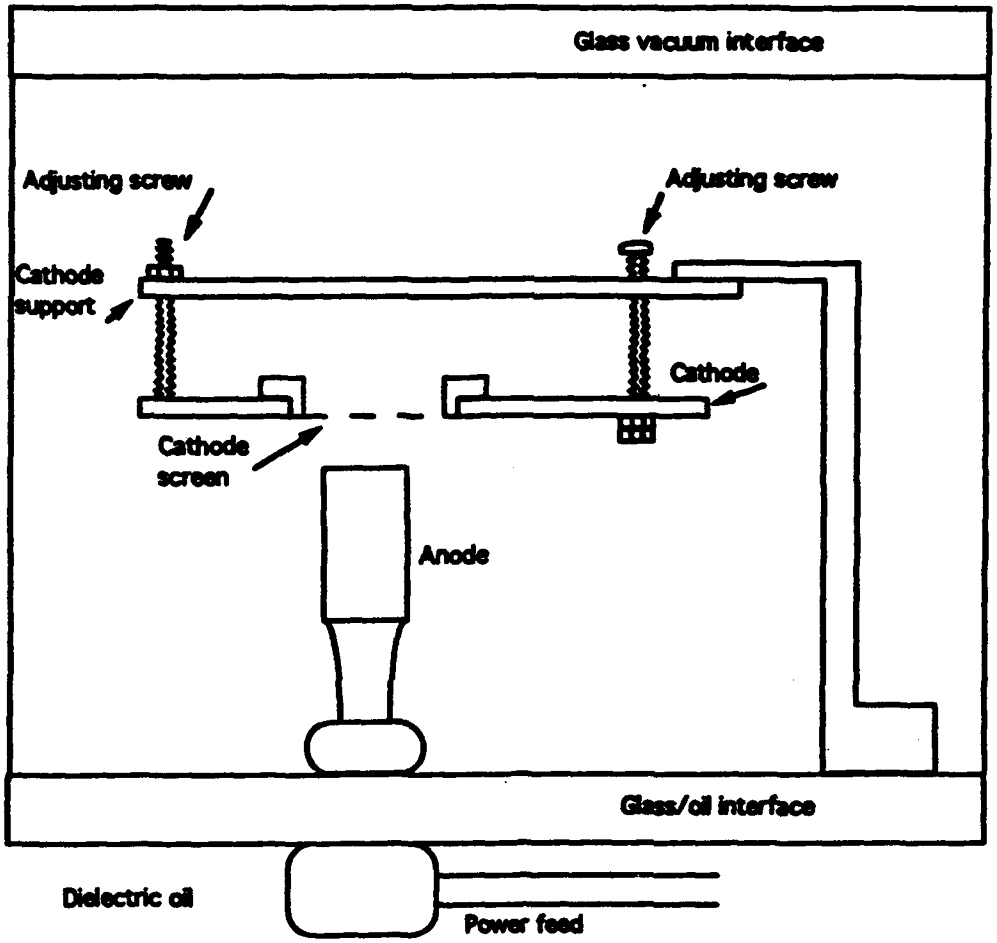
Glass vacuum interface
Adjusting screw
Adjusting screw
Cathode support
Cathode
Cathode screen
Anode
Glass/oil interface
Dielectric oil
Power feed

Fig. 1

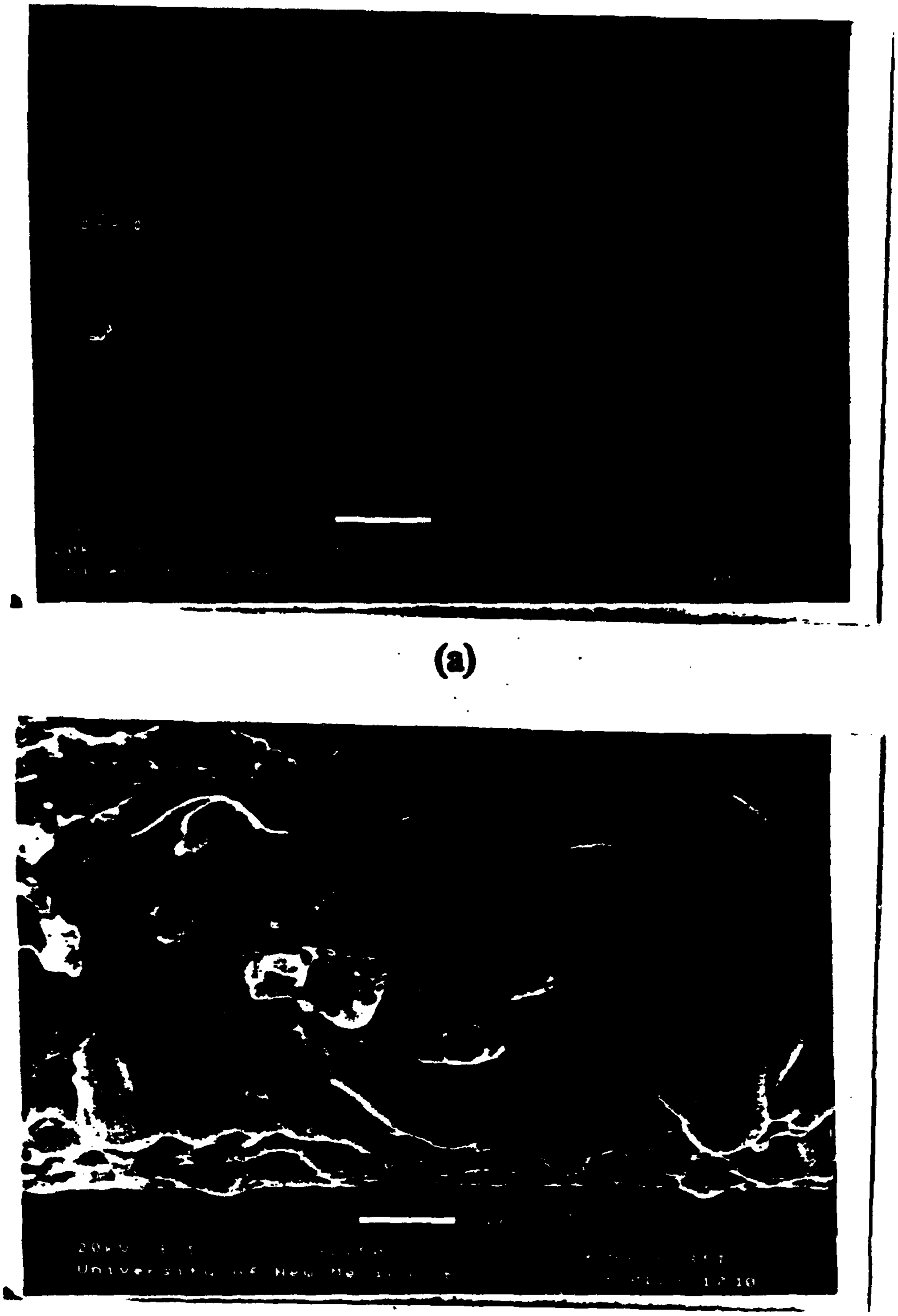

(a)

(b)

Fig. 2

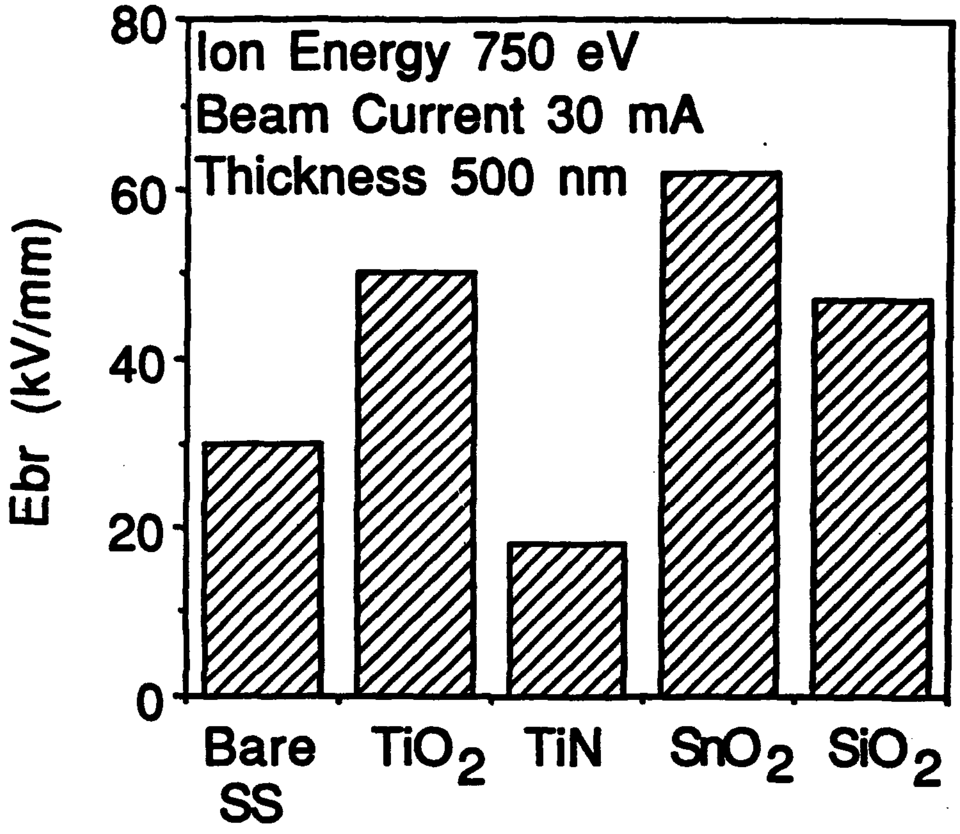
Ion Energy 750 eV
Beam Current 30 mA
Thickness 500 nm
Ebr (kV/mm)
80
60
40
20
0
Bare SS
TiO2
TiN
SnO2
SiO2

Fig. 3

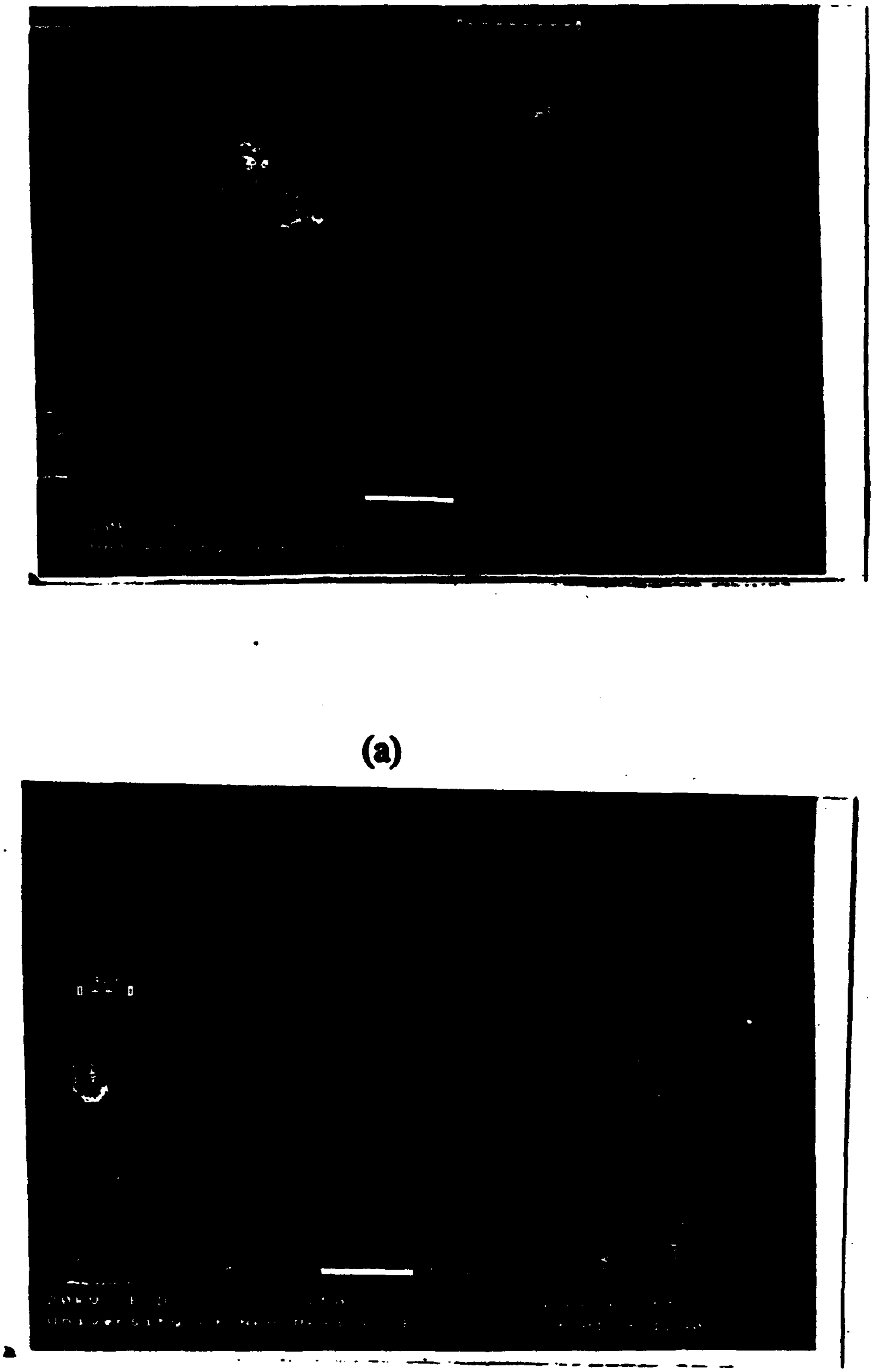

(a)

(b)

Fig. 4

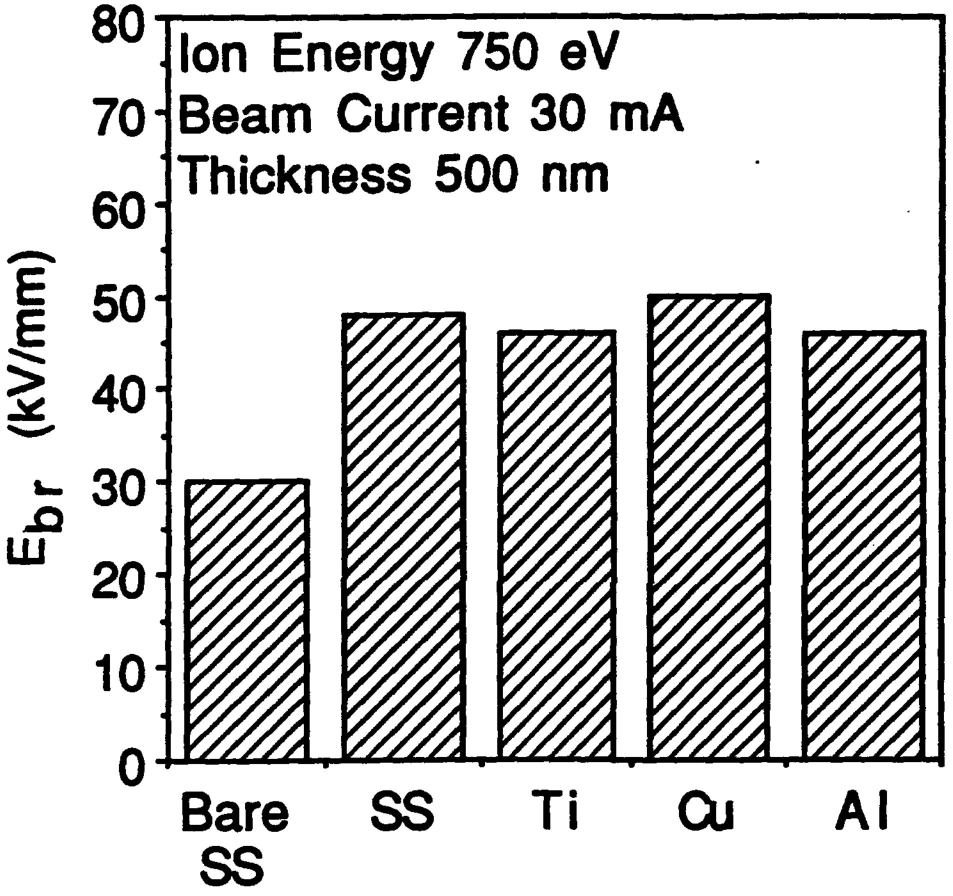

Ion Energy 750 eV
Beam Current 30 mA
Thickness 500 nm
E_{br} (kV/mm)
0
10
20
30
40
50
60
70
80
Bare SS
SS
Ti
Cu
Al

Fig. 5

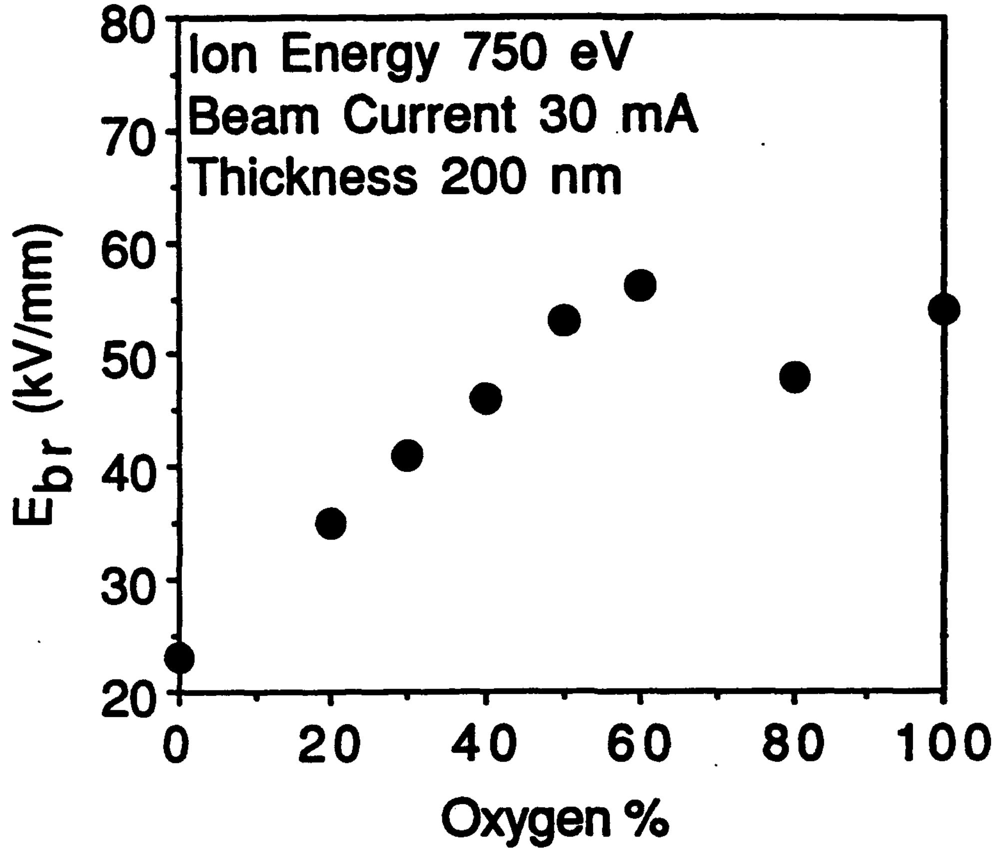

Ion Energy 750 eV
Beam Current 30 mA
Thickness 200 nm
E_{br} (kV/mm)
80
70
60
50
40
30
20
0
20
40
60
80
100
Oxygen %

Fig. 6

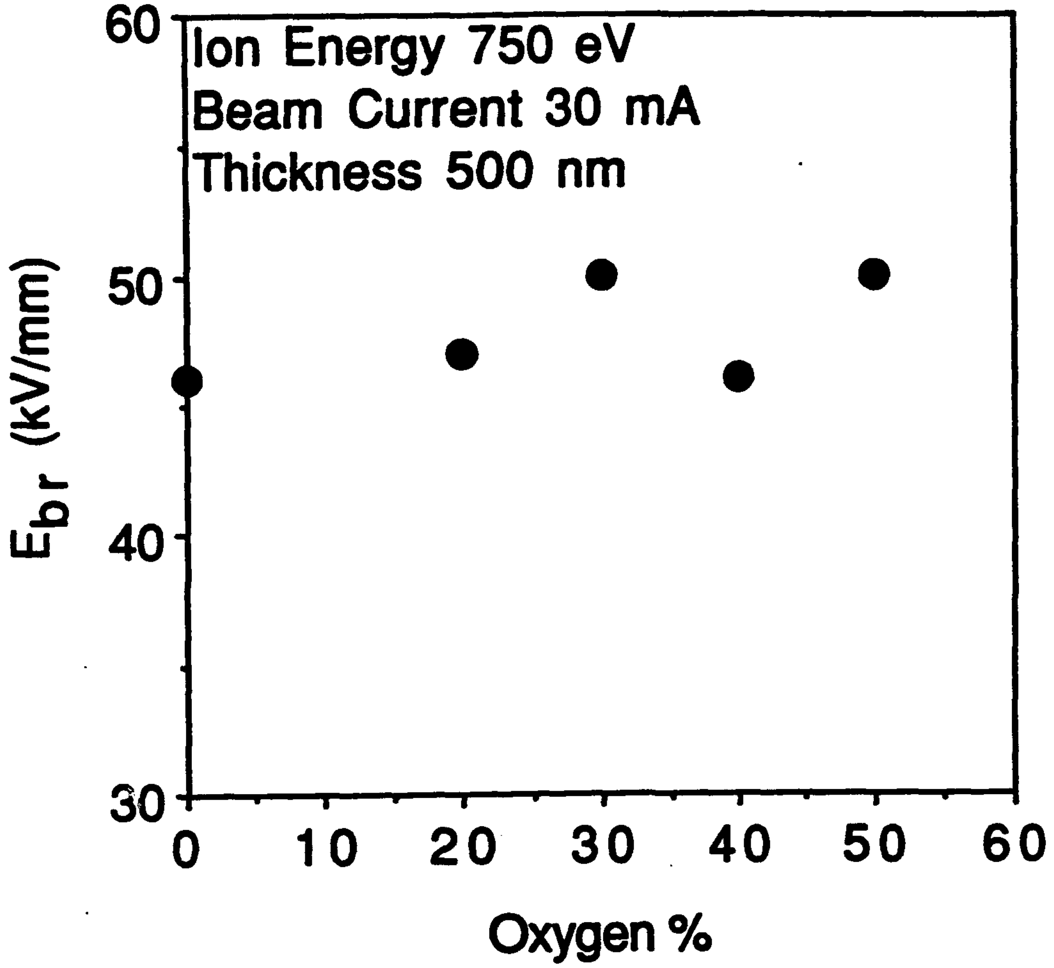
Ion Energy 750 eV
Beam Current 30 mA
Thickness 500 nm
60
50
40
30
E_{br} (kV/mm)
0
10
20
30
40
50
60
Oxygen %

Fig. 7

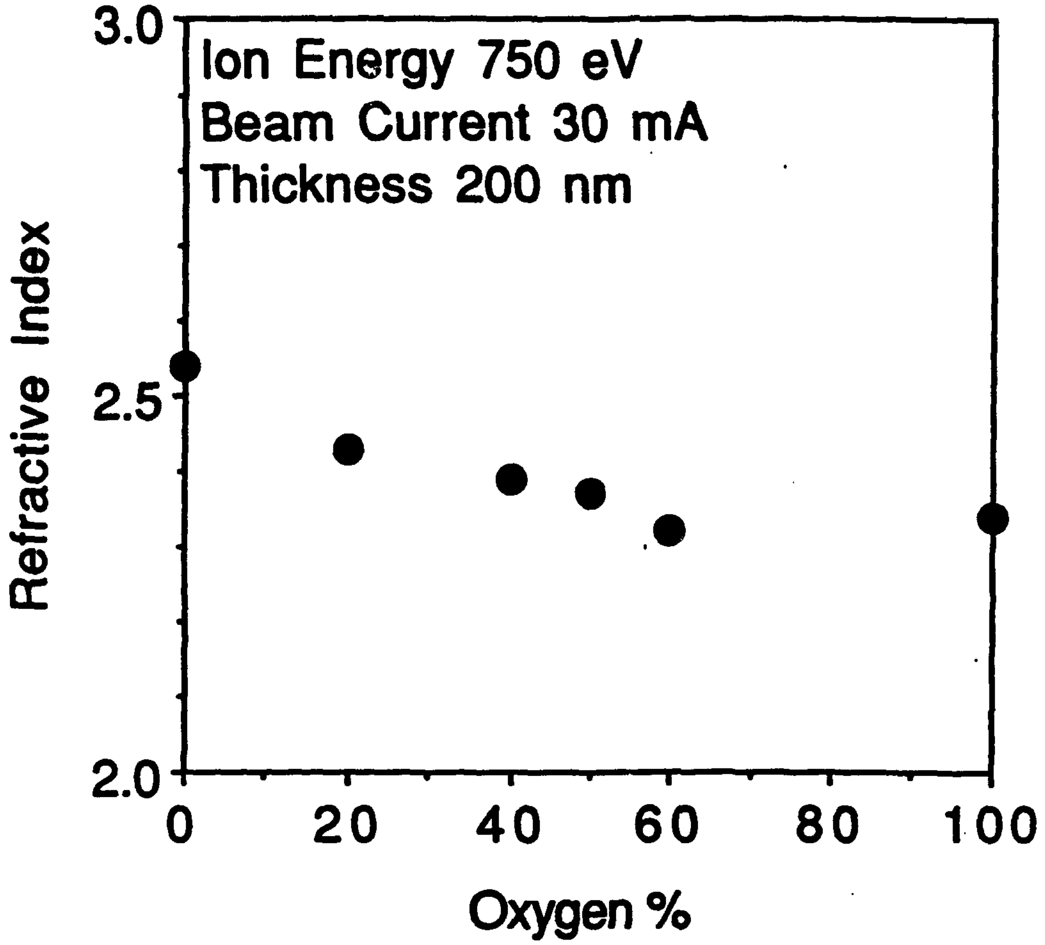
Ion Energy 750 eV
Beam Current 30 mA
Thickness 200 nm
Refractive Index
3.0
2.5
2.0
0
20
40
60
80
100
Oxygen %

Fig. 8

Efficiency Enhancement of High Power Vacuum BWOs Using Nonuniform Slow Wave Structures

L. D. Moreland, E. Schamiloglu, R.W. Lemke,* S.D. Korovin,** V.V. Rostov,** A.M. Roitman,** K.J. Hendricks,*** and T.A. Spencer***

Pulsed Power and Plasma Science Laboratory
Department of Electrical and Computer Engineering
University of New Mexico
Albuquerque, NM 87131

Abstract—The Sinus-6, a high power relativistic repetitively-pulsed electron beam accelerator, is used to drive various slow wave structures in a BWO configuration in vacuum. Peak output power exceeding 500 MW at 9.6 GHz was radiated in an 8 ns pulse. We describe experiments which study the relative efficiencies of microwave generation from a pair of nonuniform amplitude slow wave structures. A simple model analyzing the changes in electron energies and their relative phases along the length of a nonuniform amplitude BWO provides insight into the improved efficiency achieved using a two stage nonuniform tube. Experimental results are compared with 2.5 D particle-in-cell computer simulations. Initial results suggest that prebunching the electron beam in a nonoscillating shallow-ripple section of a nonuniform BWO results in increased microwave generation efficiency. Furthermore, simulations reveal that, in addition to the backward propagating transverse magnetic surface mode, backward and forward propagating volume modes with wavelengths twice that of the surface mode play an important role in high power microwave generation and radiation.

* Department 1241, Sandia National Laboratories, P.O. Box 5800, Albuquerque, NM 87185

** Institute of High Current Electronics, Siberian Branch, Russian Academy of Sciences, Tomsk, Russia

*** Phillips Laboratory, Advanced Weapons and Survivability Directorate, Air Force Materiel Command, Kirtland Air Force Base, NM 87117

Accepted for publication in
IEEE Trans. Plasma Sci.
with revisions

I. INTRODUCTION

There have been many experimental and theoretical studies of high power backward wave oscillators (BWOs) [1]. The majority of the work within the United States has used slow wave structures with uniform ripple amplitudes and periods. Analyses have shown that nonuniform BWOs can be designed to yield higher beam-to-microwave power conversion efficiency than uniform BWOs [2,3]. In a nonuniform BWO, the interaction between the electron beam and electromagnetic modes changes along the length of the tube due to variations in the coupling impedance or phase velocity. The coupling impedance between the slow space charge wave on the electron beam and the TM_{01} mode can be modified by varying the ripple amplitude, or by varying the magnetic field distribution within the tube. The phase velocity of the TM_{01} mode can be varied along the length of the tube by gradually changing the period of the ripples. The efficiencies for converting input beam power into RF radiation using uniform BWOs have been reported to be as large as 15%. Work from the former Soviet Union on nonuniform BWOs has shown experimental measurements of RF efficiencies exceeding 40%, and theoretical predictions indicate efficiencies may reach 75% [2,3].

The goal of this study is to define the physics of the nonuniform BWO, which may reveal methods of further improving the efficiency of microwave generation using the Sinus-6 accelerator. In particular, we seek to quantify the use of a nonoscillating shallow ripple section as a prebuncher to yield high efficiency operation. Experimental results are presented which contrast the operation of a nonuniform BWO both with and without such a prebuncher. A simple model analyzing the changes in electron energies and their relative phases along the length of a nonuniform amplitude BWO provides insight into the mechanism for improved efficiency using a prebuncher.

The complexity of the nonuniform BWO experiment precludes an exact theoretical analysis using analytical methods. Therefore, particle-in-cell (PIC) simulation is the most feasible approach to investigating the physics of the nonuniform BWO. To this end, we have performed simulation studies of the experimental configurations using the 2.5 D, relativistic, fully electromagnetic PIC code TWOQUICK [4]. This code is a derivative of MAGIC [5].

This paper describes results to-date from a systematic program to investigate RF efficiencies of nonuniform BWOs using the Sinus-6 repetitively-pulsed electron beam accelerator. The Sinus-6 was designed and constructed jointly by the Institute of High Current Electronics and the Institute of Electrophysics. The advantage of this accelerator is that it easily yields hundreds of BWO test shots in a single day, which facilitates careful comparison of experimental results with theoretical calculations and particle simulations. The remainder of this paper is organized as follows. Section II describes the experimental setup and is followed in Sec. III by a detailed discussion of the experimental measurements. Section IV contains a single particle model which yields an explanation for the increased efficiency of a nonuniform BWO using a prebuncher. A detailed discussion of the PIC code simulation results is covered in Sec. V, along with comparisons with the experimental results. Finally, conclusions from this study and plans for future work are outlined in Sec. VI.

II. EXPERIMENTAL SETUP

Figure 1 is a cut-away diagram of the Sinus-6. The Tesla transformer (1) steps up the voltage from 300 V to 700 kV. An open ferromagnetic core is used in the Tesla transformer, which provides a high coupling coefficient between the transformer windings. The pulse forming line is contained within the Tesla transformer permitting both increased efficiency and an overall compact system. The high voltage switch (2) is a nitrogen-filled spark gap, which is pressurized to 18 atmospheres. By adjusting the pressure, the spark gap voltage can be varied from 400 to 700 kV. The oil-filled adiabatic transmission line (3) matches the 22 Ω impedance of the pulse forming line to the ~ 100 Ω impedance of the vacuum diode. The magnetically insulated coaxial vacuum diode (4) uses an explosive-emission graphite cathode. The diameter of the annular electron beam is 2 cm with a beam thickness of 1 mm, confirmed using a witness plate damage diagnostic. A magnetic field of 2.6 T, used to confine the electron beam, is generated by a pulsed solenoid system. The pulsed system provides a magnetic pulse duration of 3 ms and requires 8 s to recharge. The Sinus-6 can generate electron beams at a pulse repetition rate of 200 Hz, but is presently operating at 0.1 Hz due to constraints imposed by the magnetic field system.

The electron beam pulse has a full width, half maximum (FWHM) temporal duration of about 12 ns. Figure 2 shows typical voltage and current waveforms. By adjusting the pressure in the spark gap, cathode voltages from 400 to 650 kV were tested with corresponding beam currents ranging from 3 to 5 kA.

Total peak radiated power measurements were made using both a resistive sensor and a crystal diode detector, as indicated in Fig. 3. Power density measurements were made 1.7 m downstream from a conical horn antenna, which has a maximum diameter of 15 cm. The total power was calculated by numerically integrating the radiation pattern that was experimentally mapped. A WR-90 section of waveguide was attached normal to the antenna to measure side lobe radiation. This setup was calibrated to yield total radiated power. The resistive power detector is based on a semiconductor's fast electrons' response to high power radiation. The fast electrons cause the bulk resistance of the semiconductor to change. The detector is biased by a 100 μs, 50 V pulse. An oscilloscope records the transient voltage response due to the change in bulk resistance caused by the microwave radiation.

Additional measurements were made using the setup shown on the right in Fig. 3. After cables, attenuators, and connectors were calibrated using a scalar network analyzer, peak power densities were measured using the crystal diode detector. The radiated frequency was measured by heterodyning the RF signal against a known oscillator frequency.

Two basic nonuniform tube configurations were used in this study. Long tube #1 is a two stage nonuniform amplitude BWO and is constructed from individual rings for each ripple period. Each ring has a width of 1.5 cm (corresponding to a ripple period of 1.5 cm) and a maximum radius of 1.65 cm. Four different rings were used, as summarized in Table 1.

Long tube #1 has two sections, a first section with shallow ripples followed by a second section with deeper ripples. A variation of this tube is short tube #1 where the shallow first section is removed.

The advantage of the Sinus-6 accelerator is that, for each different BWO structure, hundreds of test shots can be taken over a limited range of beam parameters. Within its first year of operation at the University of New Mexico, the Sinus-6 has accumulated over 10,000 single shots.

III. EXPERIMENTAL RESULTS

In this section we summarize experimental data contrasting the performance of long and short tubes #1. Figure 4 presents the radiation pattern from the Sinus-6 using long tube #1 and a conical horn antenna. The radiation pattern is compared with a calculated [6] TM_{01} radiation pattern with a total peak power of 500 MW. Agreement is excellent between the measured and calculated mode patterns.

Comparisons were made of total radiated power versus the beam current using a side lobe measurement with the resistive power detector. For long tube #1, Fig. 5 presents total radiated power as a function of beam current. (It should be noted that the cathode voltage was not held constant but was allowed to vary to access the range of beam currents.) The input power was calculated by multiplying the beam current and cathode voltage and this was used to calculate the RF radiation efficiency shown in Fig. 6. The data suggests that the start current for the tube is approximately 2 kA and that the efficiency of the tube saturates at about 4 kA In Fig. 7, the total radiated peak power is plotted as a function of peak input beam power.

Power density measurements were made using the setup shown above in Fig. 3 at the peak lobe 8° off axis. Measurements were made to investigate the two stage nonuniform BWO by testing each stage individually. Sections of cutoff pipe were added to the modified tubes to ensure that the overall length of the tubes remained constant. This was required to keep the A-K gap constant and to ensure proper matching with the tapered magnetic field at the end of the tube. When the AABBB section was tested alone with beam currents as large as 3.5 kA, no measurable power was detected to a noise level of -25 dB. In other words, this section alone does not oscillate. The relative power of long and short tubes #1 were compared. Additional minor modifications were made to long tube #1 where the number of C rings were replaced by A rings. The configurations and results of power and frequency measurements are summarized in Table 2. From the data summarized in Table 2, it is evident that the initial AABBB section enhances microwave generation efficiency. Insight into the mechanism for this enhancement can be gained from a phase analysis and PIC code simulations. These are discussed in Sec. IV and V, respectively.

IV. PHASE ANALYSIS OF NONUNIFORM BWOs

The interaction between an electron beam and radiated modes within a slow wave structure is complicated. There are many factors which influence the operation of the BWO, such as the coupling between the electron beam and the various electromagnetic modes, space charge effects, and end reflections of the electromagnetic waves at the boundaries. There are a number of papers which describe these effects for uniform BWOs [7-11]. However, for a nonuniform BWO, assumptions used previously in analyzing uniform structures cannot be used to yield an analytical solution. Even without a complete analytical description of a nonuniform BWO, a simple analysis of the phase relationship between the electron beam and the longitudinal electric field of the TM_{01} mode can demonstrate the efficiency enhancement of this tube [see Ref. 3 and references therein].

A phase analysis compares the changes in phase of the longitudinal electric field of the TM_{01} mode seen by an electron as it transits the tube. An electro[illegible] phase with the electric field when the longitudinal field is at a maximum in the direction of the beam.

Because of the negative electron charge, this results in a maximum deceleration of the electron. When the electron is π radians out of phase, the electric field amplitude is at a maximum, but directed antiparallel to the path of the electron, which results in maximum acceleration of the electron. It is assumed that a TM_{01} mode is present in the BWO at a given phase and with a particular phase velocity. For a uniform beam entering the slow wave structure, the phase of an electron with respect to the electric field is evenly distributed over all phases. One half of the electrons will observe phases between $-\pi/2$ and $\pi/2$ and will be decelerated, while the remaining electrons will observe phases between $\pi/2$ and $3\pi/2$ and will be accelerated.

One measure of BWO operation is to compare the change in the kinetic energy of the electron beam as it propagates through a slow wave structure because the BWO transforms electron kinetic energy into radiated microwave energy. In effect, for a given configuration, the maximum theoretical BWO efficiency is determined by the net change in the kinetic energy of the electron beam.

We present a phase model that calculates the change in kinetic energy for each initial electron phase and then averages over all such initial phases. For a given slow wave structure and a uniform electron beam, the net exchange of energy from the electron beam to electromagnetic energy is limited due to the overall spacial averaging of the phases along the length of the tube. At the beginning of the tube there is no net exchange of energy since an equal number of electrons are accelerated as are decelerated. The phase of the electric field, θ, within the slow wave structure is given by

$$\theta = \theta_0 + \omega t - kz, \tag{1}$$

where θ_0 is the phase observed by an electron when it first enters the tube. The rate of change of the phase of the electromagnetic wave observed by an electron moving with velocity, v_e, is

$$\frac{d\theta}{dt} = \omega - k\frac{dz}{dt} = \omega - k\,v_e = \omega\left(1 - \frac{v_e}{v_{ph}}\right), \qquad (2)$$

where v_{ph} is the phase velocity of the electric field. Electrons that are accelerated have a greater rate of phase change than decelerated electrons. As an electron's phase changes, it switches back and forth between accelerating and decelerating phases. However, since faster electrons change their phase more rapidly than slower electrons, electrons will spend more time decelerating than accelerating, resulting in a net loss of kinetic energy.

The equations we present were originally derived by Kovalev [see Ref. 2 and references therein] and describe the changes in electric field, kinetic energy and phase of the electron as a function of position in the slow wave structure. Dimensionless variables are used, with 'W' corresponding to electron kinetic energy, 'a' to electric field amplitude, 'θ' to electron phase, and 'ξ' to longitudinal position. The three equations are:

$$\frac{da}{d\xi} = I\int_0^{2\pi} e^{i\theta}\,d\theta_0\,, \qquad (3)$$

$$\frac{d\theta}{d\xi} = 2\gamma_0^2\left[\frac{W}{\sqrt{W^2 - \gamma_0^{-2}}} - \frac{1}{\beta(\xi)}\right], \text{ and} \qquad (4)$$

$$\frac{dW}{d\xi} = \mathrm{Re}\left\{\left(a - i\alpha\int_0^{2\pi} e^{i\theta}\,d\theta_0\right)e^{-i\theta}\right\}, \qquad (5)$$

where $\beta = \frac{v_{ph}}{c}$, v_{ph} is the phase velocity of the slow EM wave, and c is the speed of light. In addition, the dimensionless variables are defined as

$a = \frac{2\gamma_0 e}{mc^2 k} E$, $\xi = \frac{kz}{2\gamma_0}$, $I = \frac{2\gamma_0^5 e}{\pi(\gamma_0^2 - 1) mc^2} J Z$,

$W = \frac{\gamma}{\gamma_0}$, $\alpha = \frac{4 e \gamma_0^2 J}{\pi(\gamma_0^2 - 1)^{3/2} mc^3} T$, where Z is the coupling impedance and J is the beam current. Finally,

$$T = \frac{I_0(pr_b)}{I_0(pr_0)}\left[I_0(pr_0) K_0(pr_b) - I_0(pr_b) K_0(pr_0) \right] \text{, and} \tag{6}$$

K_0 and I_0 are the zero-order Neumann and modified Bessel functions, respectively, r_0 is the average waveguide radius, r_b is the beam radius, and p is the transverse wave number of the EM wave.

These equation are solved using a computer model in which there are N particles whose kinetic energies and phases are calculated in increments of longitudinal position. Each particle observes a different initial phase at the entrance to the slow wave structure. The initial phases are evenly distributed over 2π radians. For each incremental step in z, the change in kinetic energy and observed phase for each particle is calculated. The observed phases of all the particles are then averaged to yield the change in electric field amplitude. At the end of the slow wave structure, the kinetic energy is averaged over all particles and compared with the initial kinetic energy to yield a maximum conversion efficiency.

Figures 8 and 9 illustrate the results from two calculations using the model described above, and show the effects of prebunching the electron beam. (The beam and slow wave structure parameters are similar, though not identical to the experimental configuration.) The plots show the normalized electron kinetic energy as a function of position along the slow wave structure. Each line represents a different phase initially observed by an electron. Figure 8 has the initial phases evenly distributed over 2π radians. The net loss of electron kinetic energy in this case is 9.4%. In Fig. 9, the initial phases were distributed so that two thirds of the electrons entered the tube observing initial phases between π and 2π radians, in effect prebunching the beam. The loss of electron kinetic energy in this case increased to 15.4%.

This model adds to the understanding of the basic interactions in a nonuniform slow wave structure, but it assumes that the coupling impedance and phase velocity as a function of z are known. To design a tube based on this theory, a slow wave structure would have to be designed with a given coupling impedance and/or phase velocity profile. The difficulty is in experimentally implementing a particular coupling impedance and/or phase velocity distribution.

V. NUMERICAL SIMULATION OF THE NONUNIFORM BWO

In this section we present a detailed discussion of PIC code simulations and comparisons with the experimental results. We have attempted to model the experimental configurations as closely as possible. Quantitative experimental data that can be compared directly with simulation results are radiated power, tube efficiency, the geometrical pattern of the radiated mode, and oscillation frequency. Variations in the values of measured quantities with changes in the geometrical configuration, as described in Sec. III, are compared with simulations to elucidate corresponding differences in the operation of the nonuniform BWO. Preliminary results are presented for long and short tubes #1.

The simulation configuration for long tube #1 is depicted in Fig. 10(a). The nonuniform BWO is constructed by stacking in series multiple sinusoidally shaped rings having identical periods, but different modulation depths. The radius of a uniform section of the BWO is represented by

$$r = r_o\left[1 + \varepsilon \sin\left(2\pi\frac{z}{P}\right)\right], \qquad (7)$$

where r_0 is the average radius of a section, ε is the corresponding form factor, and P is the corresponding period. The parameters for the individual rings were summarized in Table 1.

In Fig. 10(a), the inlet corresponds to the end of the diode anode-cathode gap, and is the plane at which the electron beam is injected into the problem. The inlet is perfectly transmitting to waves having phase velocity c, the speed of light, but cuts off modes of the expected frequency (9.6 GHz), allowing backward traveling waves to be reflected in the forward direction. Thus, relatively little RF power passes through the inlet.

The outlet represents the waveguide that is connected to the antenna. Reflections at the outlet could possibly have a significant impact on the dynamics of a simulation [7]. We consider only cases in which the outlet is perfectly transmitting to waves of the expected frequency. (The transmission coefficient at this boundary is insensitive to changes of less than 10% in wave oscillation frequency, so the matching condition is fixed in all simulations.)

The electron beam parameters used in the simulations are a current and voltage waveform rising to peak values of 4.8 kA and 670 kV, respectively, in 3.0 ns. These values are then maintained for subsequent times. (It was necessary to use an artificially long beam pulse in simulations to attain saturation of the radiated power. This will be discussed in more detail later.)

The applied external magnetic field used to guide the electron beam is shown in Fig. 10(b). The axial dependence of B_z and B_r are calculated using the expressions

$$B_z(r,z) \quad = \quad \frac{B_0}{\left[1+e^{(z-z_0)/\alpha}\right]} \qquad (8),$$

and

$$B_r(r,z) \quad = \quad \frac{B_0}{2\alpha} r \frac{e^{(z-z_0)/\alpha}}{\left[1-e^{(z-z_0)/\alpha}\right]^2} \qquad (9),$$

where B_0 = 2.6 T is the peak amplitude in the uniform field region. The free parameters α and z_0 are set to ensure that the electron beam is dumped beyond the interaction region, but before the outlet. The field described by Eqs. (8) and (9) satisfies the divergence equation.

Figures 11 - 17 contain results from a simulation of long tube #1. Figure 11 shows several different representations of the beam at a time when the RF fields in the BWO have saturated, about 10 ns into the simulation. The beam is clearly modulated. Charge density bunches form as a result of the interaction of a slow space charge wave with a characteristic mode of the RF structure, which, in this case, is a backward traveling surface wave; that is, the wave amplitude is largest near the inner surface of the BWO slow wave structure. As shown if Fig. 11(b), the separation between the bunches represents the spacial wavelength of the mode, which is approximately 1.5 P.

A plot of axial canonical momentum versus z, Fig. 11(b), shows that velocity modulation initially occurs in the section comprised of relatively shallow rings AABBB, where the axial electric field (E_z) is about a factor of two lower than the value in the section with deep ripples CCCDDC. In addition, comparison with Fig. 11(c) indicates that the bunches correspond to minima of axial momentum, which implies that electrons in the bunches see only a decelerating axial electric field, a condition favorable for conversion of electron energy into microwaves.

Additional insight into the general field structure is obtained from a contour plot of E_z, shown in Fig. 12. The contour plot reveals that E_z is largest on axis. This implies the existence of a standard TM mode in addition to the surface wave, whose characteristics are determined solely by the waveguide radius. We refer to this mode as a volume wave. Inspection of the figure indicates that the volume mode has a wavelength of 3.0 P, or twice the wavelength of the surface mode.

Movies of the contours of E_z reveal that the volume wave has both backward and forward traveling components, which combine to form a standing wave upstream of the first D section. These components are necessary to match fields at both ends of the finite length

BWO. Thus, the backward traveling surface mode, which interacts with the electron beam, must convert part of its energy into a backward traveling volume mode to satisfy field matching conditions at the cutoff waveguide, where the volume mode is reflected toward the outlet.

The contrasting radial dependence of surface and volume modes suggests that the surface-to-volume mode conversion efficiency depends on the ratio of ripple depth (d) to average waveguide radius (r_0). When d/r_0 is large, the surface mode dominates because the associated eigenfunction is sufficient to satisfy matching conditions near the inlet. The opposite is true when $d/r_0 << 1$. Partial conversion of the surface mode to a volume mode is conducive to high power operation since the RF power is distributed over the volume of the tube, thereby decreasing field stresses across the gaps of the slow wave structure.

The dual structure of the axial electric field component in long tube #1 is confirmed in the spacial spectrum of E_z. Figures 13(a) and 13(c) contain plots of E_z versus z along lines located at $r = 0.0$ cm (the axis) and $r = 1.2$ cm (near the surface of the rings), respectively. Figures 13(b) and 13(d) are the corresponding spacial spectra. Figure 13(d) reveals that the net field is comprised of components with inverse wavelengths of about 0.2 ($\lambda \approx 3.0$ P), 0.45 ($\lambda \approx 1.5$ P), and 0.675 cm^{-1} ($\lambda \approx$ P). The first two wavelengths belong to the volume and surface waves, respectively. The shortest wavelength corresponds to the RF structure. Comparison of Figs. 13(b) and 13(d) indicates that the volume mode dominates on axis, affirming the previous discussion.

Experimental results presented in Sec. III show that section AABBB has a significant influence on the output power of long tube #1. The fact that simulations show obvious premodulation in this region, in addition to a standing wave pattern for the volume mode, led us to hypothesize that the section with shallow ripples serves as a prebuncher for the downstream section. Prebunching the beam may increase the coupling coefficient in the downstream section, thereby improving tube efficiency, which supplements the conclusions of the phase model presented in Sec. IV.

To ascertain the role of section AABBB, simulations were performed for each of the two BWO sections separately, in correspondence with the experiments. Results corresponding to the simulation of structure CCCDDC are presented below. At this point it suffices to state that the isolated section AABBB does not oscillate and section CCCDDC does, consistent with the experiments. This suggests that, to zeroth order, the downstream section of long tube #1 determines the characteristics (for example, start current [7,10] and frequency) of the entire tube. Using this result in conjunction with previous statements concerning the spacial structure of the axial electric field, an approximate dispersion diagram for long tube #1 can be constructed.

Figure 14 is a plot of frequency (f) versus wave number (k_0) for an infinitely long, uniform BWO comprised of type C sections, which is only slightly different from structure CCCDDC and should therefore have similar dispersion characteristics. Because the actual tube is finite in length, the mode structure is discrete. The discrete modes observed in simulations are indicated in the figure by the points labeled #1, #2, and #3, which were established by matching known spacial wavelengths with corresponding frequencies on the dispersion diagram. The beam-line ($f = v_e k_0/2\pi$) coincides approximately with the light-line. The point where the slow space charge wave interacts with the TM_{01} mode is labeled #3. This interaction gives rise to a backward traveling slow wave that partially converts into a backward traveling fast wave, labeled #1. The fast wave reflects at the cutoff waveguide giving rise to a forward traveling fast wave, labeled #2, which is ultimately radiated. Although the dispersion diagram is not exact, it provides a simplified picture of the wave dynamics inherent in nonuniform BWO operation, which, in addition, is qualitatively consistent with numerical simulation.

The dispersion diagram indicates that the oscillation frequency of long tube #1 is approximately 9.8 GHz. In the simulation of long tube #1, the frequency is determined by Fourier analyzing the time dependent RF voltage developed across the gaps formed by the slow wave structure. Figure 15(a) is a time history of the voltage across the gap formed by the second and third C sections. Figure 15(b) is the corresponding Fourier spectrum, which shows that the dominant mode oscillation frequency is 9.51 GHz, in agreement with the experiment. In addition, experiments showed that the corresponding radiation pattern is consistent with a TM_{01} mode, which supports the picture of internal wave dynamics suggested by simulations.

A figure of merit for the nonuniform BWO is radiated power, or equivalently, efficiency. In simulations, the instantaneous radiated power is obtained from the integral of the Poynting vector over the cross-section of the outlet. Figure 16 is a plot of instantaneous radiated power versus time for long tube #1. Included on the plot is the beam power pulse. The average radiated power, which is the quantity measured experimentally, is about 1/2 the instantaneous power. Thus, the simulation shows that the average radiated power varies from 150 MW to 100 MW, which is about a factor of three lower than values obtained experimentally. Much of this discrepancy is due to the fact that it was necessary to use a time-biased, implicit field algorithm [12] in the simulations to eliminate large amplitude, high frequency noise observed when a computationally faster explicit scheme was used. Unfortunately, the time biased algorithm damps physical modes in addition to those which are numerical. Nevertheless, qualitative behavior and trends remain valid.

Simulations show that the radiated power pulse is significantly delayed compared with the beam power pulse. This contrasts with experimental measurements, which show that the radiated power signal tracks the beam power pulse. This discrepancy may be due to a difference in quality factors (Q), which is discussed in more detail below.

As was mentioned earlier, the power radiated from long tube #1 decreased significantly when section AABBB was removed. The corresponding simulation shows the opposite behavior. Figure 17(a) is a plot of electron charge density contours superimposed on a schematic of short tube #1. Similar to long tube #1, bunching occurs with a wavelength of 1.5 P, although the oscillation frequency has increased to 9.77 GHz, in agreement with experiment. Without section AABBB there is no premodulation of the beam.

Time histories of the input beam power and radiated RF power are compared in Fig. 17(b). Comparison with Fig. 16 reveals that, despite the absence of any premodulation, the output power has more than doubled, in contrast with experimental observations. An explanation for this is suggested by the long rise to saturation of the simulated output power pulse, which is neither observed in experiments nor in simulations of long tube #1.

The long rise time of the radiated power is indicative of a cavity resonance, which is unique to the simulated version of short tube #1. The cavity resonance has an associated quality factor Q, which causes the tube to have a finite bandwidth. For frequencies outside of this band, the tube efficiency is dependent only on the coupling coefficient of the BWO. However, for frequencies within the band, tube efficiency becomes dependent on the cavity Q, in addition to the coupling coefficient. This is exemplified in Fig. 18, which shows the results of a numerical cold test (no electron beam) for long and short tubes #1.

Cold test results were obtained by exciting the volume TM_{01} mode in each tube and plotting the resulting stored magnetic field energy versus frequency. The peak of the resulting curve corresponds to a resonance. Inspection of the figure shows that long tube #1 has a much narrower bandwidth than short tube #1. The operating frequency of each tube is indicated by a vertical unit tick mark on the plot. The presence of the beam shifts the resonance curves to slightly higher frequencies, due to space charge effects, in addition to increasing their respective bandwidths. This suggests that, in the presence of a beam, short tube #1 operates closer to resonance than does long tube #1, which explains why short tube #1 produces more output power than long tube #1 in the simulations.

The quality factor in experiments is likely to be much lower than in corresponding simulations as a result of power loss in conductors, through joints connecting conductors, and in extraneous plasma, all of which are absent in simulations. Therefore, the existence of a resonance in either long tube #1 or short tube #1 would have little effect on power output, the latter being determined exclusively by the coupling coefficient. This may explain why short tube #1 produces less output power than long tube #1 in experiments. It also suggests that output power could be increased in either tube by reducing internal losses, and operating near a resonance.

Simulations of the nonuniform BWO suggest that both surface and volume TM modes determine tube efficiency. The surface mode is the usual backward traveling TM wave produced through the interaction of the electron beam with the RF structure. Because of the finite length and nonuniform nature of the RF structure, forward and backward traveling volume (fast) TM waves are also generated, which form a standing wave pattern in the section of tube with shallow ripples. The net field in this region of the tube causes the beam to become modulated, which may increase the coupling coefficient downstream, thereby increasing efficiency. In addition, for an appropriate length, the beam may give up energy to the standing wave through transit time effects, which would increase tube efficiency above what is possible in a uniform BWO.

Conclusions

The nonuniform amplitude BWOs tested resulted in peak RF efficiencies of 15 to 25%. The maximum values for RF efficiencies occurred at approximately twice the start current. When the two sections of long tube #1 were tested individually, the initial shallow ripple section did not radiate measurable RF power and the second deeper ripple section showed RF efficiencies of approximately one third of the full length tube. The increased efficiency of the two section BWOs can be attributed to the prebunching of the electron beam by the initial section.

A phase analysis suggested that prebunching of the electron beam yields significant increase in radiation efficiency. The model is most useful for gaining insight in to the physical mechanisms for the efficiency enhancement, as opposed to designing a particular tube.

TWOQUICK simulations provided a comprehensive picture of the interaction of the surface mode and volume mode inside the slow wave structure. Simulation results were sensitive to the cavity Q's of the set-up. Agreement with experimental measurements were good when the simulations were not near a resonance.

This paper has presented a limited set of results from work in progress. Many more slow wave structure configurations are being studied in an attempt to further increase observed microwave generation efficiencies. These experiments are being performed in coordination with PIC code simulations.

ACKNOWLEDGMENTS

The work at the University of New Mexico is support by Air Force Office of Scientific Research Grant #F429620-92-J-0157DEF. The work at Sandia National Laboratories is supported in part by Air Force Phillips Laboratory and the Department of Energy.

References

[1] See, for example, J. Benford and J. Swegle, High-Power Microwaves. Boston: Artech House, 1992, Chap. 6 and references therein.

[2] N. F. Kovalev and V. I. Petrukhina, "Ultra-relativistic carcinotron with a jump in beam-rf coupling," Electr. Techn. SVCH, vol. 7, pp. 101-105, 1977 (in Russian).

[3] S. D. Korovin, S. D. Polevin, A. M. Roitman, and V. V. Rostov, "Relativistic backward wave tube with variable phase velocity," Sov. Tech. Phys. Lett., vol. 18, pp. 265-266, 1992.

[4] D. B. Seidel and T. D. Pointon, Sandia National Laboratories, private communication.

[5] B. Goplen, R. E. Clark, J. McDonald, and W. M. Bollen, Users Manual for MAGIC, Mission Res. Corp., Alexandria, VA, Rep. No. MRC/WDC-R-068, 1983.

[6] R. A. Koslover, Computer code "TM0n," SEAC, Albuquerque NM, 1988.

[7] B. Levush, T. M. Antonsen, Jr., A. Bromborsky, W. Lou, and Y. Carmel, "Theory of relativistic backward-wave oscillators with end reflections," IEEE Trans. on Plasma Science, vol. 20, pp. 263-280, 1992.

[8] B. Levush, T. M. Antonsen, Jr., A. Bromborsky, W. Lou, and Y. Carmel, "Relativistic backward-wave oscillators: theory and experiment," Phys. Fluids B, vol. 4, pp. 2293-2299, 1992.

[9] J. A. Swegle, J. W. Poukey, and G. T. Leifeste, "Backward wave oscillators with rippled wall resonators: analytic theory and numerical simulation," Phys. Fluids, vol. 28, pp. 2882-2894, 1985.

[10] J. A. Swegle, "Starting conditions for relativistic backward wave oscillators at low currents," Phys. Fluids, vol. 30, pp. 1201-1211, 1987.

[11] V.L. Bratman, G.G. Denisov, M.M. Ofitserov, S.D. Korovin, S.D. Polevin, and V.V. Rostov, "Millimeter-wave HF relativistic electron oscillators," IEEE Trans. on Plasma Science, vol. 15, pp. 2-15, 1987.

[12] B. B. Godfrey, "Time-biased field solver for electromagnetic PIC codes," presented at the Ninth Conference on Numerical Simulation of Plasmas, Northwestern University, June 30 - July 2, 1980.

Table Captions

TABLE 1. Dimensions of Slow Wave Structure Rings.

TABLE 2. Summary of Experimental Tube Configurations and Results.

Figure Captions

FIGURE 1. Cut-away diagram of the Sinus-6 accelerator. The various components (1-4) are described in the text.

FIGURE 2. Typical voltage and current waveforms from the Sinus-6 accelerator.

FIGURE 3. Diagram of experimental setup used to measure microwave power and frequency. A resistive sensor is used to measured radiated power density (left), and a crystal diode and a balanced mixer are used to measure microwave power and frequency, respectively (right).

FIGURE 4. Measured and calculated radiation pattern for a TM_{01} mode.

FIGURE 5. Dependence of peak microwave power on electron beam current.

FIGURE 6 RF efficiency as a function of electron beam current.

FIGURE 7. Peak RF power as a function of electron beam power.

FIGURE 8. Energy change of 6 electrons as a function of normalized position down a tube. Each of these electron entered the tube at a different phase with respect to the observed electromagnetic field. The phases of the 6 electrons were uniformly distributed over 2π radians.

FIGURE 9. Energy change of 6 electrons as a function of normalized position down a tube. Each of these electron entered the tube at a different phase with respect to the observed electromagnetic field. In this case, the initial phases were distributed so that two thirds of the electrons entered the tube observing initial phases between π and 2π radians, in effect prebunching the beam.

FIGURE 10. (a) Simulation configuration for long tube #1. Upper-case letters label the various rings comprising the slow wave structure. The electron beam is injected at the left and microwaves are radiated out the right. (b) Axial dependence of the applied magnetic guide field at the radial location $r = 1.0$ cm, which corresponds to the position of maximum current density.

FIGURE 11. (a) Configuration space of the electron beam. (b) Particle plot of the z-component of canonical momentum (normalized to the electron mass times the speed of light). (c) Contour plot of electron charge density, which shows that the electron beam is modulated with a corresponding wavelength of 1.5 P.

FIGURE 12. Contour plot of E_z, which shows that the peak field occurs on axis, indicative of a volume mode, with a period of 3.0 P.

FIGURE 13. (a) Plot of E_z vs. z at $r = 0.0$ cm, and (b) the corresponding Fourier spectrum. (c) and (d) are similar plots for $r = 1.2$ cm. As expected, the amplitude of the volume mode decreases with increasing r.

FIGURE 14. Approximate dispersion diagram for long tube #1 showing the first two passbands. The points labeled #1, #2, and #3, correspond to the forward traveling volume wave, the backward traveling volume wave, and the backward traveling surface wave, respectively. These points were established using the wavelengths obtained from the spacial spectrum of E_z (Fig. 13).

FIGURE 15. (a) Time history of the voltage across the gap between the second and third C sections in long tube #1, and (b) the corresponding frequency spectrum.

FIGURE 16. Input beam power and output RF power versus time for long tube #1.

FIGURE 17. (a) Contour plot of electron charge density superimposed on the simulation configuration for short tube #1. (b) The corresponding plot of input beam power and output RF power versus time for long tube #1.

FIGURE 18. Plot of magnetic field energy versus frequency obtained from a cold test of long and short tubes #1. The peak of a curve corresponds to the resonant frequency of the tube. The operating frequency of each tube (in the presence of the beam) is indicated by unit length, vertical tick marks located at $f = 9.51$ GHz (long tube #1) and $f = 9.77$ GHz (short tube #1).

Table Captions

TABLE 1. Dimensions of Slow Wave Structure Rings.

TABLE 2. Summary of Experimental Tube Configurations and Results.

	Tube Configuration	Relative Power	Frequency ±0.05 [GHz]
Long Tube #1	A-A-B-B-B-C-C-C-D-D-C	1.00	9.50
Long Tube #1a	A-A-A-B-B-B-C-C-D-D-C	0.27	9.50
Long Tube #1b	A-B-B-B-C-C-C-C-D-D-C	0.94	9.50
Short Tube #1	C-C-C-D-D-C	0.36	9.75

Ring Type	Maximum Radius [cm]	Minimum Radius [cm]	Average Radius [cm]	Ripple Amplitude [cm]	Form Factor	Ripple Period [cm]
A	1.65	1.45	1.550	0.100	0.065	1.50
B	1.65	1.38	1.515	0.135	0.090	1.50
C	1.65	1.20	1.425	0.225	0.158	1.50
D	1.65	1.15	1.400	0.250	0.179	1.50

Figure Captions

FIGURE 1. Cut-away diagram of the Sinus-6 accelerator. The various components (1-4) are described in the text.

FIGURE 2. Typical voltage and current waveforms from the Sinus-6 accelerator.

FIGURE 3. Diagram of experimental setup used to measure microwave power and frequency. A resistive sensor is used to measured radiated power density (left), and a crystal diode and a balanced mixer are used to measure microwave power and frequency, respectively (right).

FIGURE 4 Measured and calculated radiation pattern for a TM_{01} mode.

FIGURE 5. Dependence of peak microwave power on electron beam current.

FIGURE 6 RF efficiency as a function of electron beam current.

FIGURE 7. Peak RF power as a function of electron beam power.

FIGURE 8. Energy change of 6 electrons as a function of normalized position down a tube. Each of these electron entered the tube at a different phase with respect to the observed electromagnetic field. The phases of the 6 electrons were uniformly distributed over 2π radians.

FIGURE 9. Energy change of 6 electrons as a function of normalized position down a tube. Each of these electron entered the tube at a different phase with respect to the observed electromagnetic field. In this case, the initial phases were distributed so that two thirds of the electrons entered the tube observing initial phases between π and 2π radians, in effect prebunching the beam.

FIGURE 10. (a) Simulation configuration for long tube #1. Upper-case letters label the various rings comprising the slow wave structure. The electron beam is injected at the left and microwaves are radiated out the right. (b) Axial dependence of the applied magnetic guide field at the radial location $r = 1.0$ cm, which corresponds to the position of maximum current density.

FIGURE 11. (a) Configuration space of the electron beam. (b) Particle plot of the z-component of canonical momentum (normalized to the electron mass times the speed of light). (c) Contour plot of electron charge density, which shows that the electron beam is modulated with a corresponding wavelength of 1.5 P.

FIGURE 12. Contour plot of E_z, which shows that the peak field occurs on axis, indicative of a volume mode, with a period of 3.0 P.

FIGURE 13. (a) Plot of E_z vs. z at $r = 0.0$ cm, and (b) the corresponding Fourier spectrum. (c) and (d) are similar plots for $r = 1.2$ cm. As expected, the amplitude of the volume mode decreases with increasing r.

FIGURE 14. Approximate dispersion diagram for long tube #1, showing the first two passbands. The points labeled #1, #2, and #3, correspond to the forward traveling volume wave, the backward traveling volume wave, and the backward traveling surface wave, respectively. These points were established using the wavelengths obtained from the spacial spectrum of E_z (Fig. 13).

FIGURE 15. (a) Time history of the voltage across the gap between the second and third C sections in long tube #1, and (b) the corresponding frequency spectrum.

FIGURE 16. Input beam power and output RF power versus time for long tube #1.

FIGURE 17. (a) Contour plot of electron charge density superimposed on the simulation configuration for short tube #1. (b) The corresponding plot of input beam power and output RF power versus time for long tube #1.

FIGURE 18. Plot of magnetic field energy versus frequency obtained from a cold test of long and short tubes #1. The peak of a curve corresponds to the resonant frequency of the tube. The operating frequency of each tube (in the presence of the beam) is indicated by unit length, vertical tick marks located at f = 9.51 GHz (long tube #1) and f = 9.77 GHz (short tube #1).

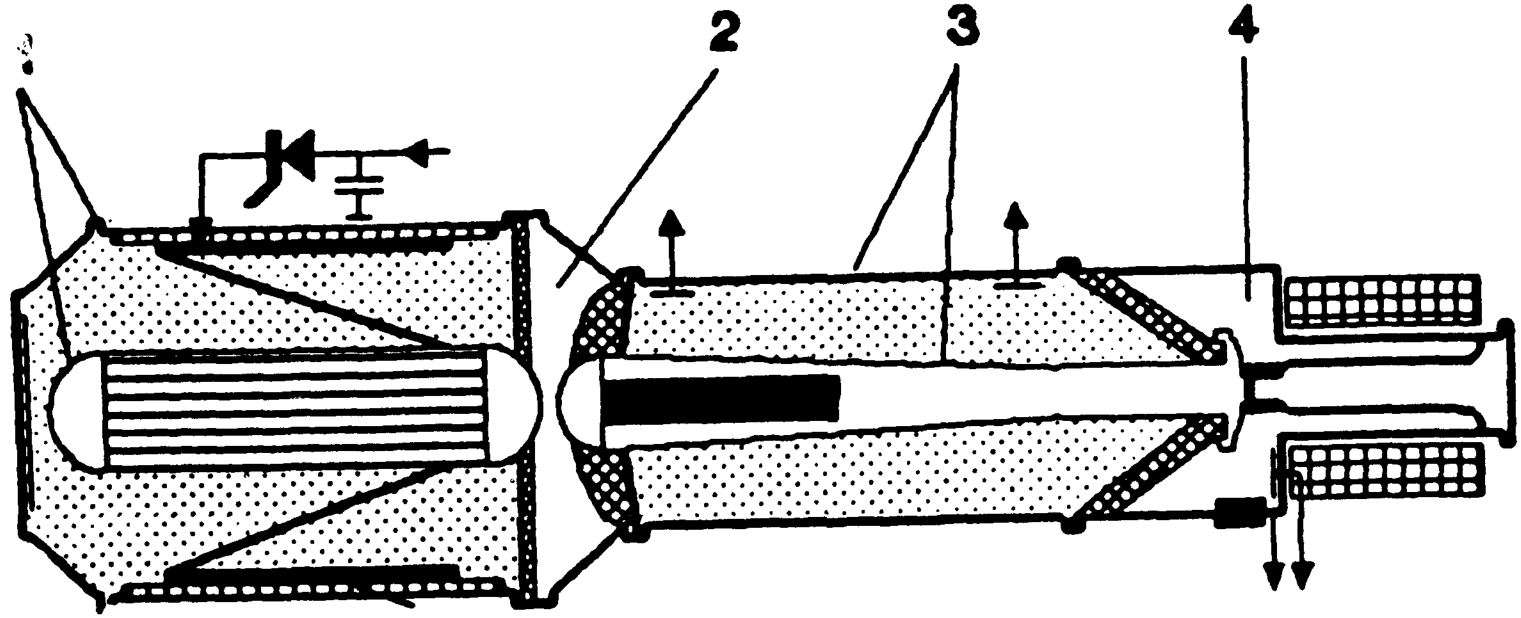
2
3
4

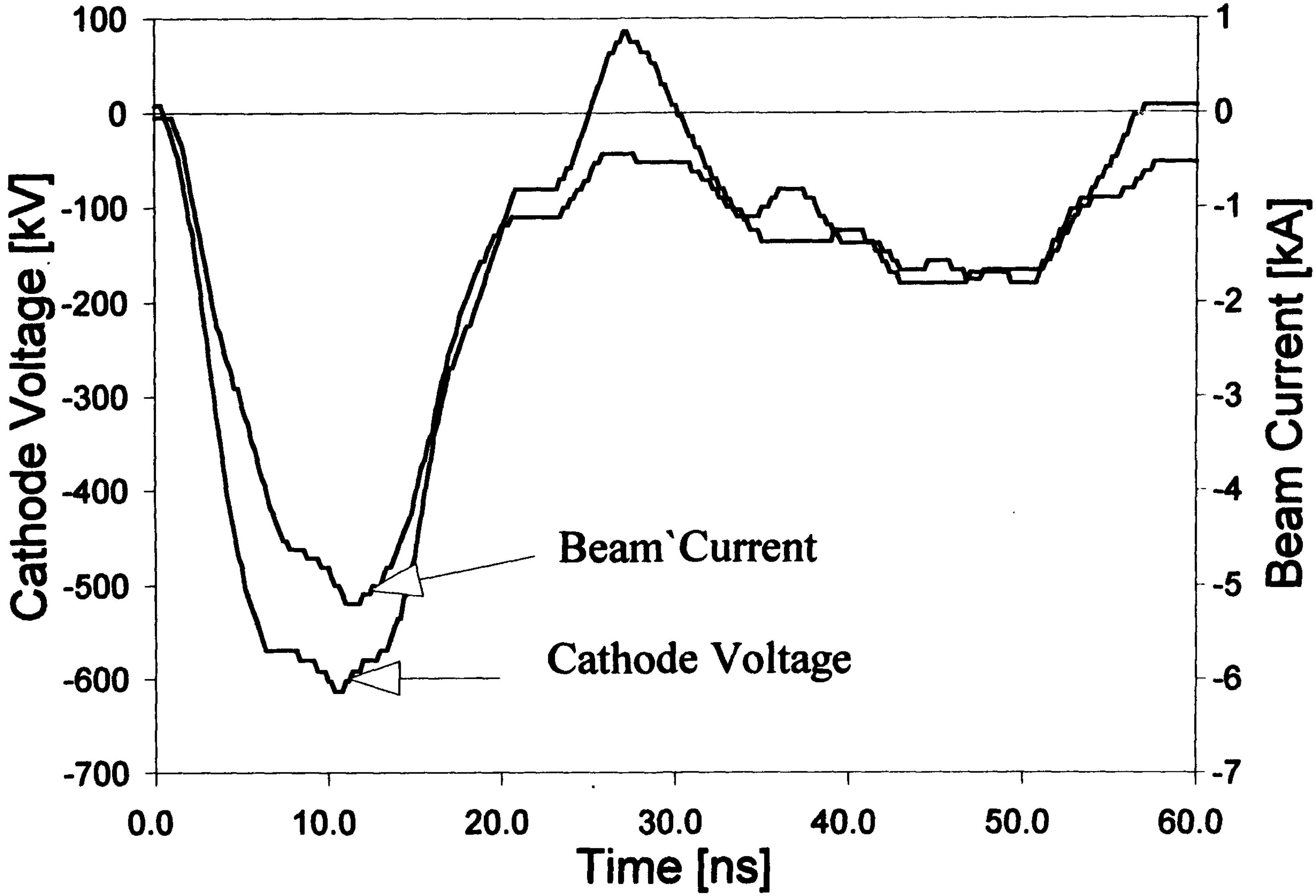

Cathode Voltage [kV]
100
0
-100
-200
-300
-400
-500
-600
-700
Beam Current [kA]
1
0
-1
-2
-3
-4
-5
-6
-7
0.0
10.0
20.0
30.0
40.0
50.0
60.0
Time [ns]
Beam`Current
Cathode Voltage

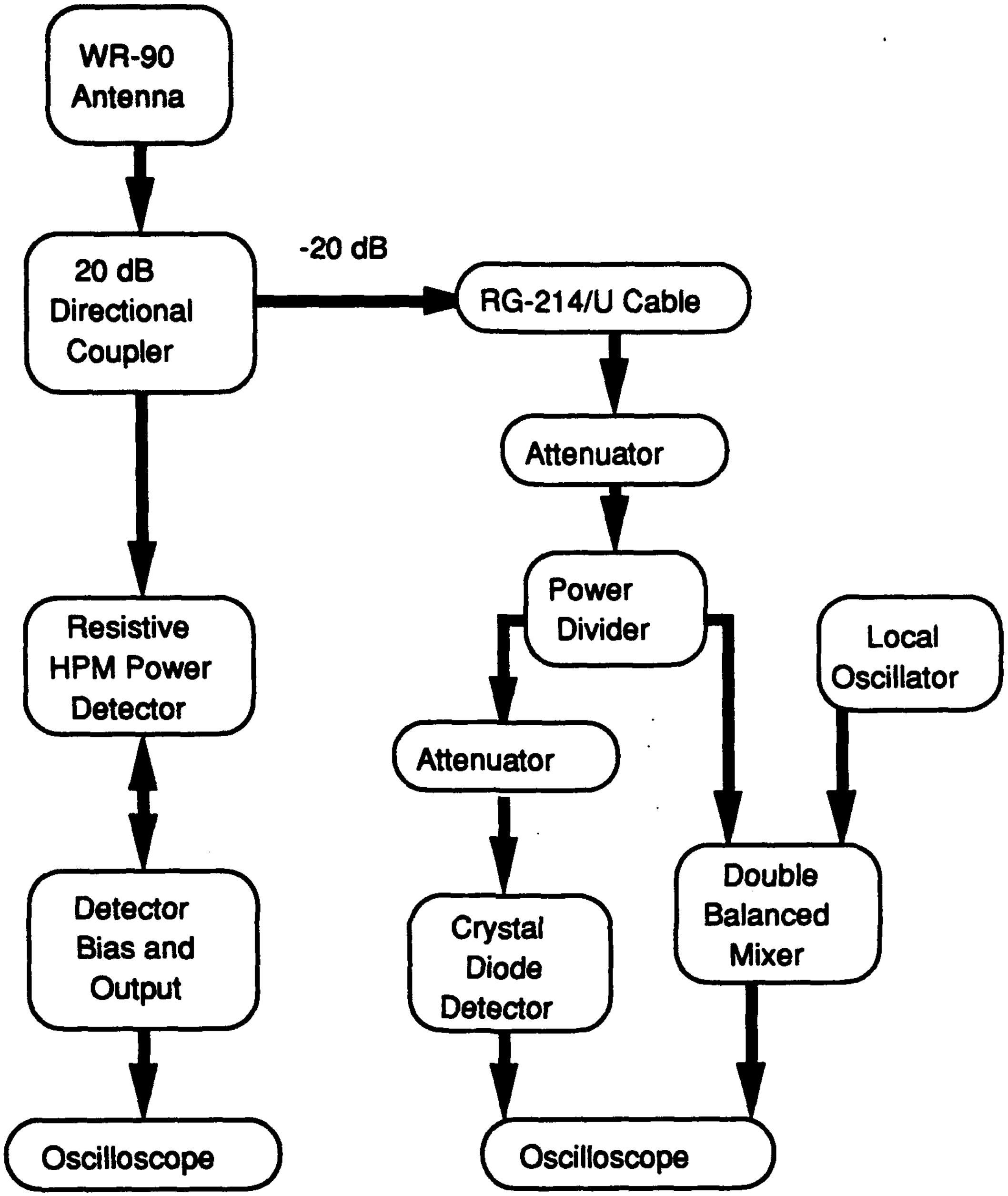
WR-90 Antenna
20 dB Directional Coupler
-20 dB
RG-214/U Cable
Attenuator
Power Divider
Local Oscillator
Resistive HPM Power Detector
Attenuator
Double Balanced Mixer
Crystal Diode Detector
Detector Bias and Output
Oscilloscope
Oscilloscope

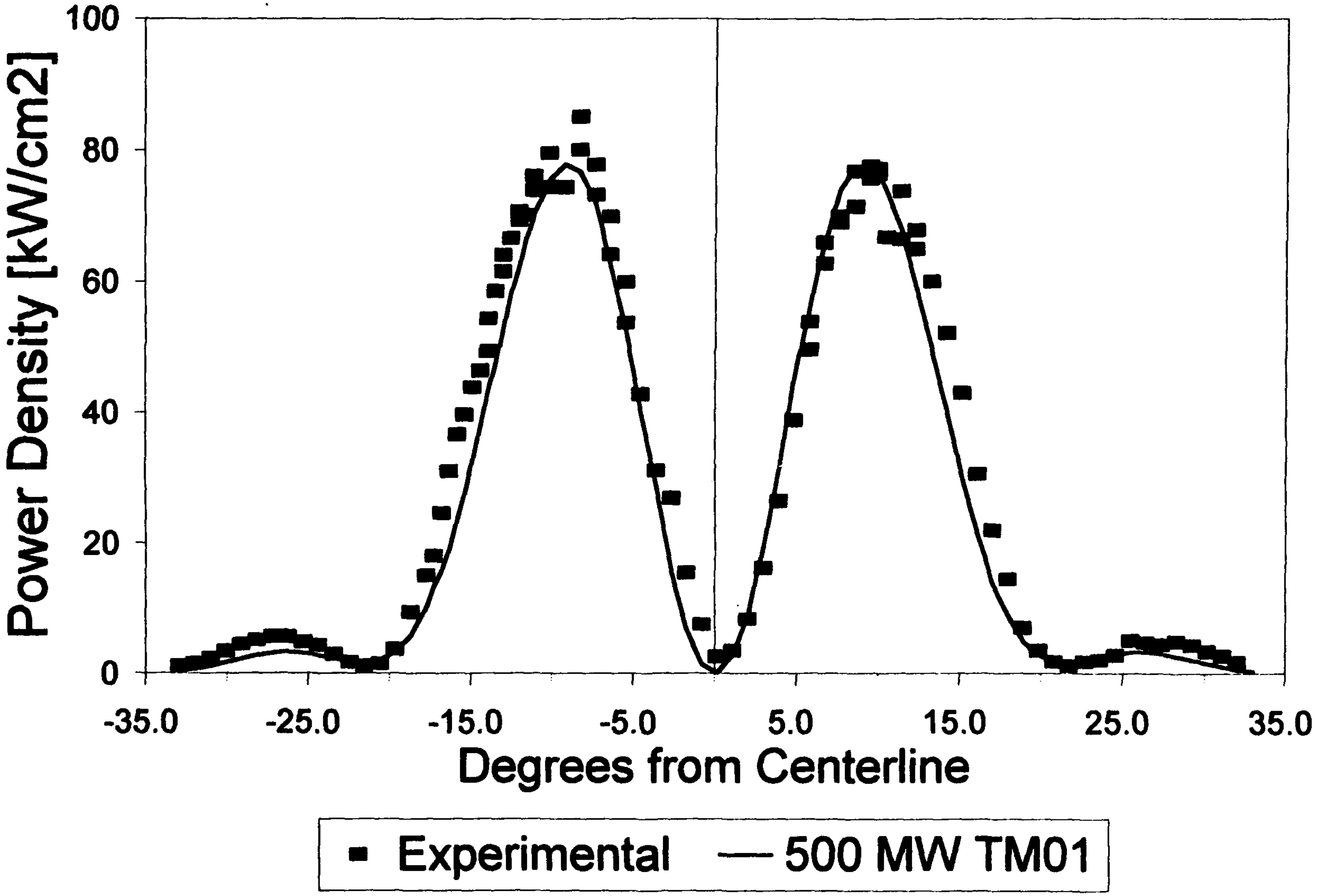
Power Density [kW/cm2]
100
80
60
40
20
0
-35.0
-25.0
-15.0
-5.0
5.0
15.0
25.0
35.0
Degrees from Centerline
Experimental
500 MW TM01

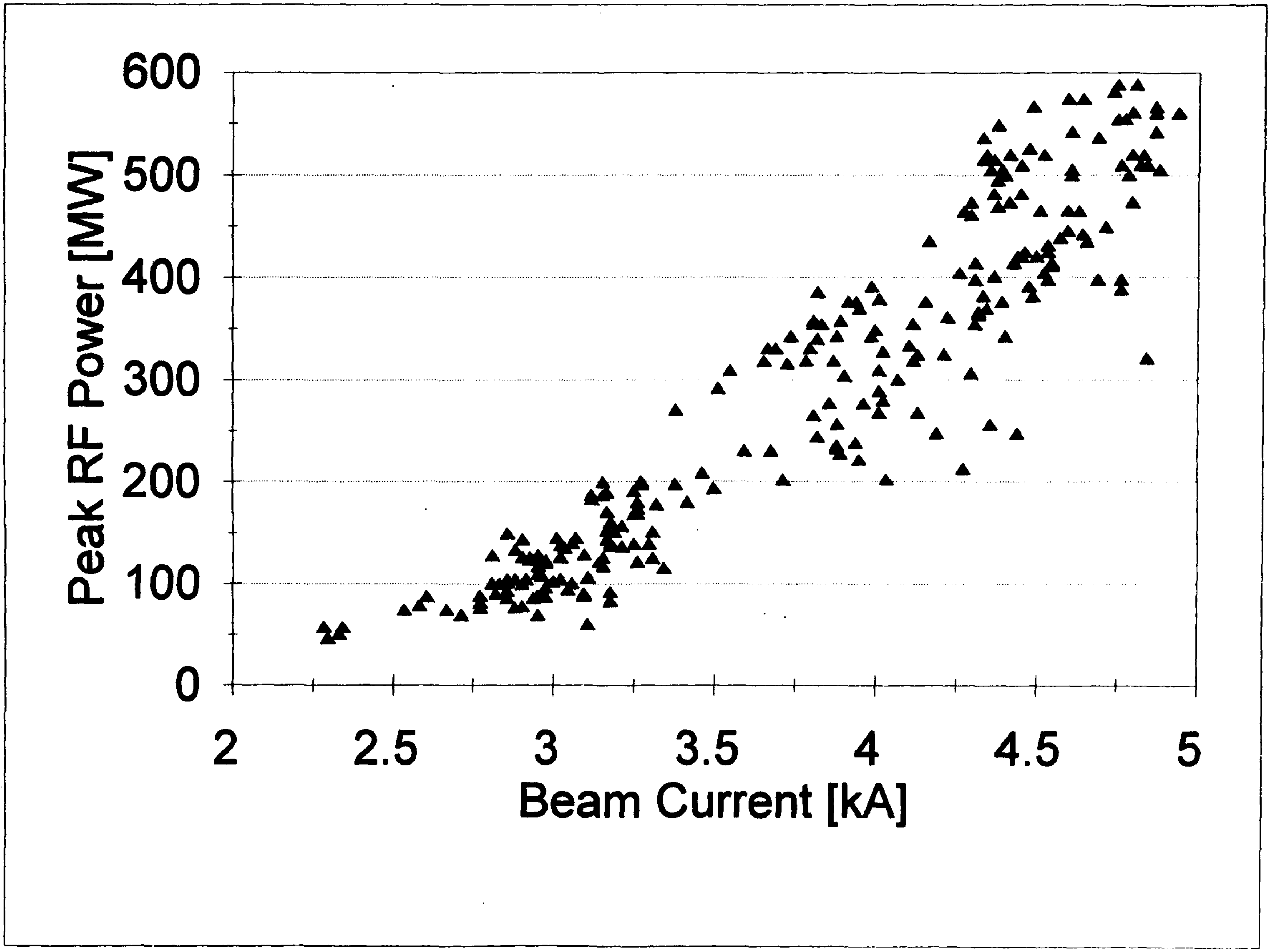

Peak RF Power [MW]
600
500
400
300
200
100
0
2
2.5
3
3.5
4
4.5
5
Beam Current [kA]

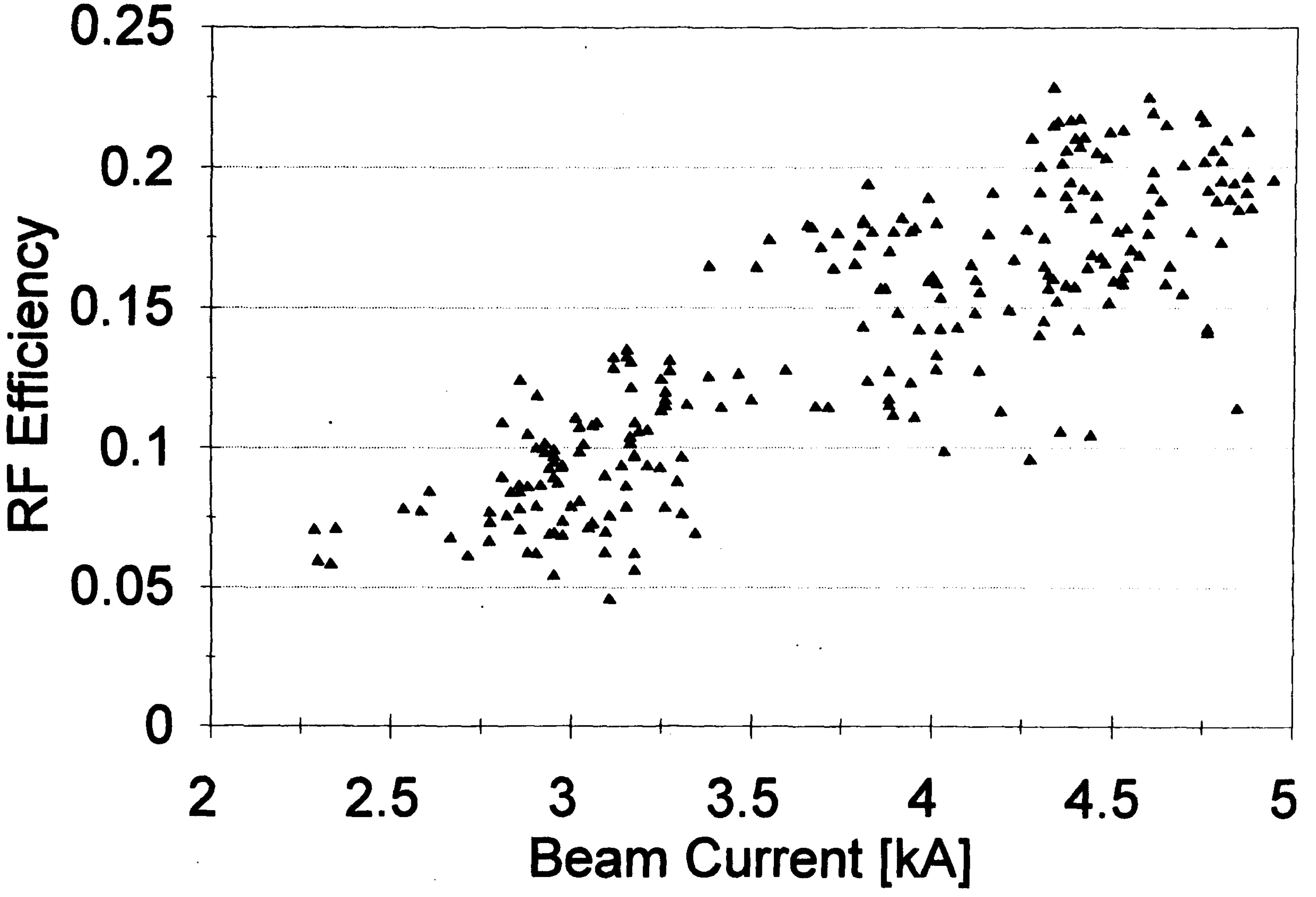
0.25
0.2
0.15
0.1
0.05
0
RF Efficiency
2
2.5
3
3.5
4
4.5
5
Beam Current [kA]

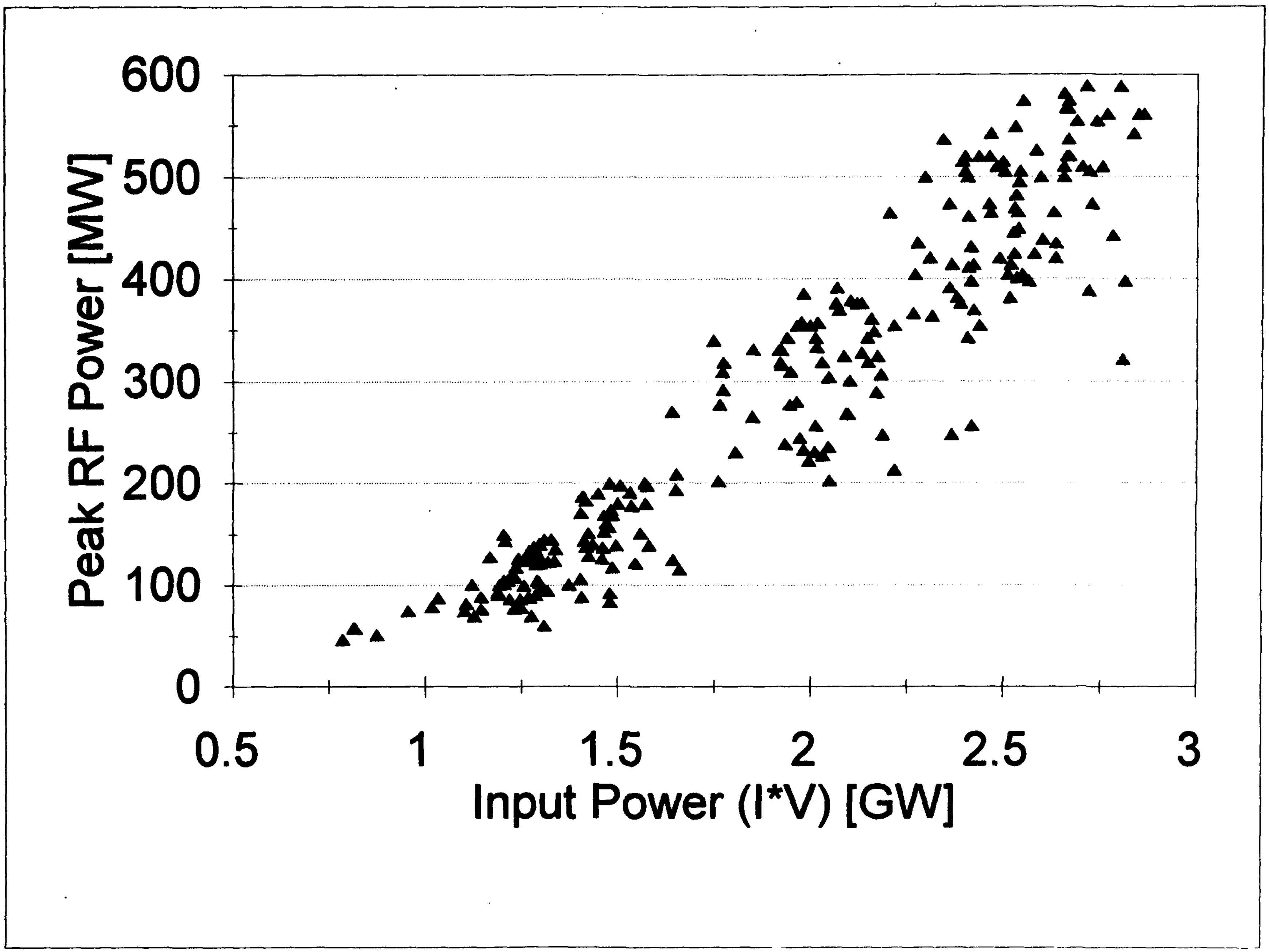
Peak RF Power [MW]
600
500
400
300
200
100
0
0.5
1
1.5
2
2.5
3
Input Power (I*V) [GW]

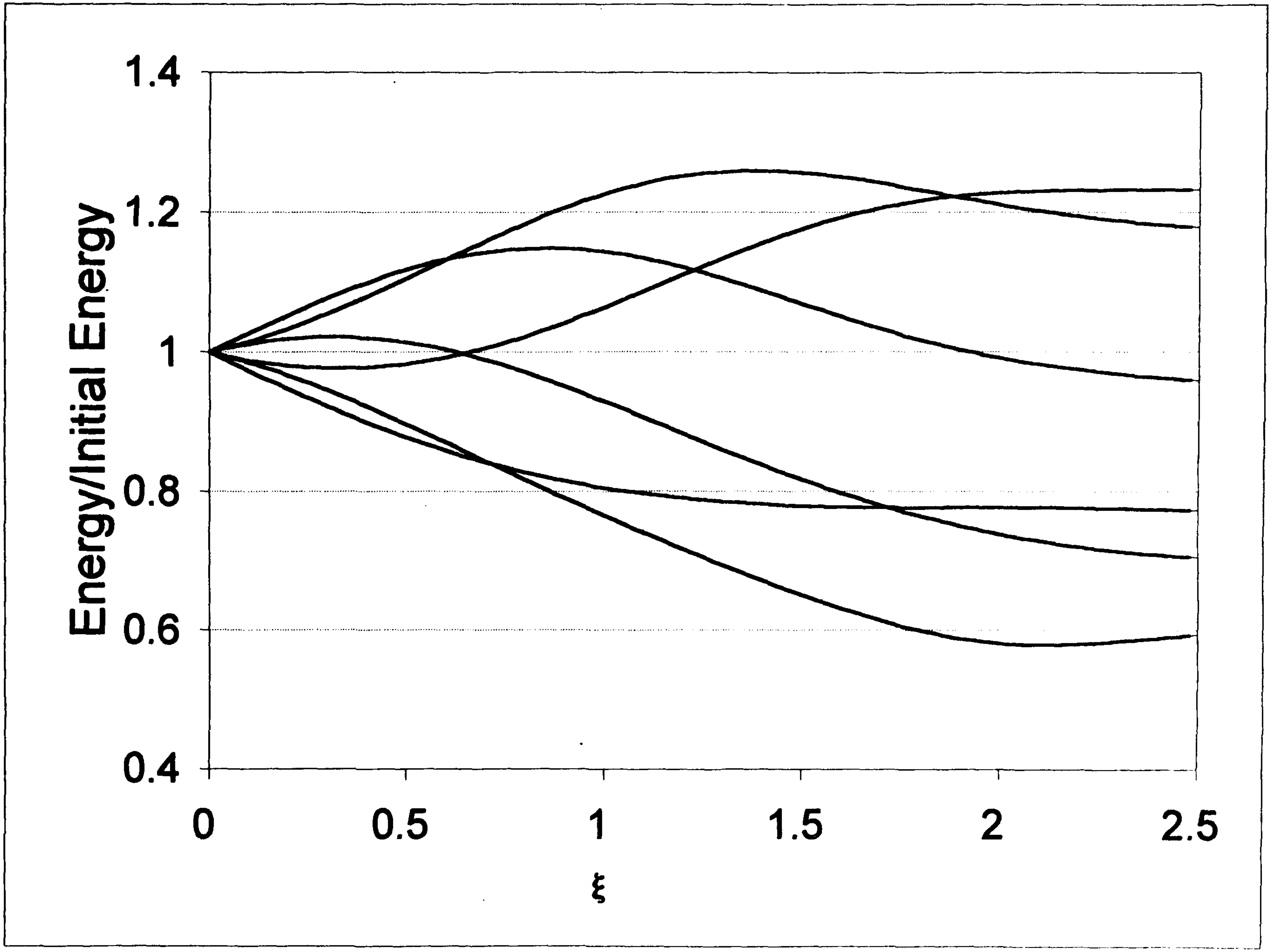

1.4
1.2
1
0.8
0.6
0.4
Energy/Initial Energy
0
0.5
1
1.5
2
2.5
ξ

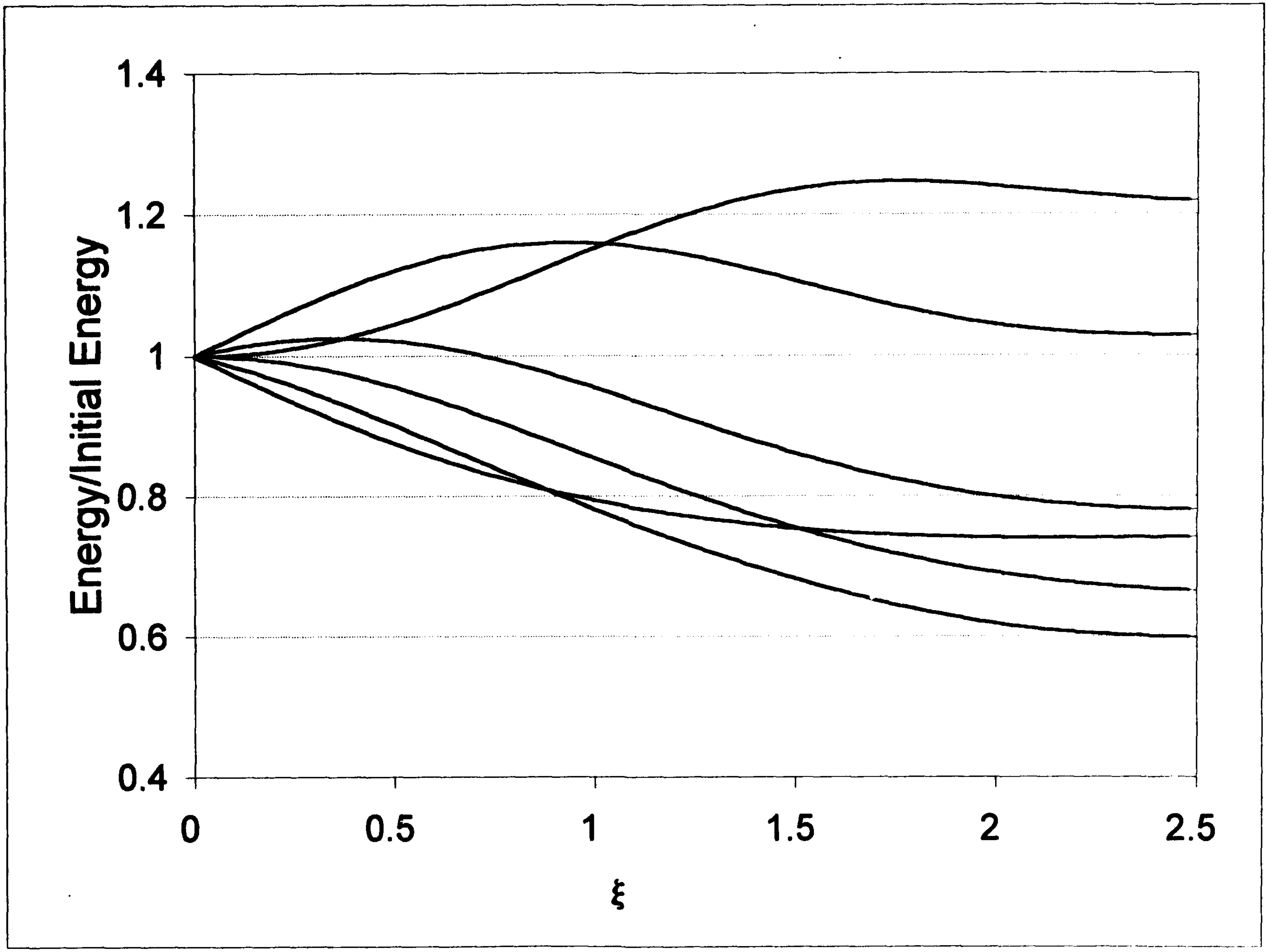
1.4
1.2
1
0.8
0.6
0.4
Energy/Initial Energy
0
0.5
1
1.5
2
2.5
ξ

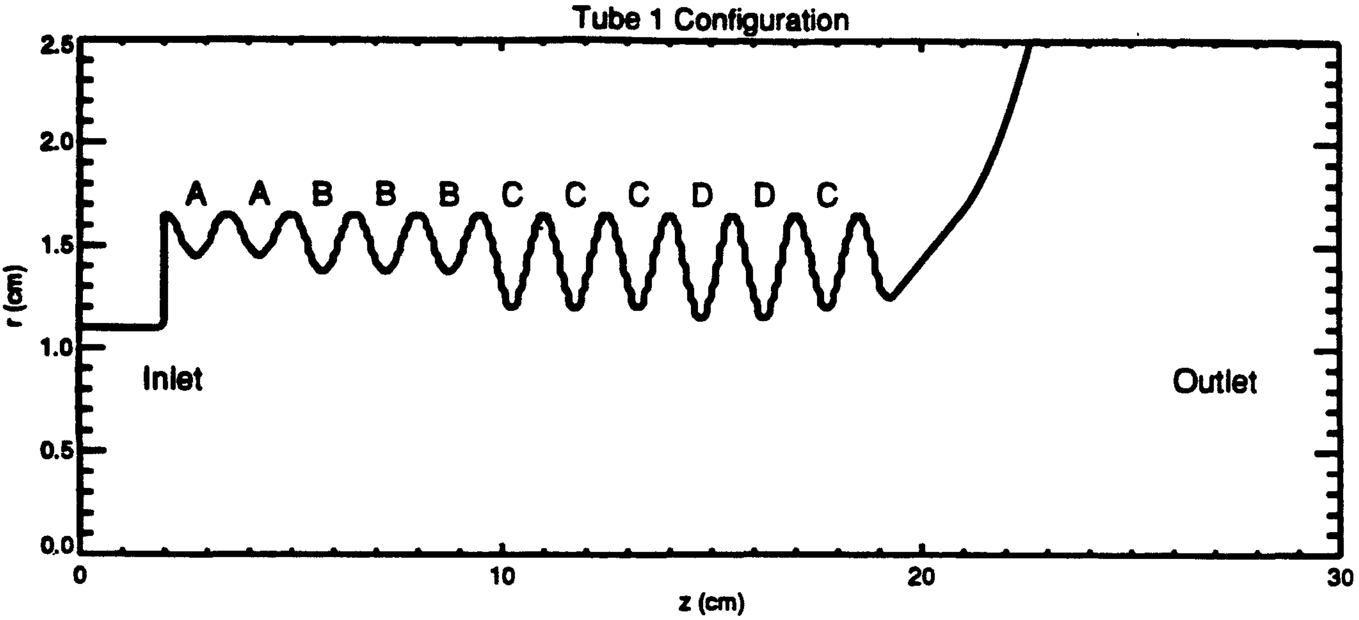
Tube 1 Configuration
A
A
B
B
B
C
C
C
D
D
C
Inlet
Outlet
r (cm)
2.5
2.0
1.5
1.0
0.5
0.0
0
10
20
30
z (cm)

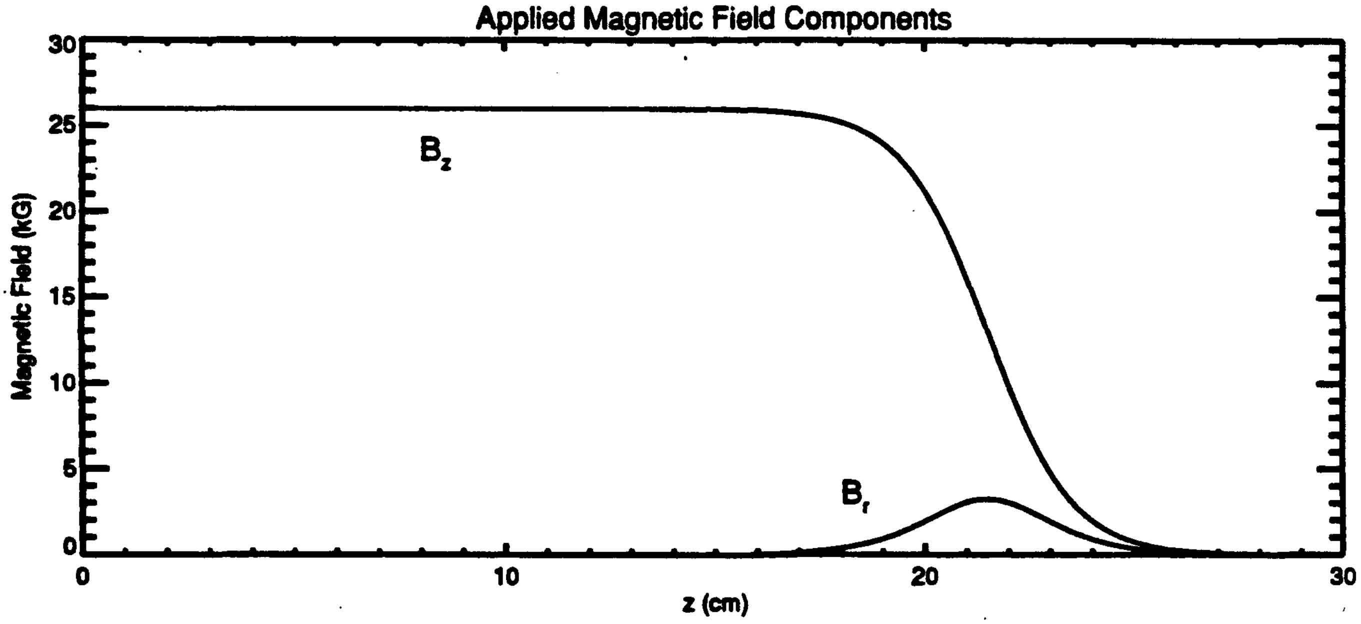
Applied Magnetic Field Components
B_z
B_r
Magnetic Field (kG)
30
25
20
15
10
5
0
0
10
20
30
z (cm)

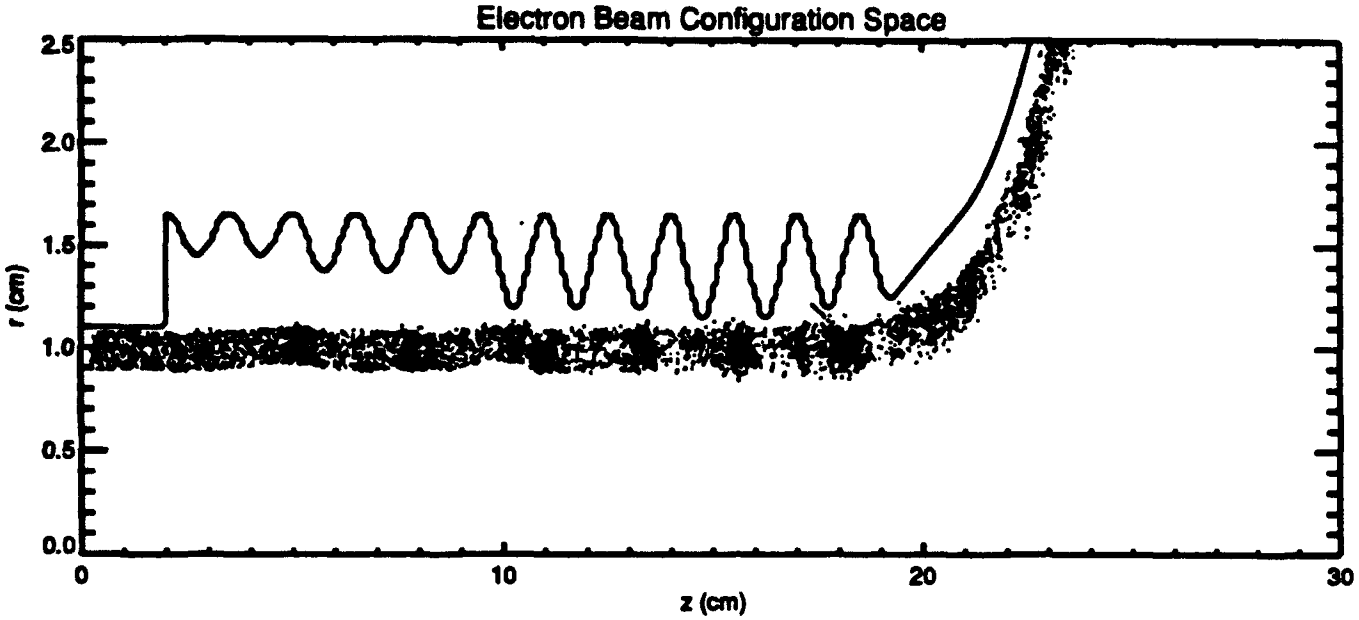
Electron Beam Configuration Space

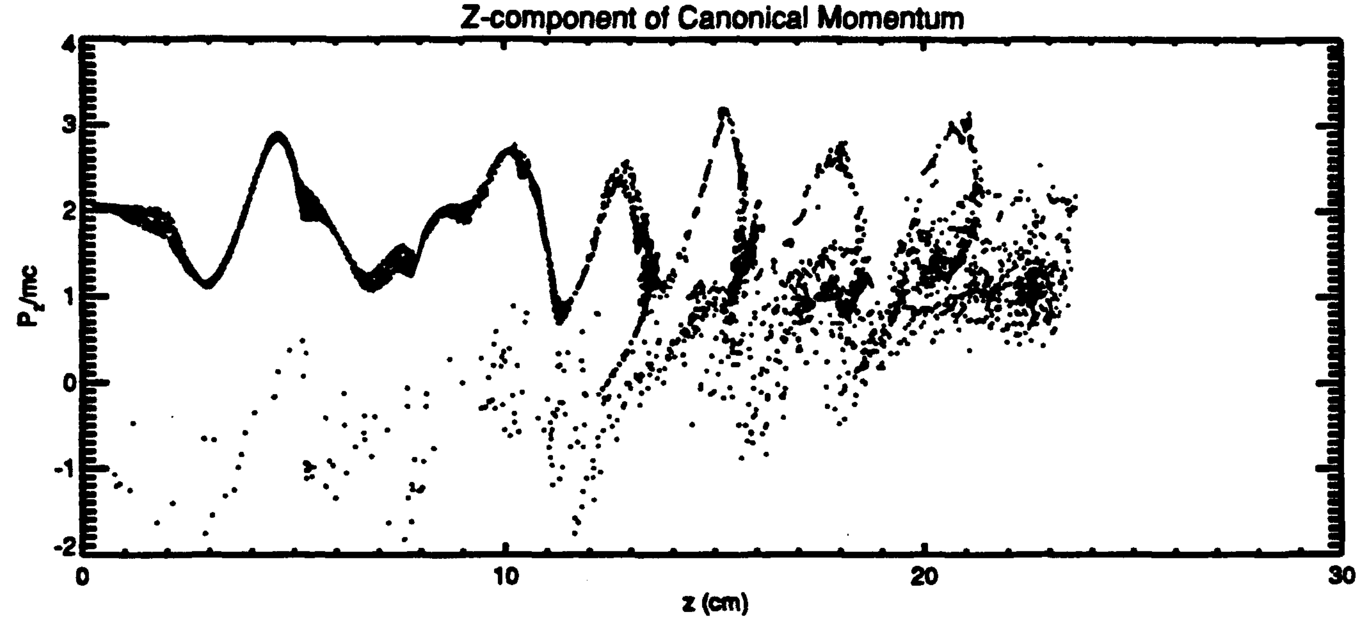
Z-component of Canonical Momentum

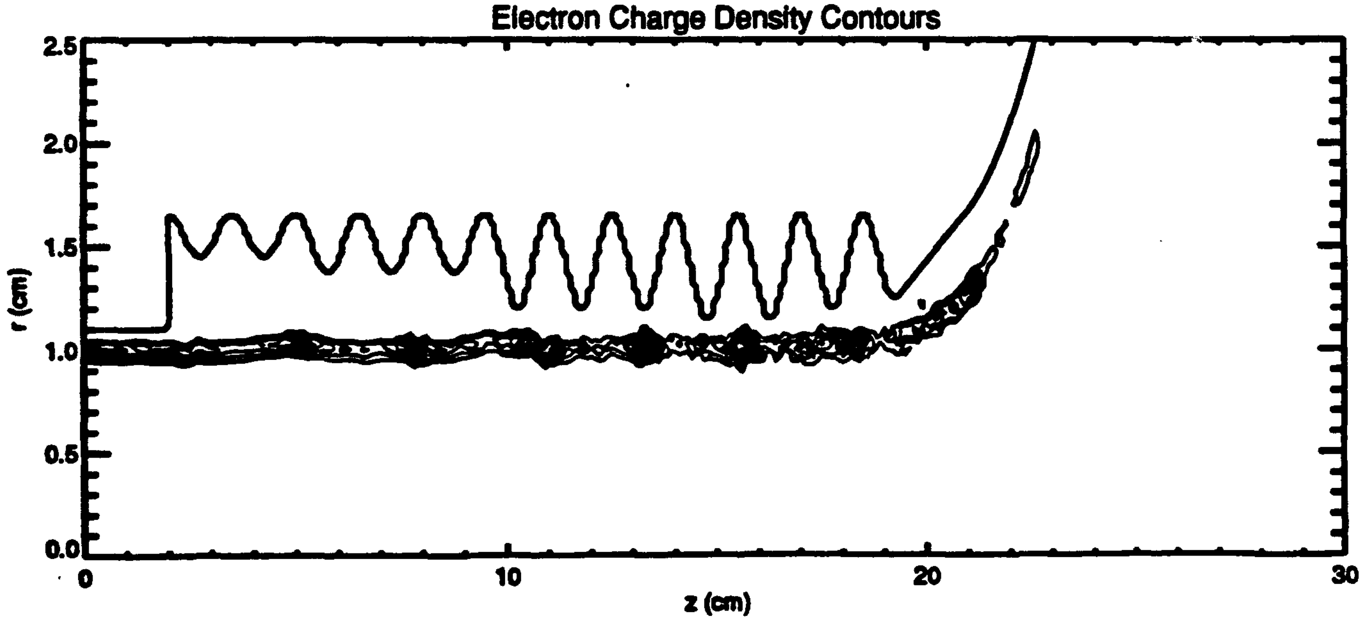
Electron Charge Density Contours

T o P

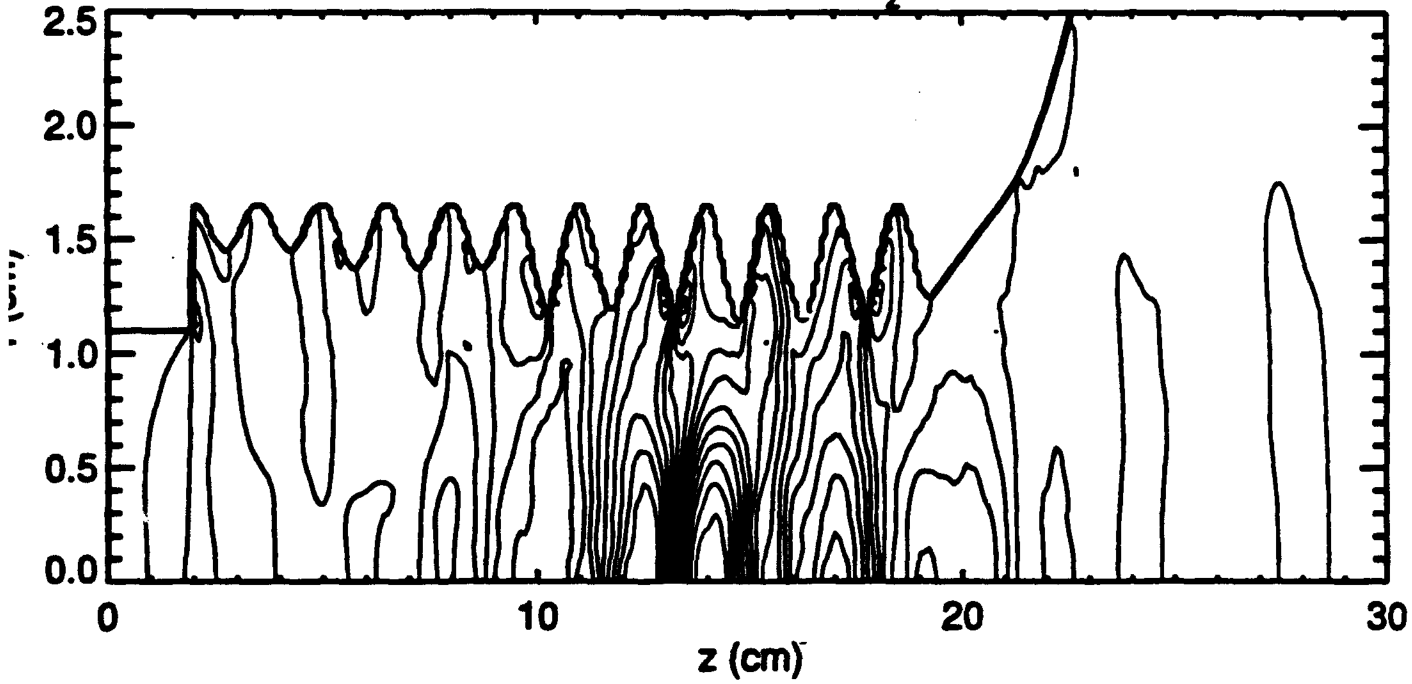
Contours of E_z

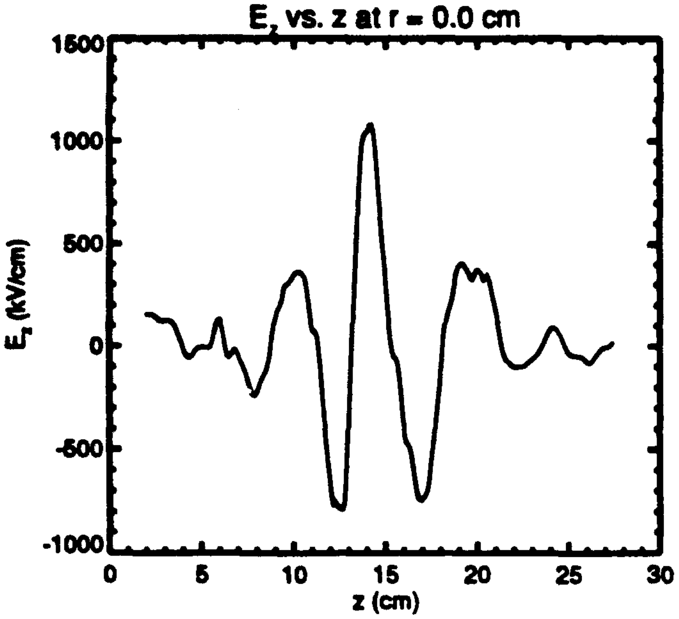
E_z vs. z at r = 0.0 cm

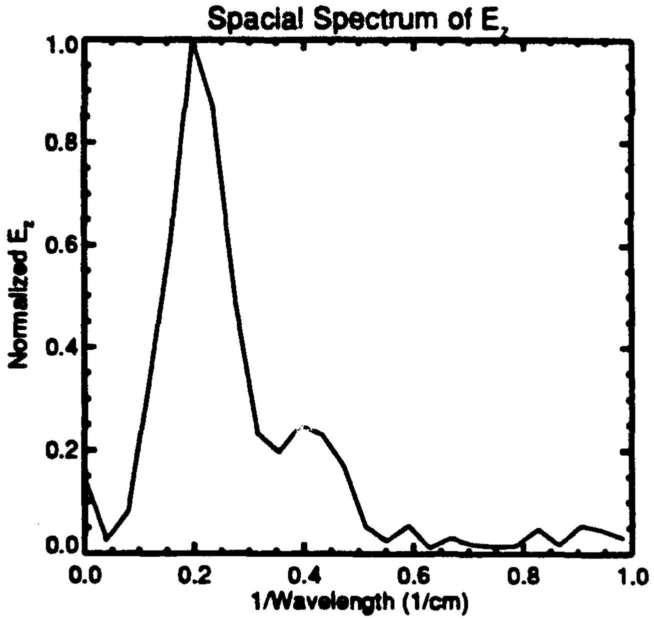
Spacial Spectrum of E_z

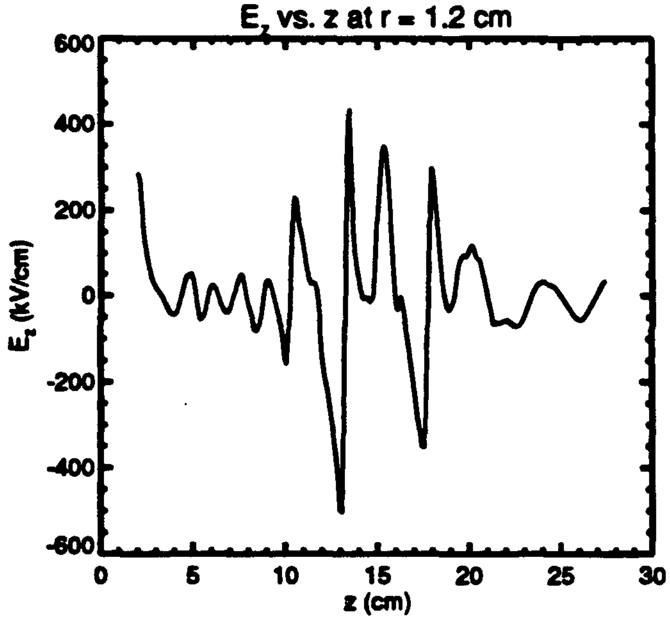
E_z vs. z at r = 1.2 cm

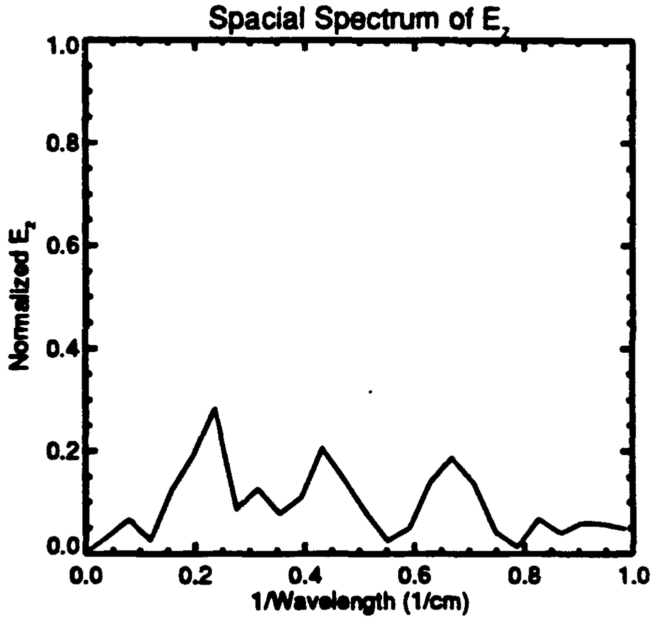
Spacial Spectrum of E_z

TOP

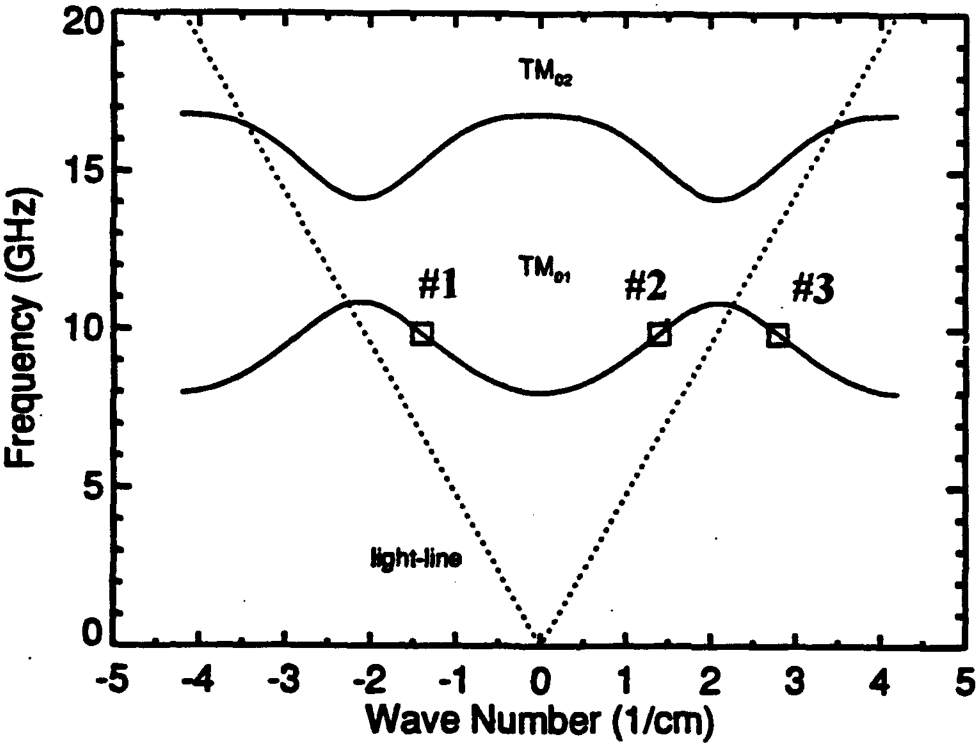
TM$_{02}$
TM$_{01}$
#1
#2
#3
light-line
Frequency (GHz)
20
15
10
5
0
-5
-4
-3
-2
-1
0
1
2
3
4
5
Wave Number (1/cm)

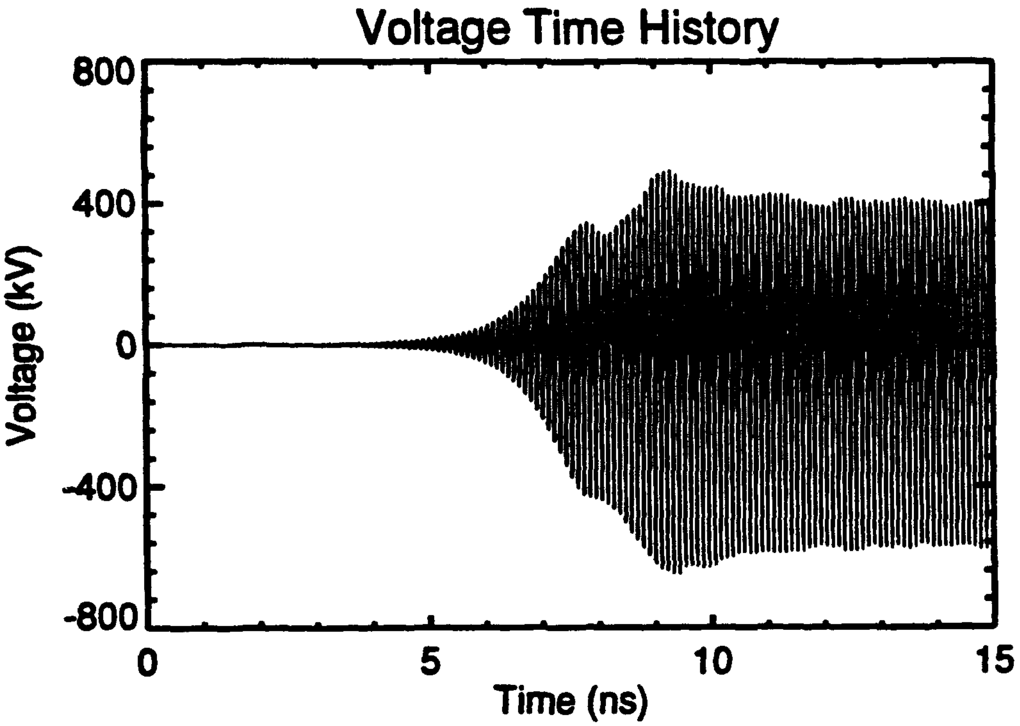
Voltage Time History

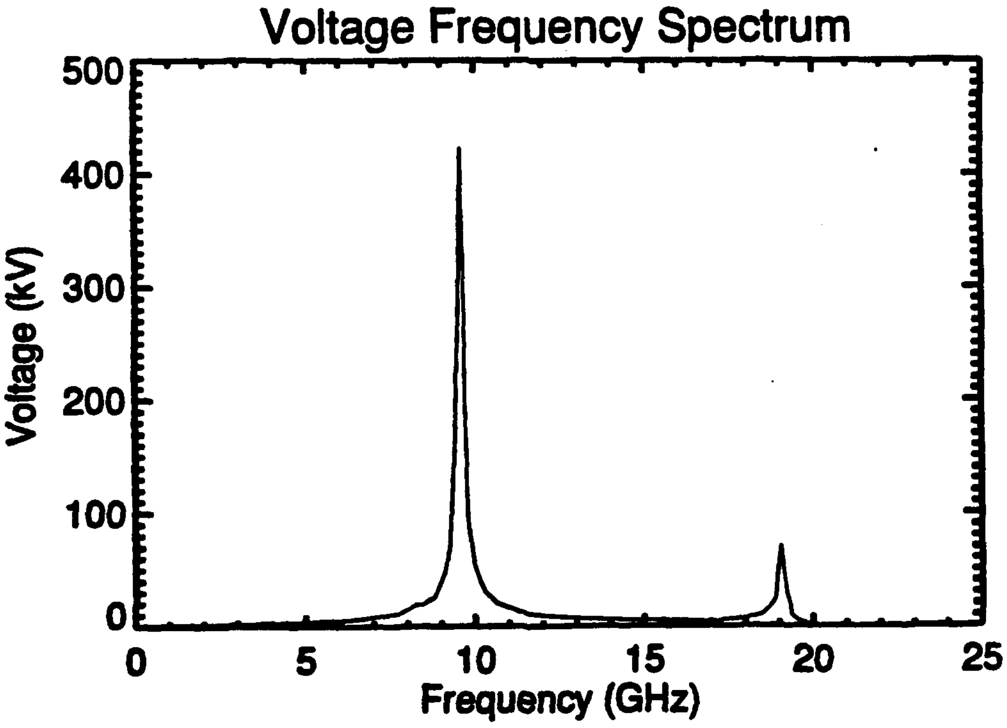
Voltage Frequency Spectrum

TOP

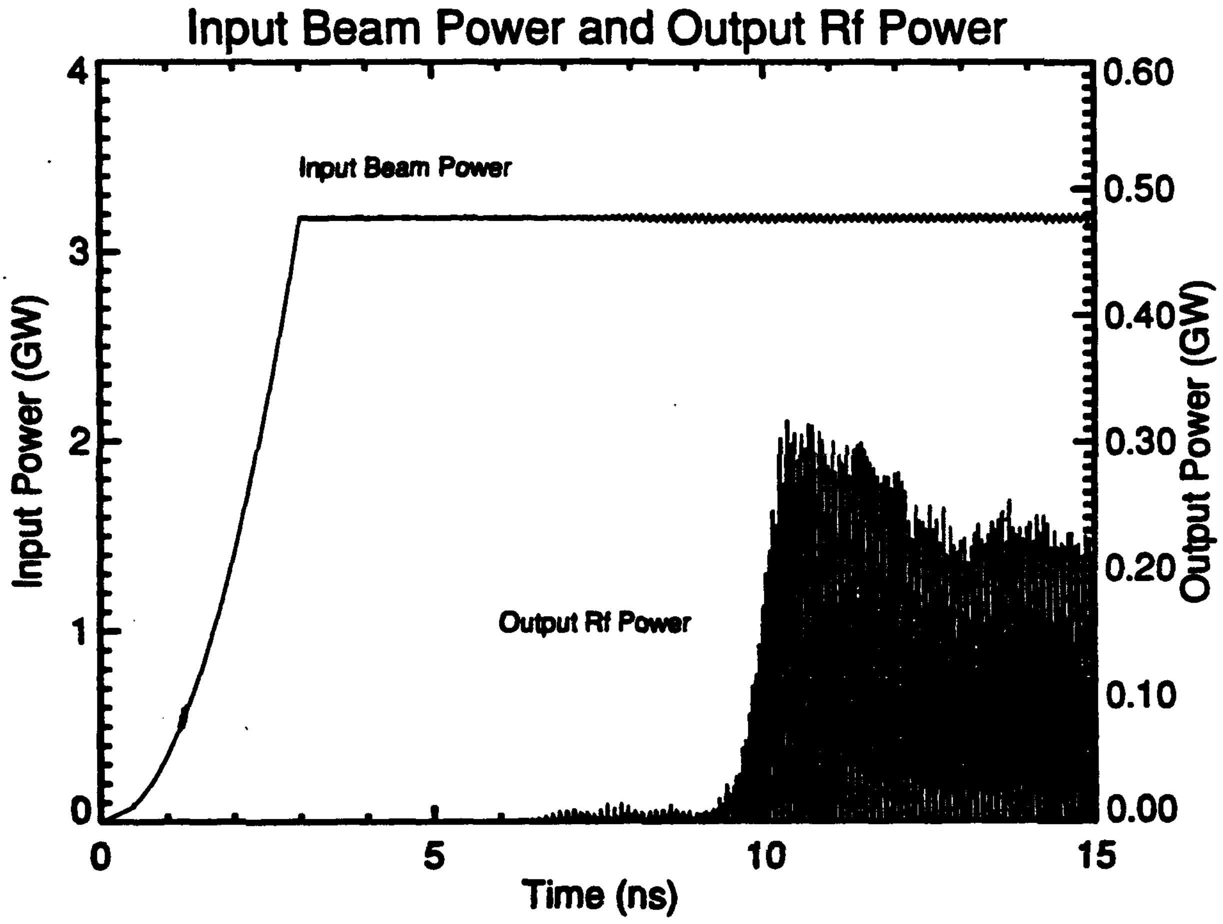
Input Beam Power and Output Rf Power
Input Beam Power
Output Rf Power
Input Power (GW)
Output Power (GW)
Time (ns)
0
1
2
3
4
0.00
0.10
0.20
0.30
0.40
0.50
0.60
0
5
10
15

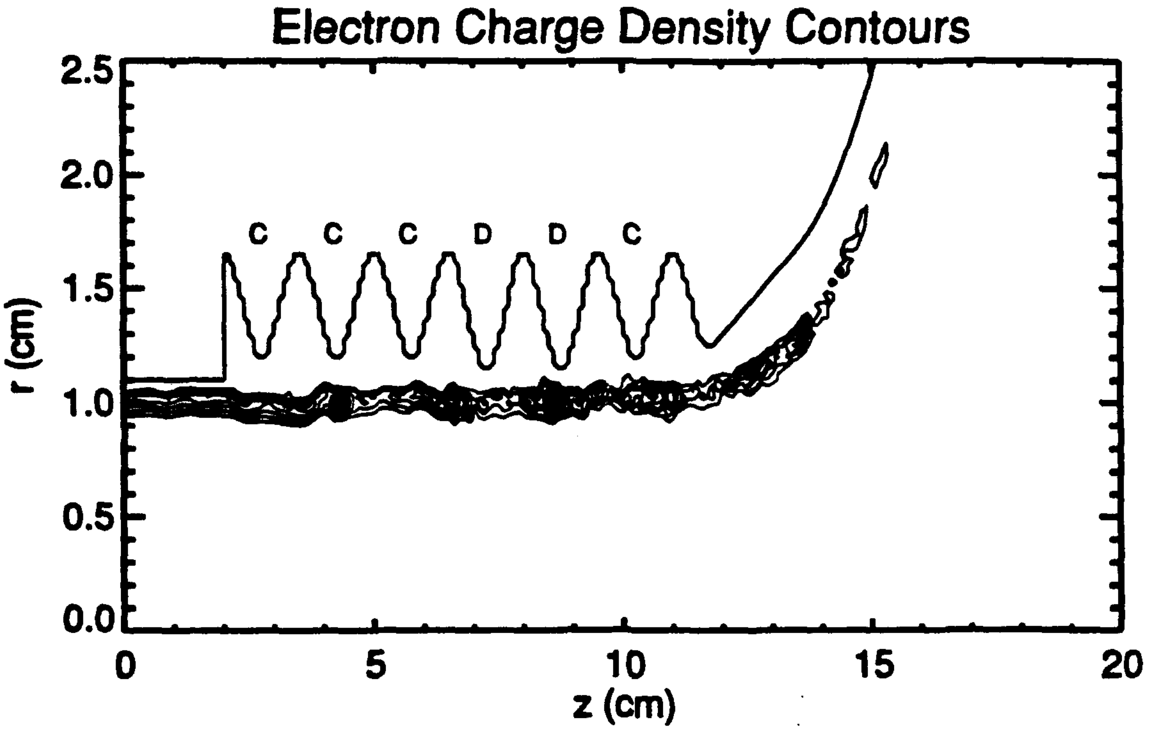
Electron Charge Density Contours

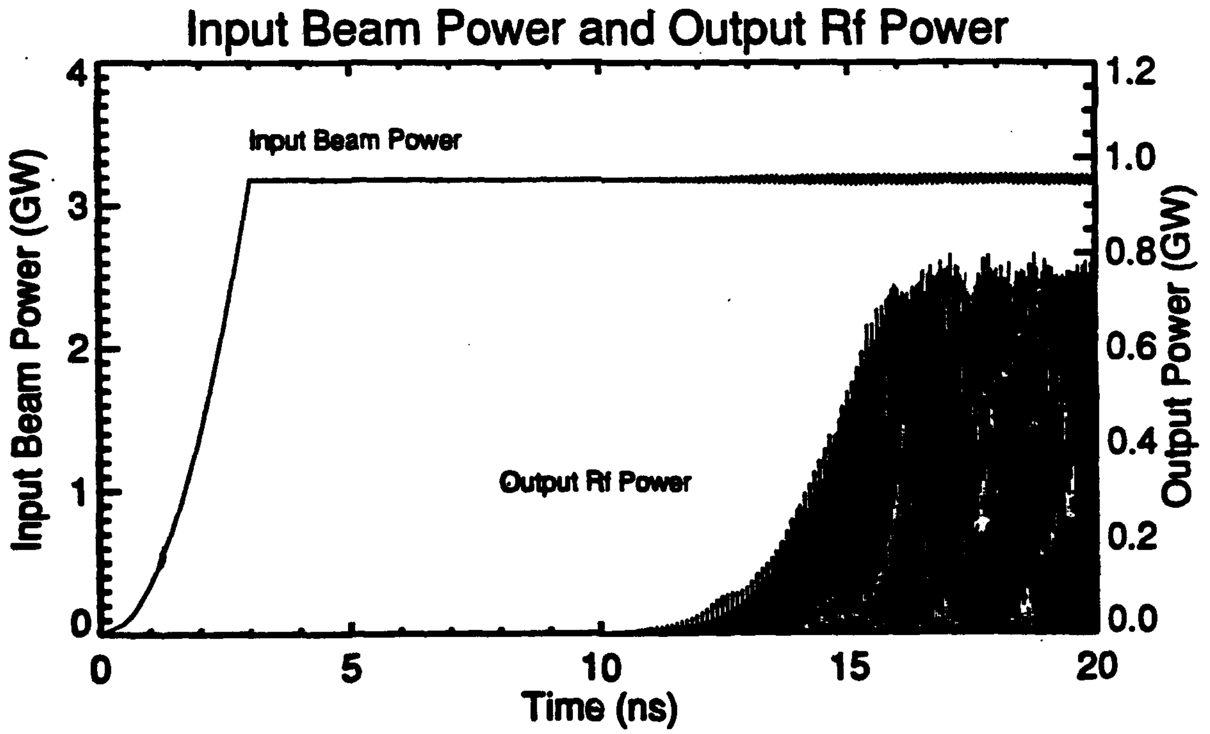
Input Beam Power and Output Rf Power

Top

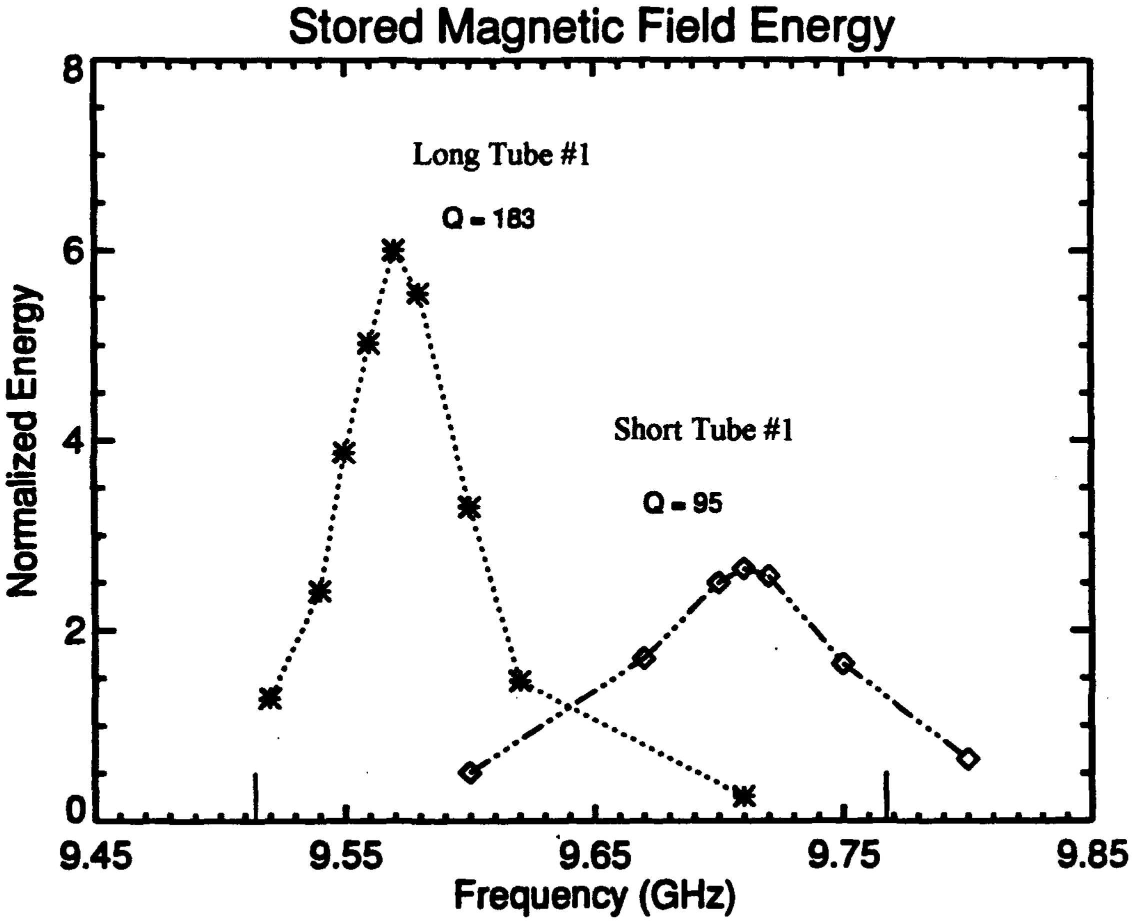
Stored Magnetic Field Energy
Normalized Energy
Frequency (GHz)
Long Tube #1
Q = 183
Short Tube #1
Q = 95
0
2
4
6
8
9.45
9.55
9.65
9.75
9.85